EFFECT OF LASER PROCESSING ON SURFACE CHARACTERISTICS OF MAGNESIUM BASED RARE EARTH ELEMENT ALLOYS

Thesis

Submitted in partial fulfillment of the requirements for the degree of

DOCTOR OF PHILOSOPHY

by

RAKESH K. RAJAN

DEPARTMENT OF MECHANICAL ENGINEERING

NATIONAL INSTITUTE OF TECHNOLOGY KARNATAKA,

SURATHKAL, MANGALORE – 575025

DECEMBER, 2018

D E C L A R A T I O N

I hereby *declare* that the Research Thesis entitled **" EFFECT OF LASER PROCESSING ON SURFACE CHARACTERISTICS OF MAGNESIUM BASED RARE EARTH ELEMENT ALLOYS"** which is being submitted to the **National Institute of Technology Karnataka, Surathkal** in partial fulfillment of the requirements for the award of the Degree of **Doctor of Philosophy** in **Department of Mechanical Engineering** is a *bonafide report of the research work carried out by me*. The material contained in this Research Thesis has not been submitted to any University or Institution for the award of any degree.

Register Number : **145040ME14F13**

Name of the Research Scholar : **RAKESH K. RAJAN**

Signature of the Research Scholar :

Department of Mechanical Engineering,

Place: NITK, Surathkal

Date:

C E R T I F I C A T E

This is to *certify* that the Research Thesis entitled **"EFFECT OF LASER PROCESSING ON SURFACE CHARACTERISTICS OF MAGNESIUM BASED RARE EARTH ELEMENT ALLOYS"** submitted by **Mr. RAKESH K. RAJAN** (**Register Number: 145040ME14F13**) as the record of the research work carried out by him, is *accepted as the Research Thesis submission* in partial fulfillment of the requirements for the award of degree of **Doctor of Philosophy.**

Research Guides

Dr. Srikanth Bontha
Associate Professor

Dr. Ramesh M.R
Associate Professor

Department of Mechanical Engineering
NITK, Surathkal

Chairman - DRPC
Date:

ACKNOWLEDGMENTS

It is my great pleasure and privilege to express my gratitude to **Dr. Srikanth Bontha,** Associate Professor, Department of Mechanical Engineering, National Institute of Technology, Karnataka, Surathkal for his exemplary guidance, inspiration and constructive criticism during the course of this work.

I would like to thank my co-guide, **Dr. Ramesh M.R,** Associate Professor ,Department of Mechanical Engineering, National Institute of Technology, Karnataka. for always expressing his willingness to support and allowed me tremendous freedom to explore the project with valuable research ideas.

I wish to express my sincere thanks to **Prof. Shrikantha S. Rao,** Head, Department of Mechanical Engineering, and all former HOD's, faculty members, technical and administrative staff of the Mechanical Engineering Department, National Institute of Technology, Karnataka, for their kind help in providing the facilities as and when needed.

I sincerely thank my RPAC members, **Dr. Mrityunjay Doddamani**, Assistant Professor, Department of Mechanical Engineering, National Institute of Technology, Karnataka and **Dr. Shashi Bhushan Arya,** Assistant Professor, Department of Metallurgical and Materials Engineering, National Institute of Technology, Karnataka for providing valuable suggestions and also for the support extended to me on all occasions.

I am grateful to **Dr.Vamsi Krishna Balla** and **Dr. Mitun Das**, CSIR-Central Glass Ceramic Institute (CGCRI), Kolkatta, India both for their immense support in extending laser surface melting facility throughout the period of study and also for their valuable inputs on my research work. **Dr.Srinivasan A**, CSIR- National Institute for Interdisciplinary Science and Technology (NIIST), Trivandrum, India, and **Dr. T.Ram Prabhu,** Defence Research and Development Organization, Bangalore, India, are also greatfully acknowledged for providing the facility for casting of magnesium alloys.

I would like to thank my friends, Dr.Nivish George,Sneha Raj, Dr.Sudheer R , who had provided everlasting optimism, brilliant ideas and assistance throughout all my challenging situations. I also extend my gratitude towards Sinu Chandran and Dr. Shaju K Albert, IGCAR, Kalpakkam India for their support in interpreting corrosion results.

All the Advanced Manufacturing and Tribology lab members, especially Mr. Mallikarjuna B, Mr. Vinay Varghese, Mr. Praveen Jeyachandran, Mr. Pratyush Mohanty, Mr. Danish Ashraf, Mr. Aneesh Patil, Mr. Uzawal Kiran, Dr. Gajanan Annae, Dr. Nithin H.S, Mr.Bhaskar for their constant help and encouragement during the process of research work. I also wish to thank my friends Dr. Jaivardhan M.L, Mr. Praddep Badiger and Mr. Ashrith H.S from Department of Mechanical Engineering, Dr.Baskaran T, Mr. Prabhu Kumar, Mr. Rajesh K.R, Mr. Vivek Naryanan from Department of Metallurgical and Materiald Engineering and Mr.Vishnu M from Department of Chemical Engineering for their everlasting supports at various stages of my research work.

I am thankful to the Director and administration of National Institute of Technology, Karnataka, for providing all necessary facilities and funds to carry out my work.

Finally I would like to thank my family for their undying love, encouragement and support throughout my life and education. Especially I would like to dedicate this quantum of work to my father who left this world during the final stages of my research work.

(**RAKESH K. RAJAN**)

ABSTRACT

Magnesium (Mg) based alloys have attracted considerable interest in the biomedical field as materials for temporary implants, primarily due to their dissolution in physiological environments and absorption by the human body. However, several problems such as inadequate strength and rapid degradation must be addressed before Mg alloys can be used as bone implants. These inadequacies of Mg alloys can be addressed either by alloying or through surface modification.

The first part of this work aims to develop Mg based alloys containing zinc (Zn) and rare earth elements such as gadolinium (Gd), dysprosium (Dy) and neodymium (Nd) for temporary implant applications. Three different alloys with compositions such as Mg-1%Zn-2% Gd, Mg-1%Zn-2%Dy and Mg-3%Zn-1.5%Gd-1.5%Nd (all in wt.%) are developed via casting route and investigated for microstructure, mechanical properties, *in vitro* corrosion behavior and cytotoxicity. The microstructure results indicate that apart from major α-Mg phase and few binary phases, Mg-Zn-Gd and Mg-Zn-Dy alloys consist of lamellar long period stacking ordered (LPSO) phases. The *in vitro* degradation behavior were studied by immersion and electrochemical methods in hanks balanced salt solution (HBSS). The corrosion rate obtained from both the methods are in the order of Mg-Zn-Gd < Mg-Zn-Gd-Nd < Mg-Zn-Dy. The MTT (methylthiazoldiphenyl-tetrazolium bromide) assay study revealed that all the three alloys had no adverse effect on cells and proves the good cytocompatibility of these alloys. The ultimate tensile strength of Mg-Zn-Gd-Nd is better than the Mg-Zn-Gd and Mg-Zn-Dy alloys due to the uniform distribution of the precipitate phase.

In order to tailor the surface properties of these alloys, the second part of this work proposes to understand the effect of laser surface melting (LSM) of Mg-Zn-Gd, Mg-Zn-Dy and Mg-Zn-Gd-Nd alloys on microstructural changes, hardness variation, wettability and *in vitro* degradation behaviour. Different ranges of laser energy densities have been adopted to alter the surface characteristics of all the alloys and proper correlations have been drawn with respect to the un-altered surface. The surface modified samples showed fine grain structure in the melt zone compared to the untreated substrate. The surface remelting of material at lower energy density conditions promoted the formation of micro cracks in the meltpool zone. Cross

sectional microhardness was observed after laser surface melting. Hardness increase of nearly two times was observed in laser melted region due to the grain refinement and solid solution strengthening. *In vitro* degradation study showed clear improvement in corrosion resistance of LSM samples at certain range of energy densities. At higher energy density, removal of materials from the surface is enhanced, resulting in deeper grooves and higher surface roughness. The wettability studies indicated that the variations in surface chemical composition, grain size and surface roughness of LSM samples strongly influence the surface energy and hydrophilicity.

Keywords : *Mg-Zn-REE, Laser surface melting, Mechanical behavior, Degrdation behavior, Surface roughness, Cytotoxicity, Wettability.*

CONTENTS

DECLARATION

CERTIFICATE

ACKNOWLEDGEMENTS

ABSTRACT

CONTENTS i

LIST OF FIGURES v

LIST OF TABLES xi

ABBREVIATIONS xiii

NOMENCLATURE xv

CHAPTER 1 1

1 INTRODUCTION 1

1.1 Magnesium alloys in structural engineering field 3

1.2 Magnesium alloys in biomedical field 4

1.3 Magnesium based rare earth element (REE) alloys 5

1.4 Laser surface melting (LSM) 6

CHAPTER 2 11

2 LITERATURE SURVEY 11

2.1 History of magnesium and magnesium alloys as biomaterials 11

2.2 Recent developments of Mg alloys for biomedical applications 11

2.3 Mg-Zn based alloy systems 14

2.4 Magnesium based Rare Earth Element (REE) alloys 15

2.5 Mg-Zn-Gd based alloy system 16

2.6 Mg-Zn-Dy based alloy system 17

2.7 Mg-Zn-Gd-Nd based alloy system 19
2.8 Laser surface modification of magnesium alloys 21
2.9 Summary of literature survey 24
2.10 Objectives of the study 25
2.11 Outline of the thesis 26
CHAPTER 3 28
3 MATERIALS AND METHODS 28
3.1 Methodology 28
3.2 Casting of alloys 29
3.3 Laser Surface Melting (LSM) of alloys 30
3.4 Microstructural characterization 33
3.4.1 Optical Microscope (OM) 33
3.4.2 Scanning Electron Microscope (SEM) 33
3.4.3 Transmission Electron Microscope (TEM) 33
3.5 Phase analysis 34
3.6 Integrated Coupled Plasma-Atomic Emission Spectroscopy (ICP-AES) 34
3.7 Mechanical properties 34
3.7.1 Tensile testing 34
3.7.2 Microhardness 35
3.8 Surface roughness measurement 36
3.9 Wettability behavior 36
3.10 In-vitro degradation 37
3.11 Atomic Absorption Spectroscopy (AAS) 40
3.12 Fourier Transform Infrared Spectroscopy (FTIR) 40
3.13 In-vitro cell material interactions 41

CHAPTER 4 42

4 RESULTS AND DISCUSSION 42

4.1 Studies on as cast alloys 42

4.1.1 Compositional analysis 42
4.1.2 Microstructural analysis 42
4.1.3 Phase analysis 50
4.1.4 *In-vitro* degradation-Immersion studies 50
4.1.5 Electrochemical behaviour 57
4.1.6 *In vitro* cell-materials interactions 60
4.1.7 Mechanical properties 62
4.1.8 Conclusions 64

4.2 Studies on laser surface melted (LSM) Mg-Zn-Gd alloy system 66

4.2.1 Microstructural analysis 66
4.2.2 Phase analysis 70
4.2.3 Microhardness distribution 71
4.2.4 Surface roughness analysis of LSM samples 72
4.2.5 Wettability behaviour 73
4.2.6 *In-vitro* degradation-Immersion method 76
4.2.7 Corrosion damage characterization 80
4.2.8 Conclusions 86

4.3 Studies on laser surface melted Mg-Zn-Dy alloy 87

4.3.1 Microstructural analysis 87
4.3.2 Phase analysis 91
4.3.3 Microhardness distribution 92
4.3.4 Surface roughness analysis of LSM samples 93
4.3.5 Wettability behaviour 95
4.3.6 *In-vitro* degradation-Immersion method 97
4.3.7 Corrosion damage characterisation 103
4.3.8 Conclusions 109

4.4 Studies on laser surface melted Mg-Zn-Gd-Nd alloy 110

4.4.1 Microstructural analysis 110
4.4.2 Phase analysis 113
4.4.3 Microhardness distribution 115
4.4.4 Surface roughness analysis of LSM samples 116
4.4.5 Wettability behaviour of LSM samples 117
4.4.6 *In-vitro* degradation-Immersion method 120
4.4.7 Corrosion damage characterization 124
4.4.8 Conclusions 130
CHAPTER 5 132
5 Conclusions and Future work 132
5.1 Overall conclusions 132
5.1.1 As-cast alloys 132
5.1.2 Laser surface melted alloys 132
5.2 Future work 133
REFERENCES 134
LIST OF PUBLICATIONS 152
BIO-DATA 154

LIST OF FIGURES

Figure 2.1 Real/possible applications of biodegradable magnesium implants (a) cardiovascular stents (BIOTRONIK, Germany) (b) MAGNEZIX screw (c) Micro clip for laryngeal microsurgery (pure Mg) (d) orthopedic plates and screws (e) wound closing device (Chen et al. 2014) 13
Figure 2.2 Mg-Gd Phase diagram (Hort et al. 2010) 17
Figure 2.3 Mg-Dy Phase diagram (Bi et al. 2014) 18
Figure 2.4 Mg-Nd phase diagram (Okamoto 2013) 20
Figure 3.1 Magnesium casting facility (Courtesy: CSIR-NIIST) 29
Figure 3.2 Schematic representation of laser surface melting 31
Figure 3.3 Experimental setup of LENS^{TM} system 31
Figure 3.4 Tensile testing (a) Electronic tensometer (b) Tensile specimens (c) Schematic of specimen 35
Figure 3.5 Microhardness tester 36
Figure 3.6 Contact angle analyzer (Goniometer) 37
Figure 3.7 Immersion study (a) schematic diagram (b) experimental set up (c) enlarged view of beaker and (d) mounted samples. 38
Figure 4.1 Optical micrograph of (a) Mg-Zn-Gd (b) Mg-Zn-Dy (c) Mg-Zn-Gd-Nd 43
Figure 4.2 SEM microstructure of alloys showing morphology of different phases (a) Mg-Zn-Gd (b) Mg-Zn-Dy (c) Mg-Zn-Gd-Nd 44
Figure 4.3 TEM of Mg-Zn-Gd alloy with SAED patterns of $(Mg, Zn)_3Gd$ phase 47
Figure 4.4 TEM of Mg-Zn-Gd alloy with LPSO phase 47
Figure 4.5 TEM analysis of Mg-Zn-Dy eutectic phase with SAED pattern 48
Figure 4.6 TEM analysis of Mg-Zn-Dy LPSO phase 48
Figure 4.7 TEM analysis of Mg-Zn-Gd-Nd with granular phases 49
Figure 4.8 TEM analysis of Mg-Zn-Gd-Nd with rod phase 49
Figure 4.9 X-ray diffraction analysis of different phases in (a) Mg-Zn-Gd, (b) Mg-Zn-Dy and, (c) Mg-Zn-Gd-Nd alloys 50

Figure 4.10 The rate of hydrogen evolution through immersion corrosion of the three developed alloys as a function of immersion time in HBSS 51
Figure 4.11 Amount of Mg^{2+} released through immersion corrosion of the three developed alloys as a function of immersion time in HBSS 52
Figure 4.12 XRD analysis of alloy samples after 180 h of immersion 56
Figure 4.13 SEM surface morphology of (a) Mg-Zn-Gd (b) Mg-Zn-Dy (c) Mg-Zn-Gd-Nd alloys samples after 180 h of immersion 57
Figure 4.14 Tafel plot extrapolation of the Mg-Zn-REE alloys tested in HBSS 58
Figure 4.15 The influence of different REE addition on the *in vitro* cell viability,..... 61
Figure 4.16 SEM micrographs with the morphology of NIH 3T3 cells in (a) Mg-Zn-Gd, (b) Mg-Zn-Dy and (c) Mg-Zn-Gd-Nd alloys after 1 day of cell culturing. 61
Figure 4.17 SEM micrograph revealing the tensile fracture surface morphology of the (a) Mg-Zn-Gd (b) Mg-Zn-Gd-Nd (c) Mg-Zn-Dy..... 64
Figure 4.18 Typical cross sectional SEM microstructures of (a) Laser surface melted Mg-Zn-Gd alloy (b) enlarged LSM zone (at 25 J/mm^2) (c) enlarged view of top region of the melt pool (d) Bottom region of the melt pool with heat affected zone (HAZ). 68
Figure 4.19 Cross sectional (SEM) micrograph of LSM sample with meltpool at energy densities of (a) 12.5 J/mm^2 (b) 17.5 J/mm^2 (c) 22.5 J/mm^2 (d) 25 J/mm^2 (e) 35 J/mm^2 (f) 45 J/mm^2 70
Figure 4.20 Comparison of XRD results of as cast and selected LSM Mg-Zn-Gd alloy 71
Figure 4.21 Hardness distribution in as cast and LSM Mg-Zn-Gd samples..... 72
Figure 4.22 Surface topographies of laser treated Mg-Zn-Gd alloy (a) SEM image, Roughness (3D maps) profiles at (b) 25 J/mm^2 (c) 35 J/mm^2 (d) 45 J/mm^2 73
Figure 4.23 Schematic of contact angle analysis on as-cast and LSM sample surface by using polar liquid (DI Water) (R_z represents the line roughness)..... 75
Figure 4.24 Rate of hydrogen evolution from as-cast and LSM Mg-Zn-Gd samples during immersion in HBSS (All the LSM units are in J/mm^2) 77
Figure 4.25 Cumulative Mg^{2+} ion release from as-cast and LSM Mg-Zn-Gd samples during immersion in HBSS (All the LSM units are in J/mm^2)..... 78

Figure 4.26 Corrosion rate comparison of as cast and LSM Mg-Zn-Gd alloy samples by weight loss method after 180 hours of immersion in HBSS..... 80
Figure 4.27 Cross sectional view of the corroded surface after immersion in HBSS for 180 h (a) As- cast Mg-Zn-Gd alloy and laser treated at (b) 12.5 J/mm^2 (c) 45 J/mm^2..... 81
Figure 4.28 Cross sectional view meltpool overlapping variations at (a) 12.5 J/mm^2 (b) 45 J/mm^2 82
Figure 4.29 Surface morphology of degraded Mg-Zn-Gd alloy (a) 12.5 J/mm^2 (a.1) Enlarged view of the surface product (b) 35 J/mm^2 (c) 45 J/mm^2 laser melted sample immersed in HBSS for 180 hrs. 84
Figure 4.30 XRD spectra of corrosion product extracted from 12.5 J/mm^2 and 25 J/mm^2 laser melted sample immersed in HBSS for 180 hours 85
Figure 4.31 FTIR spectra of corrosion product of LSM Mg-Zn-Gd after immersion in HBSS..... 85
Figure 4.32 (a) Typical cross sectional microstructure of Mg-Zn-Dy alloy laser surface melted at 25 J/mm^2 (b) and (c) Enlarged view of microstructural changes in different regions, (d) and (e) Meltpool depth of the alloy processed at 25 J/mm^2 and 45 J/mm^2, respectively. 90
Figure 4.33 X-Ray diffraction analysis of different phases in as cast and laser melted Mg-Zn-Dy alloy..... 92
Figure 4.34 Microhardness distribution of as cast and LSM Mg-Zn-Dy alloy samples.. 93
Figure 4.35 3D surface maps of LSM samples processed at (a) 12.5 J/mm^2 (b) 22.5 J/mm^2 (c) 35 J/mm^2 (d) 45 J/mm^2 94
Figure 4.36 Hydrogen evolution extracted during the immersion study in HBSS 99
Figure 4.37 Mg^{2+} release extracted during the immersion study in HBSS..... 99
Figure 4.38 pH changes extracted during the immersion study in HBSS..... 100
Figure 4.39 Measured degradation rate and it comparison after 180 hours of immersion in HBSS..... 102

Figure 4.40 SEM image of cross sections of samples after 180 hours of immersion (a) as-cast sample (b) 12.5 J/mm^2 and (c) 45 J/mm^2 laser processed sample (d) Enlarged view of solidification crack (e) Pit at the overlapping zone 105
Figure 4.41 SEM images of surface after 180 hours of immersion (a) as cast alloy (b) 12.5 J/mm^2 (c) 17.5 J/mm^2 and (d) 35 J/mm^2 laser processed samples 107
Figure 4.42 SEM+EDS mapping analysis of corrosion product after 180 hours of immersion in HBSS 107
Figure 4.43 XRD analysis of corrosion product after 180 hours of immersion..... 108
Figure 4.44 FTIR Spectra analysis of corrosion product extracted from corroded sample after 180 hours of immersion..... 108
Figure 4.45 Cross sectional SEM morphology (a) LSM modified zone and substrate (b) fine cells in the meltpool (marked 1) (c) columnar grain in the meltpool (marked 2) and (d) overlapping zone and HAZ (marked 3,4 in the meltpool) 111
Figure 4.46 Laser processing parameters and meltpool depth variations 112
Figure 4.47 Phase analysis of as cast and LSM Mg-Zn-Gd-Nd alloy 114
Figure 4.48 Micro hardness distribution and the cross sectional indentation spots in the samples..... 115
Figure 4.49 Contact angle variation in LSM samples with respect to the energy density and as cast conditions..... 118
Figure 4.50 Contact angle variation in polished LSM samples with respect to the energy density and as cast conditions..... 119
Figure 4.51 (a) The hydrogen evolution trend (a.1) enlarged view as a function of immersion time in HBSS 122
Figure 4.52 (a) Mg^{2+} ion release rate during the period of 180 hours of immersion in HBSS, enlarged views (a.1) and (a.2) as a function of immersion time..... 122
Figure 4.53 Degradation rate comparison through different methods..... 124
Figure 4.54 Cross sectional SEM images of (a) as cast (b) 12.5 J/mm^2 (c) 35 J/mm^2 (d) 45 J/mm^2 samples after 180 hours of immersion in HBSS. 125

Figure 4.55 Surface morphology of (a) as cast (b) 12.5 J/mm^2 (c) 35 J/mm^2 (d) 45 J/mm^2 samples after 180 hours of immersion in HBSS taken in SEM. 127
Figure 4.56 SEM + EDS mapping of surface product after immersion study 129
Figure 4.57 XRD spectra of corrosion product after immersion in HBSS for a period of 180 hours..... 129
Figure 4.58 FTIR Spectra of corrosion products extracted after 180 hours of immersion in HBSS..... 130

LIST OF TABLES

Table 3.1 Parameters used for laser surface melting..... 32
Table 4.1 Chemical composition of the alloys in wt. % 42
Table 4.2 EDS compositional analysis (wt.%) of different phases observed in the Mg-Zn-REE alloys (Figure 4.2) 45
Table 4.3 Corrosion rate of Mg-Zn-REE alloys derived from immersion corrosion measurements..... 54
Table 4.4 Electrochemical properties derived from Tafel extrapolation 58
Table 4.5 Mechanical properties of as cast alloys..... 63
Table 4.6 Typical composition of laser melted zone and as cast Mg-Zn-Gd alloys analyzed by EDS (wt. %)..... 67
Table 4.7 Laser parameters, melt pool depths, grain size and roughness of LSM Mg-Zn-Gd alloy..... 69
Table 4.8 Effect of LSM at different laser energy densities on the surface energy and contact angle of as cast, LSM and polished LSM sample 75
Table 4.9 Laser processing conditions and measured melt pool depth..... 89
Table 4.10 EDS analysis of melt pool region and substrate (as cast) of Mg-Zn-Dy alloy 90
Table 4.11 Surface roughness, surface energy and contact angles of laser melted and polished laser melted samples processed at different energy densities 95
Table 4.12 EDS analysis of meltpool region..... 113
Table 4.13 FWHM and grain size of the as-cast and LSM samples 114
Table 4.14 Surface energy and surface roughness results of LSM and LSM polished samples..... 117

ABBREVIATIONS

ASTM	: American Society for Testing and Materials
OM	: Optical Microscope
SEM	: Scanning Electron Microscope
TEM	: Transmission Electron Microscope
EDS	: Energy Dispersive Spectrum
REE	: Rare Earth Elements
UTS	: Ultimate Tensile Strength
YS	:Yield strength
LSM	: Laser Surface Melting
GIXRD	: Glancing Incident X-ray Diffraction
FTIR	:Fourier Transform Infrared Spectroscopy
HBSS	:Hanks Balanced Salt Solution

NOMENCLATURE

ρ	: Density	g/cm^3
E	: Energy density	J/mm^2
v	: Scan velocity	mm/s
d	: Laser beam diameter	µm
P	: Laser power	W
γ_s	: Total surface energy	mN/m
$\boldsymbol{\gamma_s^d}$	: Dispersive component of surface energy	mN/m
γ_S^p	: Polar component of surface energy	mN/m
θ	: Solid/liquid contact angle	Degree
γ_L	: Total surface tension	N/m
Pw	: Average corrosion rate (Hydrogen evolution)	mm·year^{-1}
ΔW	: Weight loss	mg·cm^{-2}·day
V_H	: Hydrogen evolution rate	ml·cm^{-2}·day^{-1}
$(CR)_w$	: Corrosion rate (Weight loss)	mm·year^{-1}
A	: Exposed area	cm^2
$(CR)_i$	: Corrosion rate (Electrochemical study)	mm·year^{-1}/mmpy
EW	: Equivalent weight	g
i_{corr}	: Corrosion current	µA·cm^{-2}

CHAPTER 1

1 INTRODUCTION

Magnesium (Mg), the lightest of all metals is the eighth most abundant element and constitutes about 2% of the earth's crust by weight. It is also the third most plentiful element dissolved in seawater. The history of magnesium dates back to 1755 when Joseph Black discovered that magnesia contained a new element, Magnesium. In 1808, Sir Humphrey Davy was honored as the discoverer, since he successfully isolated the metal by the electrolysis process. Later on, Michael Faraday obtained pure metallic magnesium from reduced dehydrated magnesium chloride. The density of Mg is 1.7 g/cm^3, and its atomic number is 12. It has a hexagonal close-packed (HCP) crystal structure with a = 0.320 nm, c = 0.520 nm and c/a = 1.624. The basal plane is close-packed with an atomic diameter of 0.320 nm.

Mg is classified as an alkaline earth metal. The major advantages of magnesium include:

- Lowest density of all metallic materials
- High specific strength
- Good castability, suitable for high pressure die-casting
- Can be turned, milled at a high speed
- Much improved corrosion resistance using high purity magnesium

The major limitations of Mg and its alloys include:

- Magnesium is a highly flammable metal
- Low elastic modulus
- Limited cold workability and strength
- High degree of shrinkage upon solidification
- High chemical reactivity

The relative density of alloyed Mg is 1.74 g/cm^3 which is two-thirds the density of aluminum (Al), and typical Mg alloys weigh 35% less than their Al counterparts at

equal stiffness (Makar and Kruger, 1993). The high strength-to-weight ratio makes Mg alloys extremely promising for applications requiring lightweight, such as aerospace and transportation. Interestingly, magnesium ions are present in large amounts in the human body and are involved in many metabolic reactions and biological mechanisms. Therefore, magnesium can serve as a metallic biodegradable material in the human body where it can be gradually dissolved, consumed or absorbed. As a potential biodegradable material, magnesium shows many advantages over current metallic materials and biodegradable plastics and ceramics. These advantages include its higher fracture toughness over ceramic biomaterials, higher strength than biodegradable plastics, and more favorable elastic modulus than commonly used biomedical metals. Nevertheless, several problems such as inadequate strength and high corrosion rate prevent the wide spread use of Mg alloys as biomaterials. These problems must be addressed before Mg can be widely used in the bio medical field. To improve its strength and corrosion resistance, alloying is the most widely used strategy and Mg is rarely used in its unalloyed form.

Magnesium alloys have attracted increasing interest in the last decade due to their properties such as excellent specific strength, high damping capacity and better biocompatibility with human body and high recyclability. The research and development of magnesium alloys for industrial and biomedical application have intensively increased during the last few decades. Magnesium must be alloyed with other elements to modify its properties such as ductility, the elastic modulus, corrosion etc. The common alloying elements are Al, Ca, Li, Mn, Rare Earth metals (La, Ce, Nd, Dy, Gd and Y), Si, Zn, and Zr. Based on these alloying elements, alloy are designated by various conventions (Friedrich and Mordike 2006). Commercially available magnesium alloys with their conventions are briefly listed below

- AZ Series The main compositions are Mg-Al-Zn
- AM Series Mg-Al-Mn
- AE Series Mg-Al-Rare Earth Elements (REE)
- EZ Series- Mg-REE-Zn
- ZK Series - Mg-Zn-Zr

- WE Series- Mg-Y-REE

As the desire to further use Mg alloys in various applications grows, different areas of magnesium research must be intensified in order to improve the properties of Mg alloys. Alloys used for structural applications can be recycled back into the products which display the same chemical, physical and mechanical properties as primary material. Recycling requires only 5% of the energy necessary to produce the primary product. This attribute gives a positive impact upon the environment.

1.1 Magnesium alloys in structural engineering field

The high specific strength and good castability make magnesium an attractive and promising structural engineering alloy. Mg alloys are in high demand in the automotive industry as this sector is working to improve the fuel efficiency through weight reduction (Friedrich and Schumann 2001). However, Mg alloys are also associated with a number of limitations compared to other metals such as aluminium alloy. These limitations include low creep resistance, lower tensile properties and poor workability due to its hexagonal structure, low wear and corrosion resistance. Studies have been reported about the various surface treatment approaches such as diffusion coating of magnesium alloys to reduce the wear and corrosion issues (Zhong et al. 2012). Also, Rare Earth Element (REE) addition is considered as an effective approach to increase the creep resistance and strength. Many studies have been carried out with different Mg alloys because pure magnesium in the as cast condition has very low strength and rapid corrosion rate. The alloying elements can directly improve the mechanical properties by solid solution strengthening, precipitation hardening and grain refinement strengthening. The atomic size of the element and the valence are the main factors which influences the solubility. The hexagonal close packed structure (HCP) of magnesium and its atomic diameter (0.320 nm) ensure that it form a solid solution with a diverse range of elements.

1.2 Magnesium alloys in biomedical field

In general, biomaterials are used to support tissues by taking over their functions after implanting into the body. There are several considerations for element selection in developing newer alloys as biomaterials. The first consideration is elemental toxicity. The degradation product of the designed alloy should be non-toxic and absorbable by the surrounding tissue or dissolved or excreted through the kidneys. The second consideration is the strengthening ability of the elements. The third consideration is the influence on the corrosion behavior. So far AZ31, AZ61, AZ91, AM60, ZK30, ZK60 and WE43 have been extensively investigated. Kannan and Raman (2008) have added REE to commercial alloys such as AZ61, AZ91 in order to improve the corrosion resistance and mechanical properties. In this regard researchers have tried to develop new Mg based alloys with low/no toxicity for biological applications.

From the literature survey it becomes clear that, there are many binary alloys such as Mg-Ca, Mg-Zn, Mg-Si, Mg-Gd, Mg-Zr and Mg-Y that have been developed and investigated for biomedical applications. Selection of appropriate alloying elements have significant effect on properties. Some important elements which are selected for alloying with Mg are briefly discussed here. Zinc (Zn), which is recognized as an element for humans, is usually used in combination with aluminium in magnesium alloys (AZ91, AZ31, AE21, AZ63). It was found that the addition of zinc lowers the melting range of Mg-Al alloys (Zhang et al. 2010). The main phases observed in the Mg-Zn alloys are α-Mg phase and a second phase of Mg-Zn precipitated along the grain boundary. As reported (Bakhsheshi-Rad et al. 2012), the grain size noticeably decreased from 155 to 46 μm with increasing Zn content in the cast Mg-Ca-xZn alloys. Similar result were reported by (Zhang et al. 2009) and (Brar et al. 2012). Zirconium (Zr) is expected to be an effective element for solution strengthening, with low solubility of 3.8 wt. % in Mg and can also be used as a potential grain refining agent during solidification. Zr can reduce the average grain size to about 50 μm at normal cooling rates (Qian and Stjohn 2009). Strontium is a known osteopromotive element that can activate osteoblastic cell replication. Other studies (Li et al. 2012) (Li and Zheng 2013) reported that strontium (Sr) addition can also result in grain refinement.

In the Mg-Sr binary system, the excessive Sr addition leads to the opposite effect i.e., the grain boundaries became coarser and broader.

In order to design magnesium alloys with improved mechanical properties, proper strengthening mechanisms and grain boundary reinforcement studies have to be carried out. Magnesium alloys containing rare earth elements (REE) are a new class of material systems. The designation 'E' in the magnesium alloys represents REE in general. However, yttrium has its own designation letter W. The REE group comprises 17 elements, which can be subdivided into two groups according to their solid solubility in magnesium, indicating their strengthening ability: (i) high solid solubility (Y, Gd, Tb, Dy, Ho, Er, Tm, Yb and Lu); and (ii) limited solubility (Nd, La, Ce, Pr, Sm and Eu) (Feyerabend et al. 2010a). REEs can also be classified into light REE (La, Ce, Pr, Nd and Pm) and heavy REE (Sm, Eu, Gd, Tb, Dy, Ho, Er, Tm, Yb and Lu).

1.3 Magnesium based rare earth element (REE) alloys

Magnesium alloys containing heavy rare earth metals have high strength properties combined with quite low density (1.738 g/cm^3), which makes them very attractive as structural materials in applications where weight saving is of great importance. Addition of REE improves the creep, corrosion resistance and the mechanical properties at both room and elevated temperature. He et al. (2007) developed high temperature resistant magnesium alloys, such as Mg-Zn-Y-Gd-Zr. Further, they achieved effective grain refinement through the hot extrusion process. Liu et al. (2008) reported improved ultimate tensile strength (402 MPa) of Mg-10Gd-2Y-0.5-Zr (wt. %) alloy at room temperature. Studies have reported that the REE containing magnesium alloys would have great applications in aerospace and automotive sectors, which requires low density and high strength materials at high temperatures.

Mg-REE alloys have also been studied explicitly for biomedical applications such as cardiovascular stents and orthopaedic implants applications. Primarily, the advantage of degradation of magnesium alloys is taken into consideration for making absorbable metal stents (AMSs) from modified magnesium based alloys (Li et al.

2008a). Various rare earth element alloyed magnesium alloys such as WE43, Mg-4Y, Mg-5Gd, and LAE442 have been studied and proposed from the perspective of their potential degradability, mechanical properties and cytotoxicity. Many rare earth elements possess anti-carcinogenic properties, but studies have also reported that some REE combinations induce acute toxicity to certain extent (Hort et al. 2010a). Currently, studied Mg-REE based alloys under consideration for biomedical applications include Mg-Y, Mg-Gd, WE43 and so on. Among them, WE43 alloy has been extensively studied for its excellent mechanical properties and corrosion resistance. A newly prepared Mg-Nd-Zn-Zr alloy (denoted as JDBM) alloy outperforms WE43 on mechanical properties and corrosion resistance. Although magnesium based alloys in orthopaedic applications are still in preclinical trials, magnesium based cardiovascular stents have already entered clinical trials in patients. Among the various combinations, Mg containing high soluble REE become more attractive due to their superior properties. Among the REE, gadolinium (Gd) and dysprosium (Dy) have higher solubility and neodymium (Nd) possesses moderate solubility in Mg and these are considered to be potential REE for improving tensile strength, ductility and corrosion resistance. In addition, it is possible to tailor the mechanical and corrosion properties through the control of these alloying elements. In spite of these studies, REE dissolved in magnesium alloys are still limited and their biosafety is still under concern. Hence, it is important to investigate systematically the potential behaviour of Mg alloys containing REE.

1.4 Laser surface melting (LSM)

Due to dynamic environmental conditions Mg alloys also corrode quickly and possess poor wear resistance. These can be controlled by tailoring the surface characteristics such as microstructure and near surface chemical composition. This can be achieved by adopting suitable surface modification techniques. Among different surface modification techniques such as ion implantation, friction stir processing, chemical passivation etc., the use of lasers in the surface modification have made significant progress due to the flexibility in controlling the laser processing parameters. Laser is a source of coherent monochromatic radiation that can be applied for tailoring the surface

microstructure precisely and locally. The principal aim of using laser melting technique is to improve properties through the rapid heating and cooling at the precise area which would homogenize and refine the microstructures in that shallow melted region.

The laser irradiation techniques mainly alter the texture, surface chemistry, morphology and crystal structure of the material. The major advantage of using laser as a tool for material processing is the ability to precisely control the rate of energy is required for depositing the material. A proper selection of laser processing parameters to achieve the desired surface modification need to be optimized by adopting design of experiment techniques. The increasing demand of laser material processing can be attributed to several unique advantages of lasers, which include

- High productivity
- Automation worthiness
- Non-contact process
- Reduced processing cost
- Greater material utilization
- Minimum heat affected zone

Laser processing enables delivery of controlled quantum of energy (1-30 J/cm^2) or power (10^4-10^7 W/cm^2) with precise temporal and spatial distribution either in short pulses or as continuous wave (Olakanmi et al. 2015). The process is characterized by an extremely fast heating/cooling rate (10^4 -10^{11} K/s), very high thermal gradients (10^6-10^8 K/m) and ultra-rapid resolidification velocity (1-30 m/s) (Liu et al. (2005) and Gan et al. (2015)). These extreme processing conditions very often develop an exotic microstructure and composition in the near surface region with large extension of solid solubility. Laser materials processing can mainly be carried out in three ways:

- With melting (surface melting, glazing, cladding, welding and cutting processes require high power density).
- Without melting (transformation hardening, bending and magnetic domain control processes require low power density).
- With vaporization (cutting, drilling, ablation processes require substantially high power density within a very short interaction/pulse time).

One of the major advantages of laser materials processing is the possibility to accurate control the area where laser radiation should be delivered along with the amount and rate of energy deposition. Only the amount of the laser beam energy that is absorbed by the material can contribute to processes like heating and melting. Laser melting of metallic substrates finds wide application due to their precision of operation and production of a fusion zone with high depth/width ratios, minimizing the total amount of material affected or distorted by a laser beam. The absorbed high-energy beam results in a rapid rise of substrate temperature. If the beam intensity is high enough, the increasing surface temperature can exceed the melting point of the substrate material and molten pool is formed on the surface. The front between the liquid and solid phases propagates inside the material as the heat is conducted from the surface into the material bulk, and the surface temperature increases until heat conduction and the heat of melting and evaporation balance the surface energy deposition. The effectiveness of the laser processing is dictated by the energy density, beam dimension, the degree of overlap in tracks and the beam surface interaction time. Considering the size of the bulk substrate, the depth/thickness of the laser surface modified layer is generally very small. The large temperature gradient between the surface and the underneath substrate facilitate rapid quenching and solidification, that could result in microstructural refinement, extension of solubility limit and the formation of non-equilibrium crystalline or amorphous phases depending on the other processing conditions.

The principal aim of laser surface melting (LSM) techniques used in the material surface processing is to improve properties such as wear, erosion and corrosive resistances due to formation of hard, homogeneous and ultra-fine structure at the material surface layer. Metallurgical changes that occur in the laser melted surface layer are in the form of grain refinement, supersaturated solid solutions, and fine dispersion of particles. All these can contribute to the hardening and strengthening of the surface layer. The laser melting can harden alloys that cannot be hardened so effectively by the laser transformation hardening. Studies (Ho et al. 2015b) have showed that by changing the laser melting process parameters it was possible to control the chemical

composition. The scope of improving the wear and corrosion resistance of Mg alloys by bulk alloying is restricted due to segregation of alloying elements, formation of brittle inter metallic phases, and processing cost/difficulty. Furthermore, wear and corrosion are essentially surface related degradation that can be reduced/minimized by appropriate tailoring of the surface micro structure without affecting the bulk. For this purpose a laser beam may be used as a source of heat to melt or clad near the surface region of a substrate to improve the surface properties.

The melted surface layers produces a fine microstructure that reduces the size of galvanic couples and expands the solid solution range of alloying elements. These factors can potentially improve the overall corrosion resistance in Mg alloys. Researchers studied surface melting of Mg alloys such as MEZ, Mg-Zn-Y etc., The results showed that the microstructure of the surface melted zone is characterized by epitaxially grown fine columnar grains at solid-liquid interface and significant improvement in corrosion resistance.

CHAPTER 2

2 LITERATURE SURVEY

2.1 *History of magnesium and magnesium alloys as biomaterials*

The use of magnesium alloys as implant materials were investigated long ago. The renowned physician Edward C. Huse used magnesium wires as ligature to stop bleeding from vessels of three human patients. He further observed that the in-vivo corrosion of Mg was slower and the time period of complete degradation was dependent on the size of the wire used (Witte 2015). One of the pioneering physician Payr proposed that oxygen tissue, water content, carbon dioxide, the dissolved salts in blood and chemical processes in cells were mainly responsible for the in vivo corrosion of Mg. Even though it is used as a ligature Mg cannot be tied or twisted because of its brittle nature. Furthermore Seelig 1924 found that noble metals must be alloyed with magnesium increases its ductility. Later on Gotthard Gossaru patented a Mg rope with better tensile strength and stiffness. Andrews 1917 proposed absorbable Mg clips and staples that can be used for closing the vessels (closure for wounds). It was reported (Witte 2010) that Mg could be only implanted without combining it with other metallic implants to prevent electrolytic corrosion. Zierold (1924) compared the reaction of various metals on bone tissues and concluded that Mg has little action other than as a connective tissue stimulant and hypothesized that it may accelerate new bone production. In the review article (Witte 2010) it was documented that , Nicole surprisingly observed low corrosion rate of pure Mg in bone and an almost complete corrosion after 2 months. Compared to other metals, the long term storage of metallic corrosion products in bone could not be observed for magnesium. The advantages and obvious benefits of biodegradable metal implant studies are still awakening the curiosity of many researchers for further biomedical applications.

2.2 *Recent developments of Mg alloys for biomedical applications*

In spite of the immense potential of biodegradable magnesium alloys, the fast degradation rates of Mg-based implants in physiological environment impose several limitation in many clinical applications. Stainless steel, Co-based alloys and titanium

alloys are widely used in hard tissue implants, especially in load bearing applications due to their strength, ductility and good corrosion resistance (Seal et al. 2009). With regards to bio-medical implants such as plates, screws and pins, Witte et al. 2008 reported that it is desirable to use a material that can degrade in the physiological environment so that subsequent surgical procedure to remove the implants from the human body after the tissue have healed is not necessary. Magnesium and its alloys are chemically active and can degrade naturally in the physiological environment by corrosion. Mg^{2+} is the fourth most abundant cation in the human body and is largely stored in the human bone tissue. Also the recommended daily intake of Mg for adults is 240-420 mg/day, which is 52.5 times more than that of other essential elements like iron and zinc (Staiger et al. 2006). Troitskii and Tsitrin (1944) reported that Mg based implants have good biocompatibility based on *in-vivo* and *in-vitro* testing. The unique mechanical properties of magnesium alloys also render them desirable for hard tissue implants. Magnesium alloys possess a density of 1.7-2.0 gcm^{-3} that is closer to that of natural bones (1.8-2.1 gcm^{-3}) while the compressive and tensile strength are much higher than those of biodegradable polymers. Compared with Ti alloys (110-117 GPa), stainless steel (189-205 GPa) and Co-Cr alloys (230 GPa), the elastic modulus of magnesium alloys (41-45 GPa) is closer to that of natural bones. Hence Staiger et al. (2006) commented that stress shielding effect induced by serious mismatch in the elastic moduli between natural bones and Mg implants can be avoided.

The recent technological advances in developing high purity magnesium with high mechanical and corrosion performance has further, renewed interest in using Mg-based alloys in biomedical application. Heublein et al. (2003), took advantage of the degradation behaviour of magnesium alloys to develop cardiovascular stents. BIOTRONIX has manufactured absorbable metal stents (AMSs) (Zheng et al. 2014 from WE43 and modified Mg based alloys. Various possible applications of magnesium implants are briefly listed out in **Figure 2.1**. Zartner et al. 2005 conducted clinical trials which have shown no symptoms of allergic or toxic reactions to stents they have degraded completely and safely after 4 months.

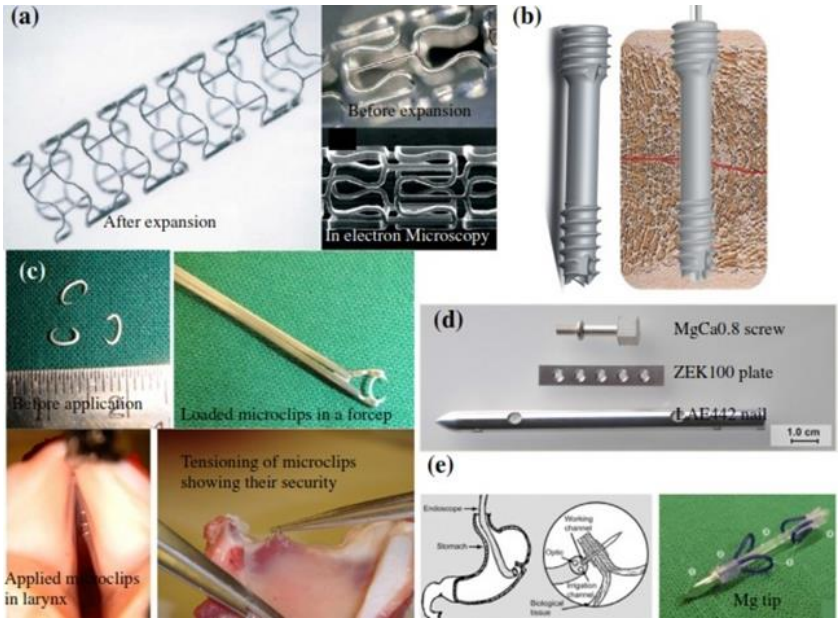

Figure 2.1 Real/possible applications of biodegradable magnesium implants (a) cardiovascular stents (BIOTRONIK, Germany) (b) MAGNEZIX screw (c) Micro clip for laryngeal microsurgery (pure Mg) (d) orthopedic plates and screws (e) wound closing device (Chen et al. 2014)

It has been reported that alloying elements such as zinc (Zn), calcium (Ca), zirconium (Zr) and rare earth elements (REE) can effectively improve the mechanical and corrosion properties of Mg (Seal et al. 2009). In this regard, several binary alloys such as Mg-Ca (Li et al. 2008b), Mg-Zn (Zhang et al. 2011), Mg-Si (Gao et al. 2009) , Mg-Zr (Mushahary et al. 2013), and Mg-Y (Peng et al. 2010) have been investigated, in both *in vitro* and *in vivo* conditions, for biomedical applications. However, these binary alloys were found to have poor yield strength and too high corrosion rates (Li et al. 2008b), (Peng et al. 2010). Few Mg alloys, containing Zn and Ca such as Mg-3Zn, Mg-1Zn-1Ca and Mg-5Ca, have been proposed for biodegradable implant applications (Li et al. 2008b; Wan et al. 2008). Among all the different alloying elements, only few are discussed in the subsequent sections.

2.3 *Mg-Zn based alloy systems*

Recently Mg-Zn alloys have attracted great interest because of higher strength, better ductility and corrosion properties. The addition of Zinc (Zn) to magnesium promotes solid solution strengthening and grain refinement. The maximum solubility of Zn in Mg is 7.57 wt.% at 341 °C and decreases to around 1.6 wt. % at room temperature. Cai et al. (2012) studied the effect of Zn (0-7 wt.%) addition to Mg on microstructure, mechanical properties and corrosion behaviour of the as cast Mg-Zn. Results proved that the improvement in mechanical properties at 5 wt.% Zn addition mainly corresponds to fine grains strengthening, solid solution strengthening and secondary phase strengthening. Also, Mg-5Zn alloy exhibits enhanced corrosion resistance. But further addition of Zn content beyond 5 wt. % promotes the galvanic couple effect and thereby increases the corrosion rate. The addition of Zn also act as a potent grain refiner. It is reported that, in Mg- Ca-xZn (Cao et al. 2005) system grain size notably reduces from 155 to 146 μm with increasing Zn content. Boehlert and Knittel (2006) investigated Mg-Zn (0-4.4 wt. %) and the results summarize that the microstructure consisted of equiaxed hexagonal close packed grain and fine lath within the grain with the precipitates preferentially located at grain boundaries. The measured finer grain size was observed for 4 wt. % Zn composition and better tensile and creep properties were observed for 4.1 wt. % Zn with small amount of yttrium (Y) addition.

The effect of Zn addition (2-5 wt.%) on the corrosion behavior on Mg-xZn binary alloy was studied by Song et al. (2012a). It was observed that increase in Zn addition increases the formation of higher volume fraction of secondary phases leading to higher anodic dissolution and cathodic hydrogen evolution rates. The maximum corrosion rate was observed for Mg-5Zn and this drop in corrosion resistance was mainly due to the micro cathodic effect of the secondary phases (Mg_xZn_y). Further (Song et al. 2012b) carried out heat treatment (T6,T4) of Mg-5Zn alloy to understand the role of secondary phases on the corrosion behavior. The results showed that T4 samples exhibit better corrosion resistance than as received and T6 samples. It was observed that the distribution of secondary phases adjusted by the heat treatment and the absence of secondary phases in T4 condition leads to better corrosion resistance.

Cha et al. (2013) investigated tailoring of electrochemical properties and microstructure of constituent phases by adding Zn to Mg-Ca alloy system as a biodegradable materials. It is revealed that the addition of Zn prevented the formation of micro galvanic couples and achieved a comparable corrosion rate with high purity Mg. Addition of more than 1 wt.% could not greatly improve the corrosion resistance. The greater reduction of hydrogen evolution was observed in both *in-vivo* as well as *in-vitro* studies of Mg-Zn-Ca alloy. The understanding of alloying elements Ca and Zn interaction on degradable magnesium has been studied by Zander and Zumdick (2015). The changes in Ca and changes in both the elements (Ca and Zn) show distinct effects. The ternary systems such as Mg-0.6Ca-0.8Zn, Mg-0.6Ca-1.8Zn showed enhanced corrosion resistance and they were evaluated as most suitable for implant application.

2.4 *Magnesium based Rare Earth Element (REE) alloys*

The next series of alloying elements which are critical for tailoring the properties of Mg are rare earth element (REE). The REE containing Mg alloys are carefully observed by various researchers. These different REE have been studied by various researchers. When it used as a constructional material the primary consideration is mechanical properties. In the biomedical field, the focus is on tailored alloys with adjustable corrosion and mechanical properties. Magnesium alloys with highly soluble REE become more applicable because of its improved properties such as corrosion behaviour and biocompatibility. Therefore, the development of Mg-REE-based alloys as biodegradable materials have attracted significant interest in recent period. Magnesium alloys with high and medium solubility REE such as gadolinium (Gd), dysprosium (Dy) and neodymium (Nd) have been the subject of several scientific investigations, as REE additions are very effective for strengthening. The discussions in the subsequent sections are based on the major REE elements especially Gd, Dy and Nd, which are studied with the focus on improving the corrosion, mechanical and biocompatibility properties when they are alloyed with Mg.

2.5 *Mg-Zn-Gd based alloy system*

Gadolinium (Gd) is one such REE being investigated for the possibility of developing new magnesium alloys with a good combination of mechanical and corrosion properties. Gd has high solubility (Yang et al. 2008) (23.5 wt. % at eutectic temperature) in magnesium. **Figure 2.2** (Hort et al. 2010) shows the binary phase diagram of Mg-Zn-Gd alloy system. As a single alloying element, Gd is present in solid solution, and can be shown to be a potential element for improving the mechanical properties of Mg alloys because its microstructure consists of different phases depending on the ratio of Zn to Gd content. Therefore, the mechanical properties of these alloys can be tailored accordingly by altering the Zn and Gd concentration. Many experimental alloys such as Mg-Gd-Y(Honma et al. 2007), Mg-Zn-Gd-Nd (Zhang et al. 2012b), Mg-Gd-Zn (Srinivasan et al. 2014a), and Mg-Gd-Y-Zn (Wu et al. 2013) systems have been developed, and their microstructure, and mechanical and corrosion properties have been investigated.

The mechanical properties of heat treated and extruded Mg-Zn- Gd alloy significantly affected by the formation of long period ordered (LPO) structure and it is later represented as long period stacking ordered structure (LPSO). This novel structure is the strengthening phase in the developed Mg-Zn-REE alloys. The heat treatment mainly aided to precipitate the LPO formation and the extrusion process helps to refine the grains effectively. The combination of these 14H-LPO phase and fine grain structure leads to high tensile yield strength, and large elongation (Yamasaki et.al 2005). So the Mg-Zn-Gd alloy is a one of the main candidate for novel high strength with LPO structure. Yang et al. (2008) investigated the effect of Gd addition up to 5 wt. % on the microstructure and mechanical properties of Mg-4.5Zn alloy. The results reported that optimum tensile properties were observed at 2 wt. % Gd, and identified only LPSO-W phase in all these alloys. Kim and Park (2011) reported the presence of W phase in Mg-Zn-Gd alloys, and found that maximum tensile strength occurred at 1-2% Gd addition. LPSO phases are also present in high Gd containing Mg-Gd-Zn systems, which enhances the mechanical properties.

Srinivasan et al. (2014) investigated the microstructure, mechanical and corrosion properties of Mg-xGd-2Zn alloy with x=2, 10 and Mg-2Gd-yZn with y=2, 6 wt. %. The Mg-10Gd-yZn alloys (y = 2,6) exhibited higher yield strength due to the higher solute contents and the presence of LPSO phase in the matrix, but showed poor elongation due to the coarse continuous second phase at the boundary. Low Gd containing alloys showed better elongation to failure and moderate strength due to the lower volume fraction of secondary phases. Corrosion resistance of the alloys decreased with increase in the total amount of alloying elements. Increase in Zn content from 2% to 6% in Mg-2Gd-yZn alloys could not change the corrosion behaviour to large extent. However, this increase in the high Gd content in alloys have detrimental effects on the corrosion properties due to the significant increase in the volume of the second phases.

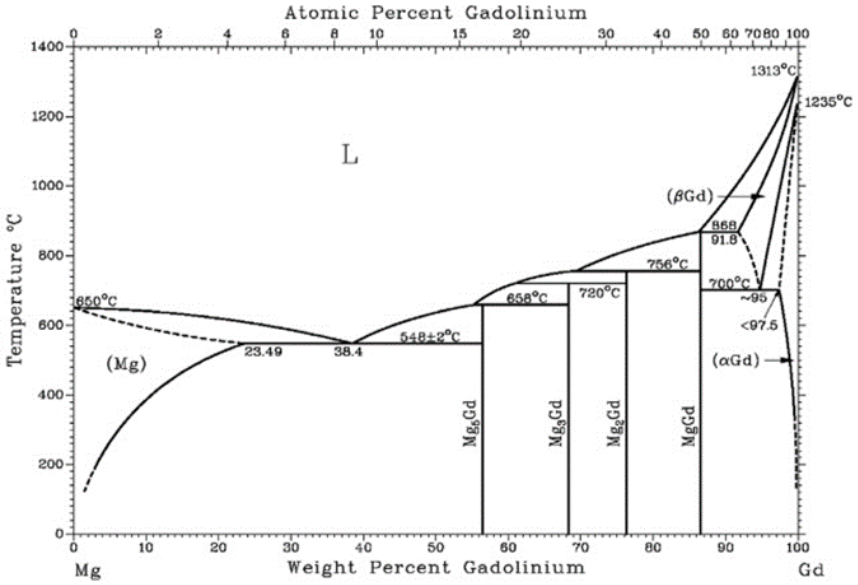

Figure 2.2: Mg-Gd Phase diagram (Hort et al. 2010)

2.6 *Mg-Zn-Dy based alloy system*

The high solid solubility (25.3 wt. %) (Bi et al. 2014) of element dysprosium (Dy) in Mg makes it possible to adjust both mechanical and corrosion properties through the control of Dy content or heat treatment. The phase equilibrium and thermodynamic data of Mg-Dy alloys were investigated and reported by various authors. All the binary

phase can also be seen in the **Figure 2.3**. Dy is also considered as a potential alloying element for the design of new Mg-REE based implants. Peng et al. (2009) studied the structure stability and strengthening mechanism of Mg-Gd-Dy-Zn die cast alloy. Their results mainly emphasised that the microstructure mainly composed of fine cellular equiaxed grains with lamellar stacking compound. The formation of small grain boundaries, stable skin region and precipitates are the reason for the enhanced mechanical properties. Bi et al. (2011) studied the microstructure and mechanical properties of the extruded Mg-2Dy-0.5Zn alloy. The formation of 14H LPSO phase with fine grained α-Mg matrix was observed. The higher volume fraction of LPSO phase leads to the better ultimate tensile strength with high thermal stability.

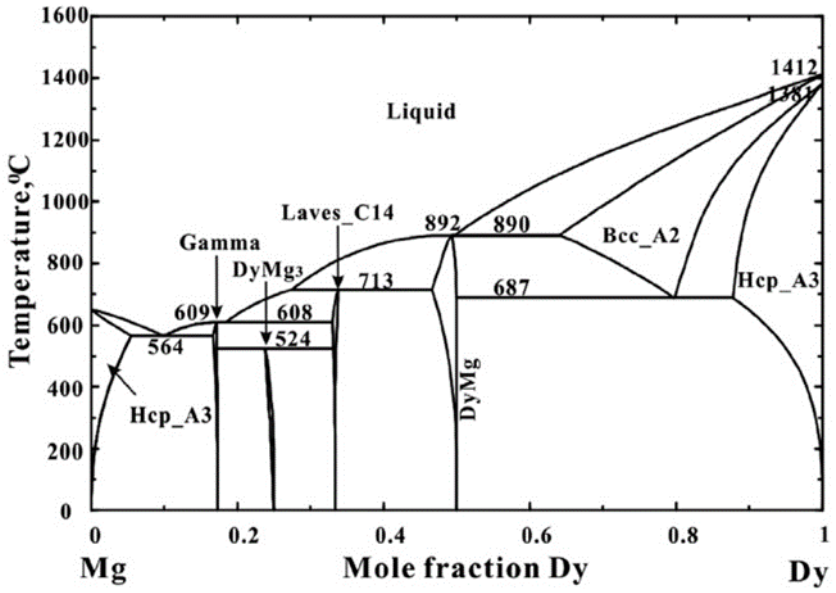

Figure 2.3 Mg-Dy Phase diagram (Bi et al. 2014)

The short-term effects of REE and other elements used in magnesium alloys on primary cells were studied (Feyerabend et al. 2010). In this study, the in vitro cytotoxicity of the elements yttrium(Y), neodymium (Nd), dysprosium (Dy), praseodymium (Pr), gadolinium (Gd), lanthanum (La), cerium (Ce), europium (Eu), lithium (Li) and zirconium (Zr) were evaluated. Out of all the elements Gd and Dy seem to be more suitable than Y, La and Ce. As an overall finding light rare earth elements (La, Ce, Pr) showed higher cytotoxic effect and Nd, Eu, Pr suitable with addition of lower

concentration. Yang et al. (2011) investigated several Mg-Dy alloy with varying Dy composition (5, 10, 15, 20 wt. %) for biomedical application and these alloys were prepared by casting. Results showed that increasing addition of Dy widely tailored the mechanical and corrosion properties. Heat treatment of this Mg-Dy further modified the properties. Among various compositions tried, Mg-10 Dy is identified as potential candidate for biomedical applications. Bi et al. (2014), in a study varied the composition of Zn (x=0, 0.1, 0.5, and 1 at. %) by keeping the Dy constant (Mg-2Dy-xZn). The corrosion results indicated that Mg-2Dy-0.1Zn alloy showed better corrosion resistance and it is mainly due to the uniform distribution of secondary phases. Mg-2Dy-0.5Zn alloy exhibited the higher tensile strength and good elongation. The improvement in mechanical properties was mainly by the strengthening of LPSO phase and grain refinement of α-Mg. Most of the work related to Dy in the literature has focused on investigation of mechanical and corrosion properties which are mainly influenced by the morphology, scale and stacking order of the phases formed in the alloy.

2.7 *Mg-Zn-Gd-Nd based alloy system*

Mg-Nd (Neodymium) based alloy shows a significant level of metastability of secondary phases. Based on the developed thermodynamic data from the phase diagram, different phase selections at different temperature regime is well described (**Figure 2.4** (Okamoto 2013)). Mg-Nd alloy has greater tendency to age hardening due to its maximum solid solubility and that leads to greater super saturation of solute during the solidification (Easton et al. 2012). Different aging treatment effectively improves the properties of Nd based alloys in terms of mechanical and corrosion properties. Zhang et al. (2012c) developed a new Mg-Nd-Zn-Zr (JDBM) alloy extruded with different ratios and also subjected to ageing treatment. The complete dynamic recrystallization after extrusion leads to better strength with moderate elongation and improved corrosion resistance. Further ageing of optimised extruded sample shows further improvement in strength as well as corrosion resistance.

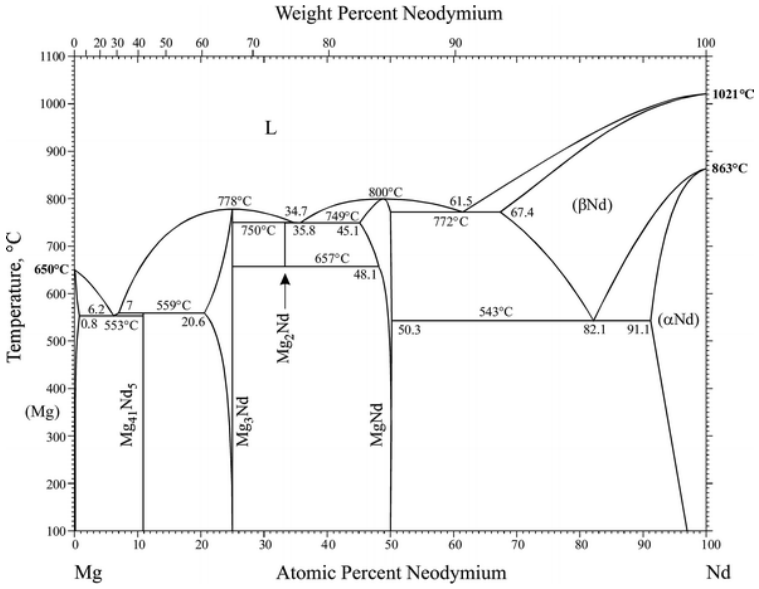

Figure 2.4 Mg-Nd phase diagram (Okamoto 2013)

The short term cytotoxicity study of this alloy meets the requirement of cell cytotoxicity and can be recommended for the biomaterial applications (Zhang et al. 2012c). The *in vivo* corrosion and antibacterial studies (Qin et al. 2015) on the JDBM alloy showed that proper amount of alloying elements (Zn, Nd, Zr) resulted in enhanced corrosion resistance, biocompatibility and antibacterial activity. The addition of Nd to the Mg-Zn based alloy followed by heating and extrusion process. The extrusion process resulted in refinement of grains and formation of stable high temperature dense phases. These different precipitate phase combinations attribute the enhancement of strength in the alloy (Hu et al. 2015). The corrosion behaviour of Mg-Nd-Gd-Zn-Zr was studied by passivation kinetics under heat treated condition (Ninlachart and Raja 2017). Results showed that the uniform distribution of REE in the solution treated alloy exhibits better passivation behaviour. Suitable mechanical properties are needful for the Mg based degradable alloy as a supporting structural material. To this end Gui et al. (2018) investigated Mg-Nd-Zn-Zr alloy under as cast and as extruded condition. The superior mechanical properties at hot extruded condition were mainly attributed to the eutectic compound with dispersed nano precipitates that supports the solid solution strengthening, grain boundary strengthening and precipitation strengthening.

Further, in addition to alloying different elements with Mg, researchers have also reported that it is necessary to carry out secondary processes such as plastic deformation and coating for further improving the properties of Mg based alloys.

2.8 *Laser surface modification of magnesium alloys*

In general, the purpose of heat treatment is to controlled heating and cooling of materials to change their mechanical and physical properties without changing the initial dimension of the product. The use of laser processing is an alternative technique for modifying the surface because of effective control of high intensity beam at short duration of time in near surface. The dominant laser process parameters for the surface modification comprises laser power, beam diameter and beam energy absorption by the treated material, scanning velocity and the thermal properties of the treated material. This process is completely suited to execute on localized area because the laser beam is finite in size. The laser surface melting is carried out as multiple scans with a small degree of overlap. The width of the scan layer is controlled by the dimensions of the laser beam. Microstructural variations at the near surface region due to the induced heat, influenced the electrochemical characteristics of the alloy. The remelted layer in Mg alloys are enriched with other alloying elements mainly due to the evaporation of magnesium from the surface. In the case of AZ91D and AM60B alloys the laser surface melted (LSM) layer has been enriched with Al to about 11-12% and 8-9% respectively (Dubé et al. 2001). The Al enrichment at the surface may either improve the β-phase volume fraction or could support solid solubility enhancement of Al in the matrix. It is believed that oxide film formed on the rapidly solidified alloys containing higher amount of Al in solid solution may provide better passivating behaviour.

Abbas et al. (2005) found that the corrosion resistance of AZ61, WE43 and AZ31, alloy could be significantly enhanced by LSM. The improved corrosion resistance in LSM is due to the reduced galvanic effect, that is mainly attributed to the grain refinement and uniform distribution of secondary phases. Liu et al. (2005) carried out LSM on Mg, alloyed with Al, Zn, Mn and Ce, by pulsed Nd: YAG laser. The results indicated that overall corrosion performance of laser melted sample is much better when compared

to as cast sample and hardness of the LSM zone is increased two times compared with the matrix. The finer dendritic microstructure in the treated zone is the main cause for the improved performance. The use of CO_2 laser with different laser powers and scan speed resulted in extremely fine grained surface, leading to an increased microhardness and corrosion resistance (Gao et al. 2007). However, LSM of AZ91D and AM60 (Dubé et al. 2001) alloys using a pulsed Nd-YAG laser resulted in an increased corrosion rate. Formation of Al rich curled bands with non-uniform microstructure were the assessed reason for the higher corrosion rate. Excessive heat during the LSM promote the formation of secondary phase and followed slow cooling may increase the grain size. But it is anticipated that inherently high cooling rate would improve the corrosion rate due to the resulted shallow melted zone which is free from constituent particles. Similarly, LSM of ZE41 alloy also concluded that there is no improvement in the corrosion resistance (Banerjee et al. 2011).

A major concern in LSM is to achieve surface strengthening by reducing micro segregation and microstructure refinement. During the LSM of Mg alloy, the thermal field plays an important role in determining microstructures and surface performance. The processing parameters like laser spot size, laser power, scanning speed, and scanning strategy all play crucial roles on the development of temperature gradients and the morphology of the melt pool. So these parameters influence the changes in cooling rate and thereby improve the performance of the material. LSM on WE43 alloy with different scanning speeds at constant energy density by excimer laser was studied (Guo et al. 2005). Under these conditions, at lower speed full melting and at higher speed partial melting of secondary phase ($Mg_{12}Nd$) was observed. The lower anodic and cathodic corrosion current at lower velocity leads to the improvement in corrosion resistance. However, the laser treated samples showed better corrosion resistance than untreated alloy. At low energy input selective melting of the surface resulted in modification of only one phase of the alloy and effective melting of phases were reported at high energy input. It was also observed that the depth of treatment was insensitive to scan velocity at high laser power (Taltavull et al. 2013). In another study, the corrosion rate of laser melted AZ91D was found to increase with an increasing laser power and decreasing laser scanning speed (Taltavull et al. 2014). Gan et al. (2015)

carried out numerical study of thermal characteristics during laser surface melting of AZ31B with different process parameters. The temperature gradients and cooling rates during LSM were predicted through simulation. The average heating and cooling rate and the dimension of the melt pool at various laser powers and scanning speed were predicted. Finally, the simulation results showed good agreement with the experimental measurements.

For implant applications, surface characteristics of these alloys play an important role in protein absorption and cell/osteoblast growth (Ho et al. 2015a). The quality and amount of cells that attach on to the surface are substantially influenced by the surface characteristics such as roughness, chemical composition, surface energy and compositional heterogeneity of the surface (Rosales-Leal et al. 2010). For example, nanoscale surface roughness of Ti was demonstrated to be very effective in enhancing osseo integration (Rupp et al. 2004). Osteoblast proliferation and differentiation as well as production of local growth factors are also influenced by surface roughness. Guan et.al found that AZ31B alloy surface modified using femtosecond pulse laser irradiation causes micro and nano ripples. The combined effect of surface roughness and interference of laser leads to the surface topographical changes in the alloy (Guan et al. 2013). Use of ns-pulsed fiber laser for surface melting of AZ31B alloy led to changes in surface roughness as well as mechanical properties. It is concluded that control in laser process parameters allows changes in surface roughness values (Ra). Surfaces with monodirectional, homogenous and nano fibrous structure were observed after melting (Furlan et al. 2015). Wettability is another important surface property that dictates biological interaction through cell adhesion on the surface (Dean 1996). The nature of the water contact angle on laser surface textured AZ31, with cauliflower type of surface roughness, were found to be hydrophilic and is mainly attributed to the surface topography and chemistry (Demir et al. 2014). Surface energy is generally directly related to the wettability of a surface (Rosales-Leal et al. 2010). The materials with high wettability/ surface energy (hydrophilicity) promote rapid cell adhesion, growth and better biocompatibility (Janssen et al. 2004). Therefore, the surface wettability of an implant material helps in estimating the overall cell-materials interactions and long term or short term stability (Baier 2006). The results showed that

laser treatment is a promising technique for tailoring biodegradation behavior and wettability of Mg alloys by changing the surface structure (Gökhan et al. 2015). In this context, laser surface modification is very efficient for phase modification, grain refinement on the surface without changing the bulk properties of the material (Kurella et al. 2008).

2.9 *Summary of literature survey*

Recent studies showed that significant progress has been made in the development of Mg based alloys as a bioresorbable material for implant application. The design method for the next phase alloys need materials with desired mechanical properties, corrosion resistance and excellent biocompatibility. Further research should focus on development of Mg alloys with tailored properties through various approaches including alloying and suitable surface modification.

Studies in the literature reveal that adding REE to Mg has resulted in enhanced the corrosion resistance, strength and ductility. Such effective outcome of the addition of REE is believed to be because of

- REE lower the impurity effect caused by elements in Mg alloys, by acting as a barrier and precipitating new intermetallic phases.
- REE is reduce the other intermetallic phase volume fraction and cover up micro galvanic corrosion effect.
- REE refine the α-Mg grains and secondary phases, leading to much homogeneous microstructure.
- REE decrease the defects in crystallographic structure caused after deformation, and decreases the anodic dissolution percentage in alloys.

From the literature review, it is evident that mechanical and corrosion properties can be fine-tuned in a broad range by changing the content and composition of alloying elements. Based on the solubility limit in Mg and compatibility with human body, dysprosium (Dy), gadolinium (Gd) and neodymium (Nd) have been selected as element for alloying Mg.

The previous studies based on the laser processing of Mg alloys recommended that there is ample scope of expanding it further in terms of improving the surface properties. Due to rapid heating and cooling that occurs in the laser treatment the composition of the surface will be homogenized and the distribution of secondary phases can be controlled at the material surface. There are persisting problems such as micro cracks that need to be addressed controlled during the melting of magnesium alloy.

2.10 Objectives of the study

Looking at the ample scope in the field of magnesium alloys and its surface modification by laser surface melting the following objectives have been identified.

- To develop Mg-Zn based alloys with addition of REE such as gadolinium (Gd), dysprosium (Dy) and neodymium (Nd). The proposed alloy systems are processed through casting route and their compositions are as follows
    a. Mg-1%Zn-2%Gd (in wt. %)
    b. Mg-1%Zn-2%Dy (in wt. %)
    c. Mg-3%Zn-1.5%Gd-1.5%Nd (in wt. %)
- Laser surface melting of the developed alloys by using laser beam of LENS^{TM}, MR-7 equipment from Optomec Inc, USA in a high purity argon purged glove box. Different laser powers (125, 175, 225 W) were used at scan velocities of 10 and 20 mm/s to achieve different laser energy densities (12.5, 17.5, 22.5, 25, 35, 45 J/mm^2)
- Characterize the as cast and laser treated alloys with respect to microstructure and mechanical properties.
- To understand the cytotoxicity behaviour of as cast alloys.
- Understand the roughness changes and wettability behaviour of laser processed alloys at different laser energy density conditions.
- Investigate the *in-vitro* degradation behaviour of as cast and laser melted alloy samples under suitable physiological environment. Further, perform the

microgrpahy of corroded surfaces and products to understand the mechanism of degradation.

2.11 Outline of the thesis

Each chapter in this thesis contains a systematic study conducted with respect to the defined objectives. A brief skeletal structure of the thesis along with summary of five chapters are as follows.

Chapter 1 starts with a brief introduction to Mg alloys, application of Mg alloys in different sectors. Here Mg based REE alloys which are the focus of this work are also introduced. This chapter concludes with an introduction to LSM.

Chapter 2 contains an extensive literature survey to understand the work carried out in the proposed field. Based on the literature gap, objectives of the work are formulated and listed out at the end of the chapter.

Chapter 3 focuses on the description of various equipment and materials used for casting and laser surface melting of Mg-Zn-REE based alloys. Following which, the various techniques used for analysis of microstructural features, mechanical properties, wettability, cytotoxicity and corrosion behaviour of as cast and laser melted alloys are described in detail.

Chapter 4 presents the results of the various tests conducted to evaluate the performance of the laser treated and untreated alloys. This chapter is divide into 4 sub sections where in the first sub section explains about the results of as cast alloys (Mg-Zn-Gd, Mg-Zn-Dy and Mg-Zn-Gd-Nd) and their conclusions. The following sub sections separately discuss the each laser melted alloy (Mg-Zn-Gd, Mg-Zn-Dy and Mg-Zn-Gd-Nd) with key conclusions.

Chapter 5 highlights the overall conclusions drawn from the results presented in this thesis and future scope of work.

CHAPTER 3
3 MATERIALS AND METHODS

3.1 Methodology

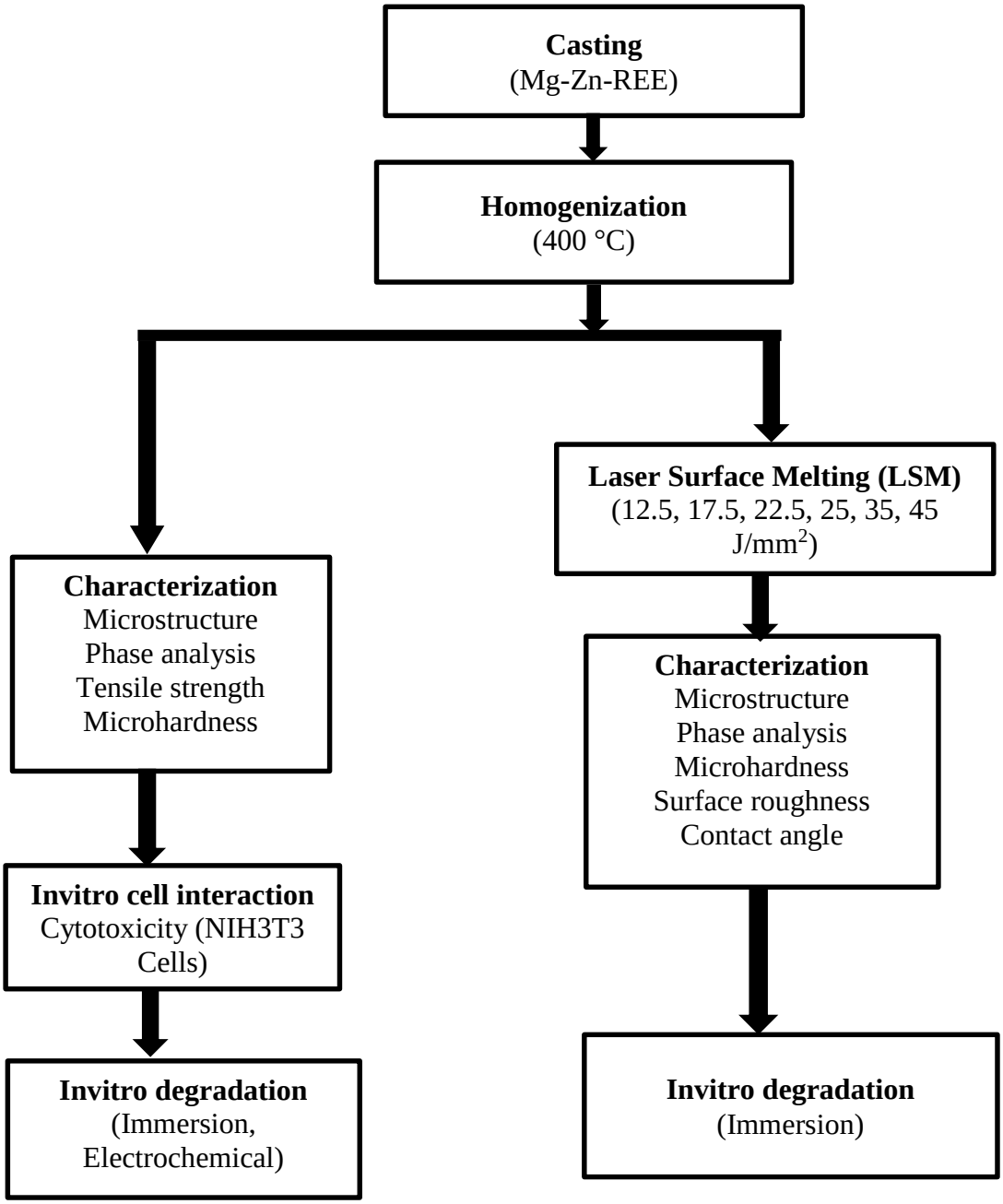

3.2 Casting of alloys

The rare earth alloying elements (99.9 wt. % purity) namely Dy, Gd, and Nd were procured from Metal Industries, Mumbai, India. Three alloys namely Mg-Zn-Gd, Mg-Zn-Dy and Mg-Zn-Gd-Nd were casted in a mild steel crucible under a protective atmosphere (Ar + 2% SF_6). Mg and Zn melts were prepared and pure Gd, Dy or Nd were added to the melt at 750 °C to the get the compositions. In addition to the REE, 0.7 wt. % of Zr was also added to the molten alloy as a grain refiner. After holding for 20 min, the melt was stirred for 2 min for compositional uniformity/homogenization followed by pouring into a preheated (250 °C) cast iron mold (200 × 110 × 20 mm). The solidified magnesium alloy block was taken out from the mold after the required curing time. The detailed view of magnesium casting unit facility is shown in **Figure 3.1**.

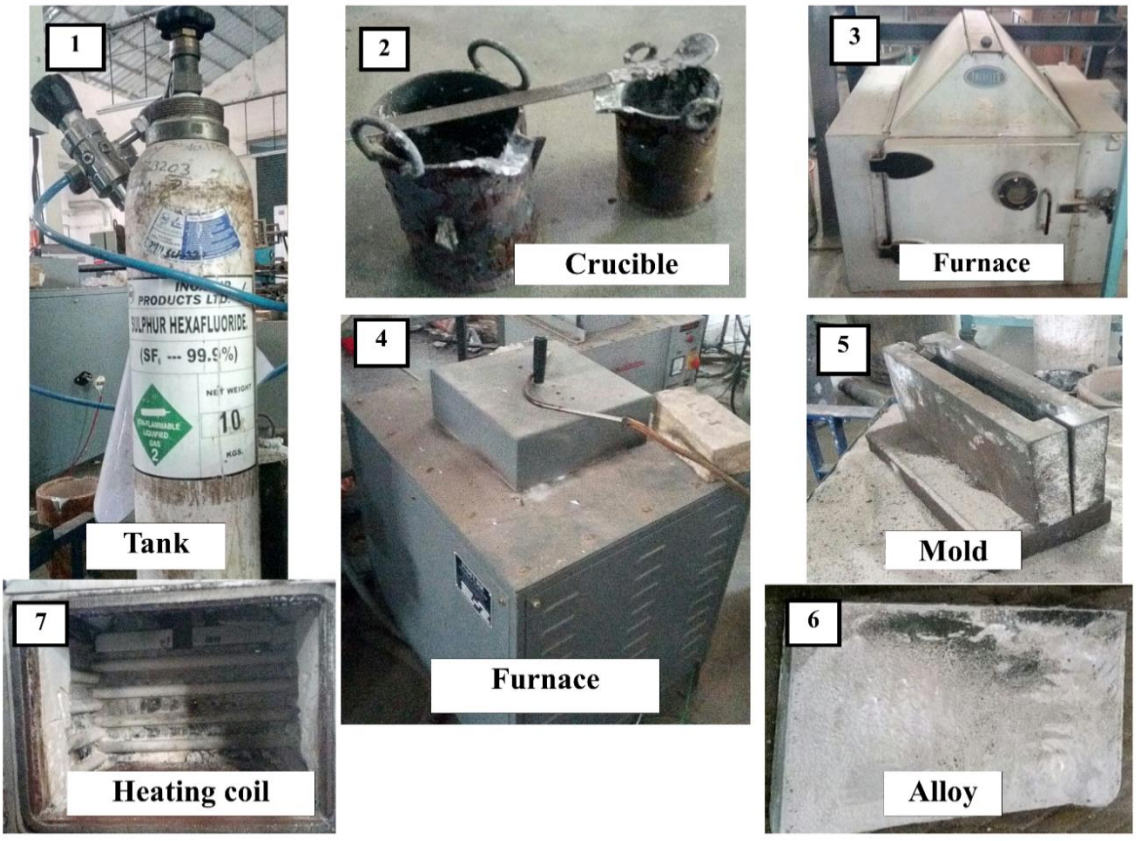

Figure 3.1 Magnesium casting facility (Courtesy: CSIR-NIIST)

The casting unit mainly consists of following parts

1. Sulphur hexa fluoride tank- It is used for providing a protective environment for the casting.
2. Crucibles and Stirrer - Crucibles are used for keeping the magnesium blocks inside the furnace for melting and stirrer for proper manual stirring of molten liquid during the melting.
3. Preheating furnace - To preheat the mold before pouring the molten metal.
4. Furnace - Melting of magnesium blocks and rare earth elements were carried out in this melting furnace. The furnace is being purged with Ar+2% SF_6.
5. Mold- After melting in the furnace the molten pool is poured into the square mold
6. Alloy block- Final moulded alloy
7. Heating coil-To provide a desired temperature condition to the furnace.

3.3 Laser Surface Melting (LSM) of alloys

The cast alloy (Mg-Zn-Gd, Mg-Zn-Dy and Mg-Zn-Gd-Nd) blocks with 90 *mm* × 20 *mm* area were used for laser surface melting (LSM). Before the laser melting process, the cast alloys slab were homogenized at about 400 °C, (which is the recrystallization temperature) for 24 hours in the furnace for producing a refined micro structure. The homogenized alloy coupons were first sized by belt polishing machine and later the sample surfaces were ground using SiC abrasive papers ranging from grade 220 to 2000 (grit size). Finally, all prepared samples were cleaned with toluene and ethanol. The selection of the laser processing parameters were decided by carrying out a number of experiments within the range of machine capacity. Laser power and scan velocity are the major parameters which affect the depth and width of meltpool during surface melting. LSM was carried out using the laser of LENS^{TM} equipment (MR7, Optomec Inc. USA) in high purity argon purged glove box with oxygen content is less than 10 ppm. A continuous wave Ytterbium doped fiber laser with beam diameter of 500 μm and wavelength of 1064 nm was used for LSM. In LENS^{TM}, the nozzle and laser delivery assembly can move in positive Z direction and the CNC table beneath the assembly moves in the X and Y directions. The metal samples for melting were fixed

on the CNC table. During melting, the CNC table moves in X and Y directions according to the each laser pass information. The schematic representation of laser surface melting represented in **Figure 3.2** and the experimental set up is shown in **Figure 3.3.**

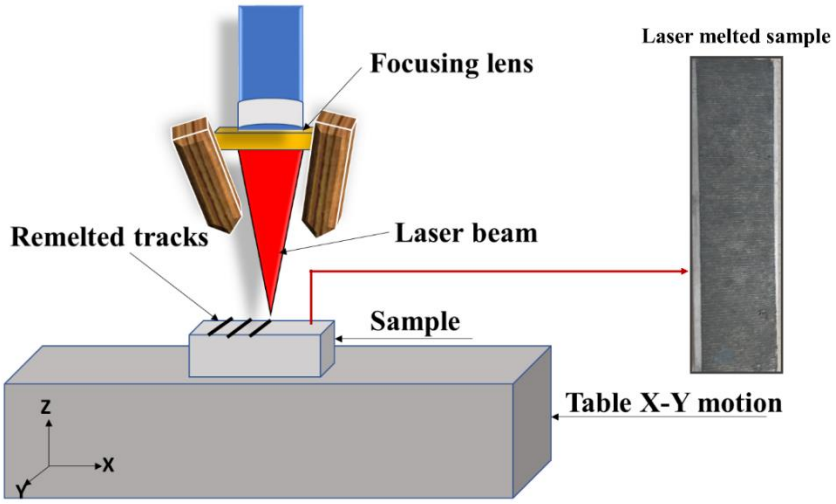

Figure 3.2 Schematic representation of laser surface melting

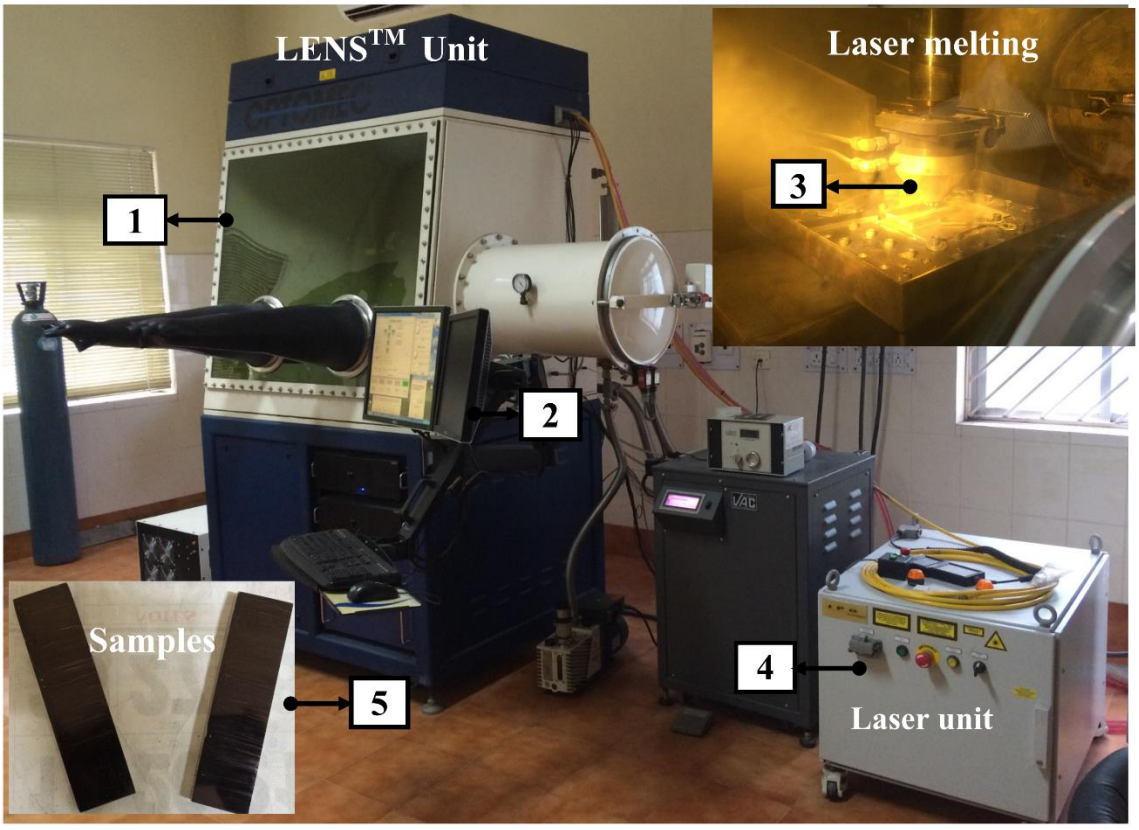

Figure 3.3 Experimental setup of LENS™ system

The main components of the LENS^{TM} system are marked in **Figure 3.3** and are listed below.

1. Glove box
2. Computer controller
3. Nozzles
4. Laser unit
5. Samples for laser melting

Different laser powers and scan velocities are used to achieve different laser energy densities .The energy density calculated as

$$\mathbf{E = \frac{P}{v.d}} \qquad \textbf{3-1}$$

Where P is laser power (W), ν is scan velocity (mm/s) and d is laser beam diameter (500 μm). The distance between two successive laser scans was maintained at 0.5 mm. The convention used to represent laser processing condition is as follows, a combination of 225 W power and 10 mm/s scan velocity is represented as 225/10 throughout this thesis. **Table 3.1** shows the laser processing parameters used in this study.

Table 3.1 : Parameters used for laser surface melting

Power (W)	**Velocity (mm/s)**	**Energy density (J/mm^2)**
125	10	25
125	20	12.5
175	10	35
175	20	17.5
225	10	45
225	20	22.5

3.4 Microstructural characterization

Microstructural analysis was done on both as cast and laser melted samples to study the intermetallic phase distribution, grain refinement and bonding quality. All the laser melted samples were sectioned perpendicular to the laser tracks for microstructural studies. Small sections of the samples were cold mounted with the help of acrylic powder and resins. The encapsulated samples were polished using a series of silicon carbide (SiC) papers up to 2000 grit followed by fine polishing on velvet cloth using superfine diamond paste (0.25 µm). The polished samples were etched with a solution of 97 ml alcohol and 3 ml HNO_3. The microstructures and local composition of the alloys were analyzed using

- Optical Microscope (OM)
- Scanning Electron Microscope (SEM)
- Transmission Electron Microscope (TEM)

3.4.1 Optical Microscope (OM)

Microstructure of the as cast and laser melted alloy samples were characterised by using an optical microscope (Axio lab A1,Carl Zeiss, Germany) with inbuilt image analyser software. The grain size measurements were done by using liner intercept method.

3.4.2 Scanning Electron Microscope (SEM)

The microstructures and local composition of the alloys were also analyzed using scanning electron microscope (SEM) equipped with Energy-dispersive X-ray Spectrometer (EDS) (JEOL JSM-6380 LA, USA). Field emission scanning electron microscope (Carl Zeiss Sigma FESEM, Germany) was also used especially for analysis of corrosion products.

3.4.3 Transmission Electron Microscope (TEM)

TEM examination was carried out using JEM-2100, JEOL model operating at 200 kV, equipped with an energy-dispersive spectrometer. For TEM analysis, samples were initially prepared in the form of a coupon (thin slice of 1 mm) using a slow speed precision cutting machine. Samples were then subjected to mechanical thinning from

base metal plate side till the thickness reached 100 μm. Further, 3 mm discs were punched and dimpled to a thickness of about 4 μm at the center. Samples were then thinned to electron transparency by ion milling technique using a GATAN (PIPS) ion milling machine. Milling was carried out using an accelerating voltage of 5 kV and 5° gun angle.

3.5 Phase analysis

The formation of different phases in the LSM regions was identified by glancing incident X-Ray diffractometry (GIXRD) (Rigaku smart lab, Japan) operating at a voltage of 40 kV and current of 30 mA. The data was collected using a monochromatic CuK_{α} radiation (λ= 0.154 nm) with a scan speed of 2° per minute, step size of 0.02° and over a range of 40 to 80°.

3.6 Integrated Coupled Plasma-Atomic Emission Spectroscopy (ICP-AES)

The composition of the cast alloys was determined using inductively coupled plasma atomic emissions spectroscopy (ICP-AES, IRIS INTREPID II XSP DUO, Thermo Electron).

3.7 Mechanical properties

The mechanical behaviour of the as cast alloys and laser melted alloys were analyzed. Following tests were carried out for evaluating the mechanical properties:

- Tensile Test
- Vicker's Microhardness

3.7.1 Tensile testing

The tensile strength of the alloys was determined using a 20 kN tensile test machine (PC-2000, Kudla instruments, India) (**Figure 3.4 (a)**) at room temperature. The test specimens of 30 mm gauge length and 6 mm diameter were machined according to the ASTM-E8/E8M standard as shown in the **Figure 3.4(a)** and **(b)** . At least three samples from each alloy were tested and average properties are reported. The fracture surfaces

of the tensile test samples were examined using SEM to understand the fracture behavior of the alloys.

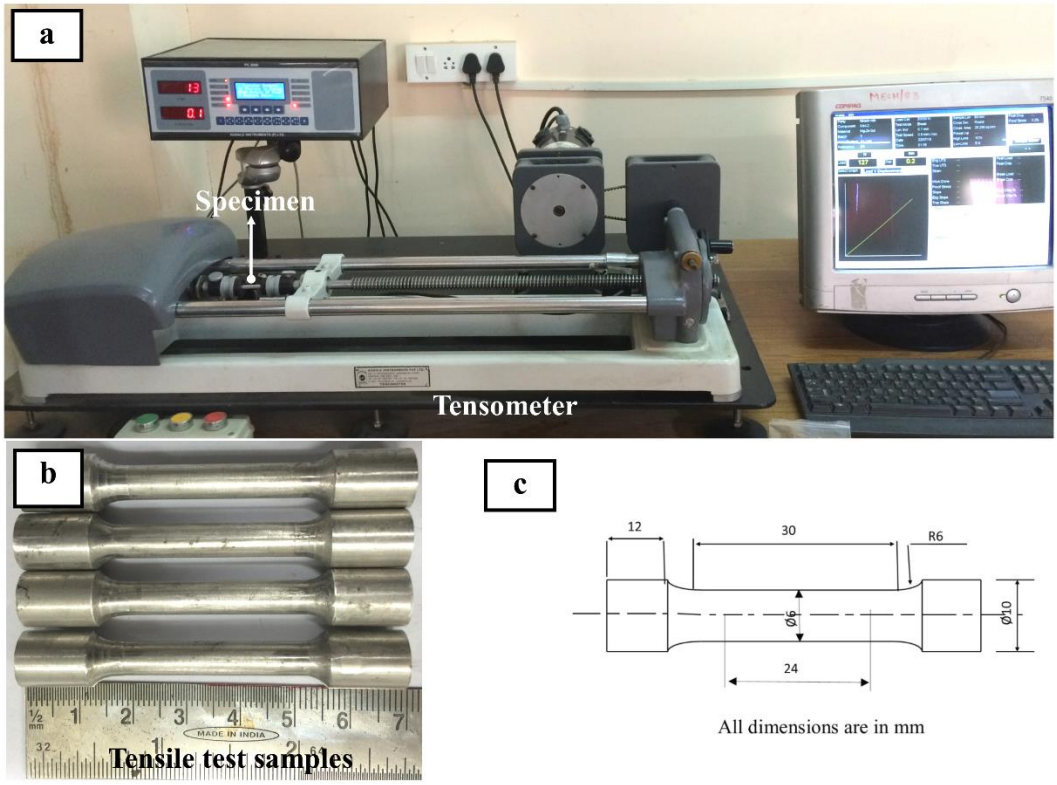

Figure 3.4 Tensile testing (a) Electronic tensometer (b) Tensile specimens (c) Schematic of specimen

3.7.2 Microhardness

The micro hardness measurements were carried out on polished surfaces of the alloys using Vickers micro hardness tester (HMV-G20 Shimadzu, Japan) **(Figure 3.5)**. The cross sectional region of the laser melted samples were used for the hardness investigation. A load of 25 g was applied with a dwell time of 15 seconds. Ten measurements were made on each sample and the average value of hardness along with standard deviation is here with reported.

Figure 3.5 Microhardness tester

3.8 Surface roughness measurement

Surface roughness was measured to understand the surface profile distribution of the samples after laser melting. Non-contact laser profiliometer (OLYMPUS-LEXT 3D laser measuring microscope, OLS4000, Japan) was used to measure the surface roughness of laser treated and untreated alloys in terms of S_q (root mean square height, µm) and S_a (arithmetic mean height, µm). A minimum of three positions on each laser melted surface with $1cm^2$ area were scanned.

3.9 Wettability behavior

Sessile drop technique was used to measure the surface wettability of the LSM samples. Krüss (DSA25E, Germany) contact angle goniometer was used to measure the surface wettability. The contact angle analyzer setup is shown in the **Figure 3.6.** In order to avoid the surface roughness effect, one set of samples surface is finely polished with velvet cloth with diamond paste after LSM. All samples are ultrasonically cleaned in alcohol before testing. All measurements were carried out by dropping 1 µL volume of polar liquid (DI water) and non-polar liquid (Diidomethane) for extracting the surface energy of the surface using contact angle measurement. Contact angle between the edge of the droplet of liquid and surface is measured with the camera attached with the goniometer microscope. The magnified image was further analyzed for contact angle value. A minimum of six independent reading were taken for each sample and results

are presented in terms of mean value with standard deviation. Fowkes equation was used to calculate the surface energy (Owens and Wendt 1969).

$$\frac{\gamma_L(1+\cos\theta)}{2} = \sqrt{\gamma_L^d \gamma_S^d} + \sqrt{\gamma_L^p \gamma_S^p} \qquad \textbf{3-2}$$

$$\gamma_s = \gamma_s^d + \gamma_s^p \qquad \textbf{3-3}$$

Where γ_s = Total surface energy, γ_L= Total surface tension, γ_S^d = Dispersive component of surface energy, γ_S^p= Polar component of surface energy

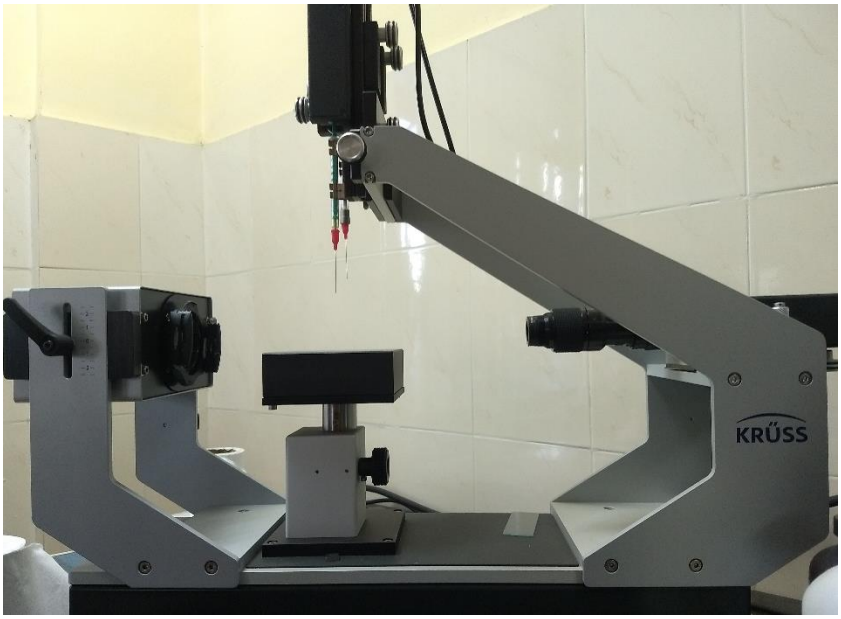

Figure 3.6 Contact angle analyzer (Goniometer)

3.10 *In-vitro* degradation

The *in vitro* corrosion rates of the developed alloys were determined using immersion and electrochemical methods (Atrens et al. 2015). Shi et al. (2010) reported that immersion studies can be used to understand the corrosion in Mg alloys in three different ways: (i) rate of weight loss, (ii) rate of hydrogen evolution and (iii) Mg^{2+} ion release. For immersion study, a standard inverted funnel and burette set up as proposed by Song et al. (2013) was used. The experimental setup is as shown in the **Figure 3.7**.

The exposed surfaces of the alloys were fine polished and cleaned by ultrasonicating in ethanol. The initial weight of the sample was recorded by using high-precision (0.0001 g) digital balance. The polished samples (**Figure 3.7(d)**) were encapsulated in resin with the polished surface (1 cm^2) exposed to the solution and kept in a static condition. A solution of 300 ml of Hanks balanced salt solution (HBSS) (HIMEDIA, Sigma-Aldrich) with initial pH of 7.4 was used as the electrolyte. The immersion tests were carried out for 180 h.

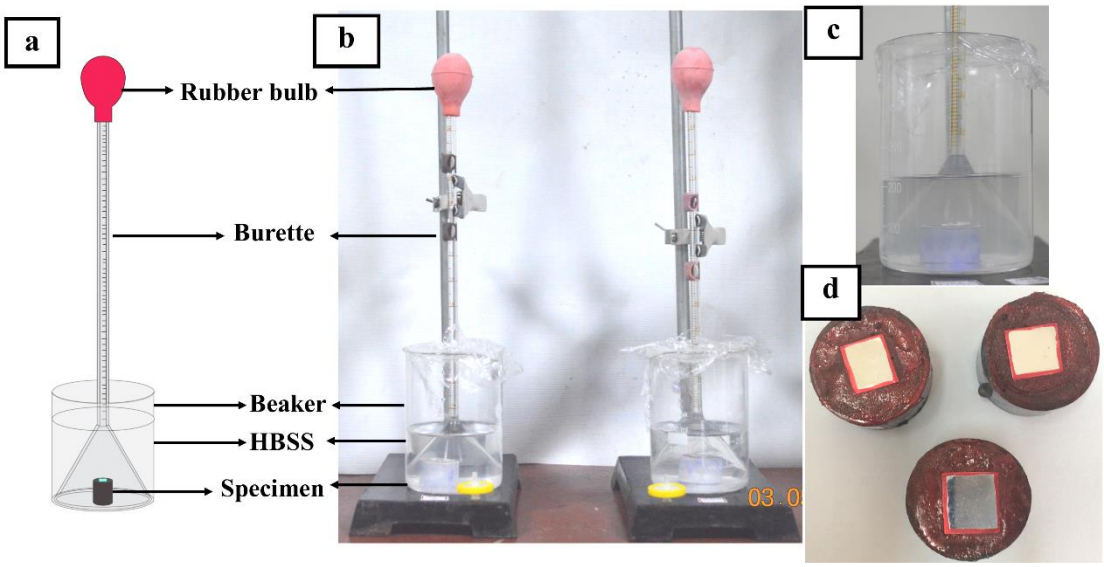

Figure 3.7 Immersion study (a) schematic diagram (b) experimental set up (c) enlarged view of beaker and (d) mounted samples.

The hydrogen evolution was suitably measured by reading the test solution level in the burette every 12 h by using standard inverted funnel and burette arrangement (**Figure 3.7 (a) (b)**) (Song et al. 2013). During the corrosion of the sample, each mole of Mg (24.306 gm) liberates one mole of hydrogen (22.4 L). Therefore, in long term immersion corrosion tests, the hydrogen emission during magnesium corrosion gives direct and real time corrosion rates at any instant of immersion. The average corrosion rate through the hydrogen evolution was estimated by following relation (Shi et al. 2010, (Zainal Abidin et al. 2013) and (Atrens et al. 2011).

$P_w = 3.65\Delta W / \boldsymbol{\rho}$ **3-4**

where, P_w is the average corrosion rate in mm/year, ΔW is the weight loss rate of the sample in $mg \cdot cm^{-2} \cdot day$ and ρ is the density of the alloy (1.768 $g \cdot cm^{-3}$).

The hydrogen emission rate V_H ($ml \cdot cm^{-2} \cdot day^{-1}$) is related to ΔW ($mg \cdot cm^{-2} \cdot day^{-1}$) using the following relation

$\Delta W = 1.085\ V_H$ **3-5**

Corrosion rate ($mm \cdot year^{-1}$) was calculated by substitution of ΔW obtained from **equation 3-5.** in **equation.3-4**.

During the immersion period, 10 ml of HBSS was collected every 12 h and the amount of Mg^{2+} ions released from the alloy were determined using atomic absorption spectroscopy (932 plus, GBC scientific equipment Ltd). The temperature and the pH of the solution are also recorded every 12 h using a digital thermometer with a resolution of 0.1 °C and a pH meter (µC - pH system 361, Systronics) with a resolution of 0.01 pH.

After the immersion test, the samples were removed from the solution and cleaned with a solution, containing 200 g/L chromic acid and 10 g/L silver nitrate, to remove the surface degradation products. The samples were first rinsed with distilled water followed by ethanol and finally dried in warm flowing air. The dried samples were weighed and the degradation rate was calculated using the following relation, according to ASTM-G31-72 (Atrens et al. 2013), (Cor 2004).

$$(CR)_w = \frac{\mathbf{K.W}}{\mathbf{D.A.T}} \quad \textbf{3-6}$$

Where $(CR)_w$ is the corrosion rate in $mm \cdot year^{-1}$ (mmpy), K is a constant (8.76×10^4 in millimeter per year), W is the difference between the initial and the final mass of the sample, A is the exposed area in cm^2, D is the density of the material in $g \cdot cm^{-3}$ and T is the immersion time in hours. The surface morphology of the immersed specimen was

examined using SEM and the composition of the degradation products were analyzed using EDS and XRD.

Metallographically polished samples were used for standard electrochemical corrosion studies at room temperature. Electrochemical measurements were performed using an electrochemical workstation (SP-150 EC Lab-Biologic, France). The construction has a three electrode test setup where a saturated calomel electrode (SCE) is used as the reference electrode, a platinum wire is used as the counter electrode, and the test sample is the working electrode. An area of 1 cm^2 of the test sample was exposed to freshly prepared HBSS. The open circuit potential (OCP) of the cell was obtained after allowing the cell to stabilize for 1 h. The polarization tests were conducted between 100 mV below the OCP and 100 mV above the OCP at a scan rate of 0.5 $mV \cdot s^{-1}$. The polarization experiments lasted for 15 minutes and it is repeated three times for each alloy. The corrosion current density (i_{corr}) of the alloy was determined from Tafel extrapolation, which was used to estimate the corrosion rate of the alloy as shown below:

$$(CR)_i = \frac{\mathbf{K1.i_{corr}.EW}}{\boldsymbol{\rho}} \qquad \textbf{3-7}$$

Where $(CR)_i$ is the corrosion rate in $mm \cdot year^{-1}$ (mmpy), i_{corr} is corrosion current density in $\mu A \cdot cm^{-2}$, EW is the equivalent weight of metal being tested and ρ is the density of the alloy in $g \cdot cm^{-3}$. The constant K1 = 3.27 x 10^{-3} $mm \cdot g \cdot (\mu A)^{-1} \cdot cm^{-1} \cdot yr^{-1}$.

3.11 Atomic Absorption Spectroscopy (AAS)

During the immersion 10 ml of HBSS was collected for every 24 hours and the amount of Mg^{2+} ions leeched from the alloy were determined using atomic absorption spectroscopy (AAS:932 Plus, GBC Scientific Equipment Limited, Australia).

3.12 Fourier Transform Infrared Spectroscopy (FTIR)

The functional group present in the corrosion product is identified using FTIR spectroscopy (Jasco FTIR-4200, Japan). The scratched out corrosion products from the

immersion samples were suitably mixed with potassium bromide and then pressed into round disk (transparent). The acquisition was carried out in the wave length of 4000-400 cm^{-1} in KBr pellet method.

3.13 *In-vitro* cell material interactions

A mouse embryo fibroblast cell line (NIH 3T3) was used to evaluate the cytotoxicity and cell-materials interactions of developed Mg alloys for culture durations of 1, 3 and 5 days. Calorimetric assay namely the MTT [3-(4, 5-dimethylthiazol (2-yl)-2, 5-diphenyl tetrazolium bromide] assay, was carried out to quantitatively understand the cell viability of these alloys. Before culture the samples were cleaned and sterilized at 121 °C for 20 min in an autoclave (15 psi). The sterilized samples were then placed in a 24-well plate and seeded with NIH 3T3 cells (1×10^4 cells/well). The cell culture media (DMEM, Dulbecco's modification of Eagle's Medium) was supplemented with 10 % v/v fetal bovine serum and the well plates were incubated at 37 °C and 5% CO_2 in an incubator. After each culture period, the MTT assay was performed following an established procedure (Das et al. 2014). SEM analysis was followed to determine how the cells adhere and proliferate on the different sample surfaces.

The following chapter contains results of the experimentations which were carried out by using the methods discussed in this chapter.

CHAPTER 4

4 RESULTS AND DISCUSSION

4.1 Studies on as cast alloys

Results of investigations carried out on the as cast alloys (Mg-1Zn-2Gd, Mg-1Zn-2Dy, Mg-3Zn-1.5Gd-1.5Nd) are discussed in the first section of this chapter.

4.1.1 Compositional analysis

The as-cast alloys were checked for elemental composition using ICP-AES and the results are presented in **Table 4.1.** It appears that there is a small wt. % loss in the alloying elements during casting.

Table 4.1 Chemical composition of the alloys in wt. %

Alloy	Zn	Gd	Dy	Nd	Zr	Mg
Mg-Zn-Gd	1	1.92	--------	--------	0.5	Bal.
Mg-Zn-Dy	1	-------	2.0	--------	0.4	Bal.
Mg-Zn-Gd-Nd	3.01	1.5	--------	1.6	1	Bal.

4.1.2 Microstructural analysis

The optical micrographs of the as-cast alloys are presented in **Figure 4.1.** These micrographs reveal α-Mg grains as the major phase (white in colour) with eutectic structures distributed along the grain boundaries (Black in colour). The addition of REE (Gd, Dy, and Nd) and Zr change the eutectic phase morphology to small sized particles and small network like structure is observed, which are distributed along the grain boundaries (Srinivasan et al. 2014b) (Zhang et al. 2013b). To identify the morphology and composition of the secondary phases at the grain boundary, the microstructures of these alloys were observed by using SEM and TEM. Micrographs of these alloys obtained using SEM are shown in **Figure 4.2**.

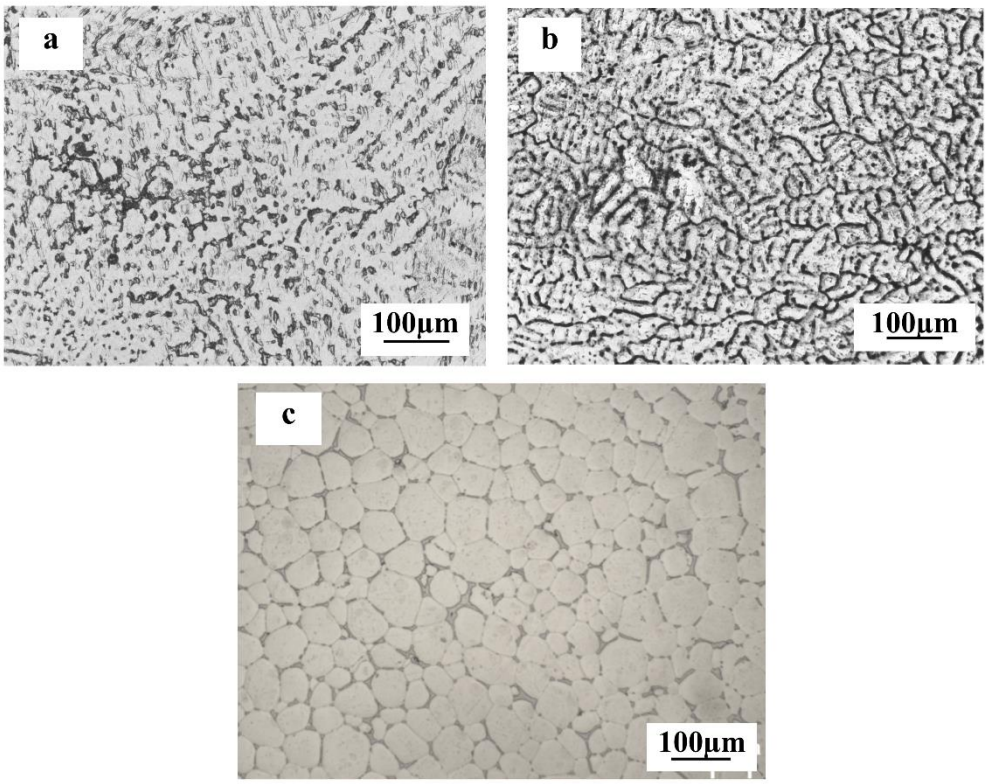

Figure 4.1 Optical micrograph of (a) Mg-Zn-Gd (b) Mg-Zn-Dy (c) Mg-Zn-Gd-Nd

The Mg-Zn-Gd alloy (**Figure 4.2(a))** consists of the α-Mg phase, the $MgZn_2$ intermetallic phase and a fine lamellar/acicular structure, known as LPSO (Zheng et al. 2011), that has grown towards the grain interior (Morishita et al. 2006). **Figure 4.3** and **Figure 4.4** shows the TEM images of Mg-Zn-Gd alloy with SAED patterns of $(Mg, Zn)_3Gd$ phase. The inset of **Figure 4.2 (a), Figure 4.4** show a magnified view of LPSO phase structure. In **Figure 4.3**, the phase with similar morphology was reported as $(Mg, Zn)_3$ Gd in Mg-Zn-Gd alloy (Yamasaki et al. 2007). This eutectic phase with a similar morphology has been reported as a LPSO phase which forms a quasi-continuous honeycomb like network phase at the matrix grain boundaries of Mg-Zn-Y or lamellar phase in Mg-Zn-Gd alloys (Li et al. 2017; Xu et al. 2016). However in this work, there is no peak that is related to Gd rich LPSO phase in XRD spectra is identified, presumably due to its low concentration. The summary of the EDS analysis of these different phases of these alloys are presented in **Table 4.2**. The primary phase, marked as A in **Figure 4.2 (a)**, is rich in Mg (95.6 wt. %) with a small amount of dissolved Gd (4.33 wt %). The grain boundary secondary phase, marked B (LPSO

phase), reveals a high concentration of Gd up to 19.9 wt. % with a small amount of Zn (5.4 wt. %). A Similar composition range has been reported by Zhang et al. 2013 for the LPSO phase in this alloy.

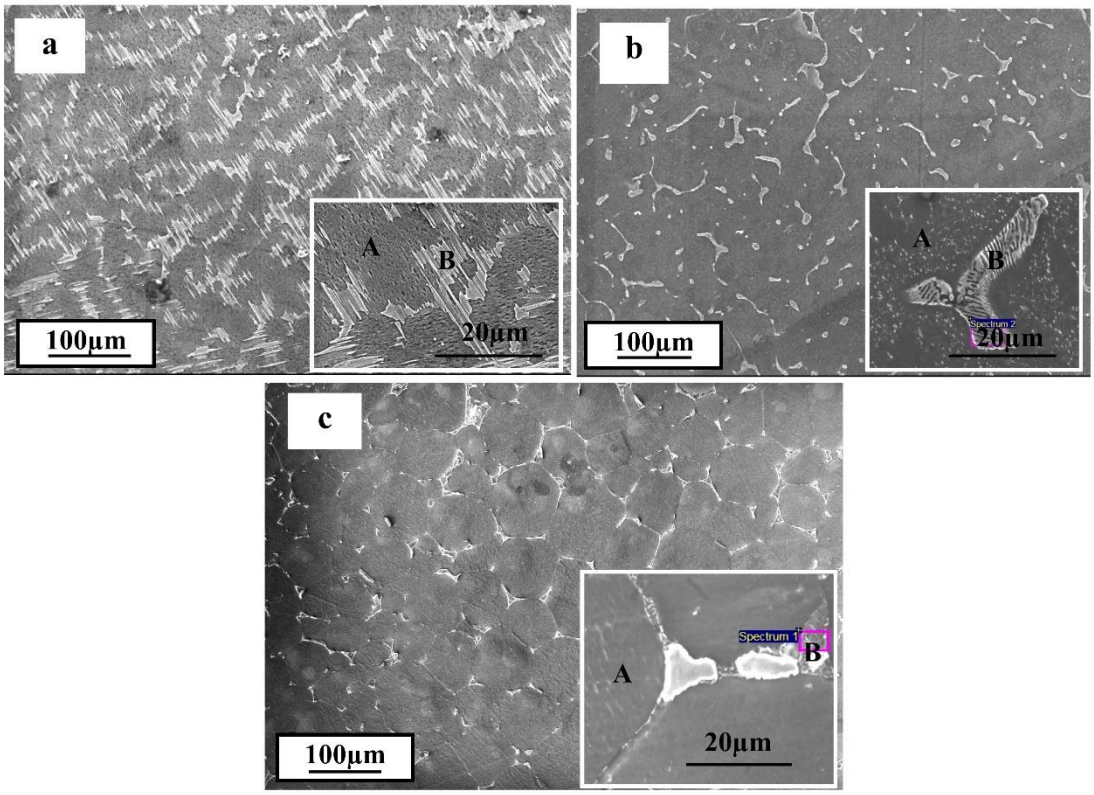

Figure 4.2 SEM microstructure of alloys showing morphology of different phases (a) Mg-Zn-Gd (b) Mg-Zn-Dy (c) Mg-Zn-Gd-Nd

Table 4.2 EDS compositional analysis (wt. %) of different phases observed in the Mg-Zn-REE alloys (**Figure 4.2**)

Alloys	Regime	Mg	Zn	Gd	Dy	Nd	Zr
Mg-Zn-Gd	A	95.6	------	4.3	------	------	0.02
	B	74.4	5.4	19.9	------	------	0.23
Mg-Zn-Dy	A	93.5	2.1	------	4.13	------	0.21
	B	38.4	29.0	------	32.2	------	0.26
Mg-Zn-Gd-Nd	A	95.4	3.9	0	------	0.38	0.32
	B	71.7	8.4	3.3	------	16.0	0.5

The Mg-Zn-Dy alloy exhibits a two phase microstructure and is represented in **Figure 4.2 (b)**, **Figure 4.5 and Figure 4.6. Figure 4.2(b)** consists of α-Mg grains with a majority of isolated or island like compounds along the grain triple points. These island like structures contain Mg-Zn intermetallic compound and a eutectic phase. This intermetallic phase has been reported as Mg_8ZnDy (Zhang et al. 2014a). and these hollow out Skelton structures are attached to long period stacking ordered structure (LPSO) (Zhang et al. 2014b). **Figure 4.6** (TEM) shows the presence of LPSO phase with lamellar morphology (Zhang et al. 2013a) in Mg-Zn-Dy system. The measured spacing between the successive fringes is 0.97 nm. There is no massive formation of LPSO phase because of the lower amount of alloying element (Dy) added. **Figure 4.5,**

reveals the presence of some block shaped morphology reported as eutectic phase associated with LPSO formed in the α-Mg matrix grain boundaries, showing a discontinuous network morphology. The analysis of the secondary eutectic phase at higher magnification in SEM (inset of **Figure 4.2 (b)**), reveals a lamellar structure that forms a semi-continuous network structure within α-Mg. The XRD analysis (**Figure 4.9(b)**) confirms that the major intermetallic phase in Mg-Zn-Dy alloy is Mg_7Zn_3 as reported in (Peng et al. 2009). The compositional analysis (**Table 4.2**) shows that the eutectic compound (**labeled B** in **Figure 4.2 (b))** is rich in Dy (32.2 wt. %) and Zn (29 wt. %) compared to their concentration in the Mg matrix which revealed 93.5 (wt. %) Mg, 4.1 (wt. %) Dy and 2.1(wt. %) Zn. The compositional analysis also indicates a good amount of dissolved alloying elements in the Mg matrix, which can potentially improve mechanical properties of the alloy via solid solution strengthening.

The SEM microstructure of Mg-Zn-Gd-Nd alloy is shown in **Figure 4.2(c)**, which is analogous to the microstructure of Mg-Zn-Dy alloy. However, the Mg-Zn-Gd-Nd alloy exhibits secondary eutectic phase along the grain boundary and grain triple points. The averaged grain size of the observed grains are in the range of 60-130 µm which indicate the lower cooling rate during casting. The secondary phase has been identified as $Mg_{12}Nd$, through XRD (Ding et al. 2010). The specific distribution of phases are observed in the grain triple points also reported as T-phase (Mg_7ZnRE) appearing as white network (Neil et al. 2009). TEM analysis is carried out to observe the detailed distribution of phases. **Figure 4.7** and **Figure 4.8** shows the bright field TEM images with selected area SAED pattern. Granular (**Figure 4.7**) and rod shaped (**Figure 4.8**) precipitates occurs in the matrix and grain boundaries. The precipitates occur in the range of 20-500 nm. The identified granular phases are mainly Mg_7Zn_3 and this kind of similar morphology was reported in Gui et al. (2018). It is observed from the EDS analysis (**Table 4.2**) that these phases (**labeled B** in **Figure 4.2 (c))** are enriched with up to 16 wt. % Nd with a small amount of Gd (3.3 wt. %). The primary phase of α-Mg constituted 95.4 wt. % of Mg. Overall, the formation of secondary phases along the grain boundaries in the present alloys indicates that they are formed in the later stages of solidification due to the rejection of alloying elements from the solidifying matrix as a result of their decreased solubility with decrease in temperature.

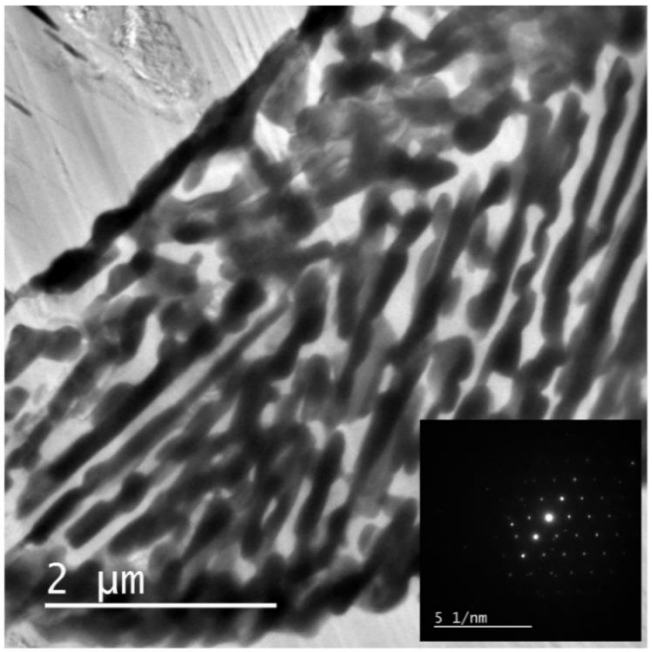

Figure 4.3 TEM of Mg-Zn-Gd alloy with SAED patterns of $(Mg, Zn)_3Gd$ phase

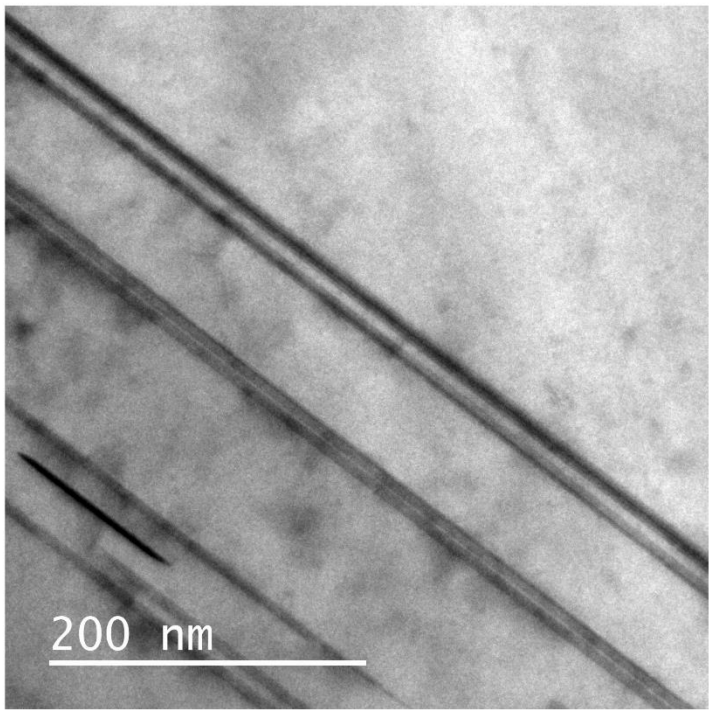

Figure 4.4 TEM of Mg-Zn-Gd alloy with LPSO phase

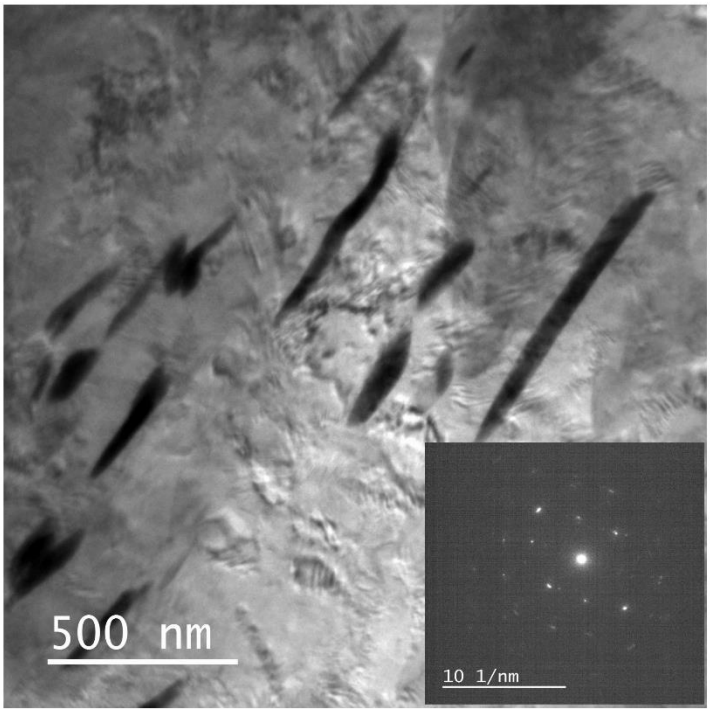

Figure 4.5 TEM analysis of Mg-Zn-Dy eutectic phase with SAED pattern

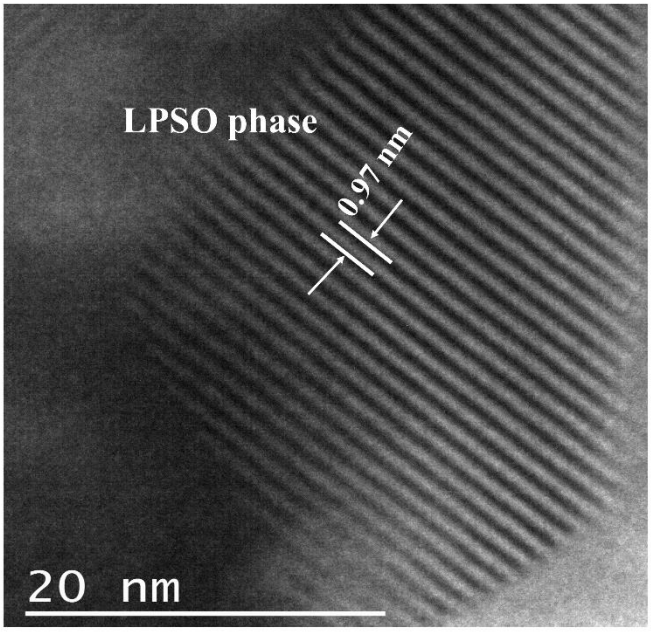

Figure 4.6 TEM analysis of Mg-Zn-Dy LPSO phase

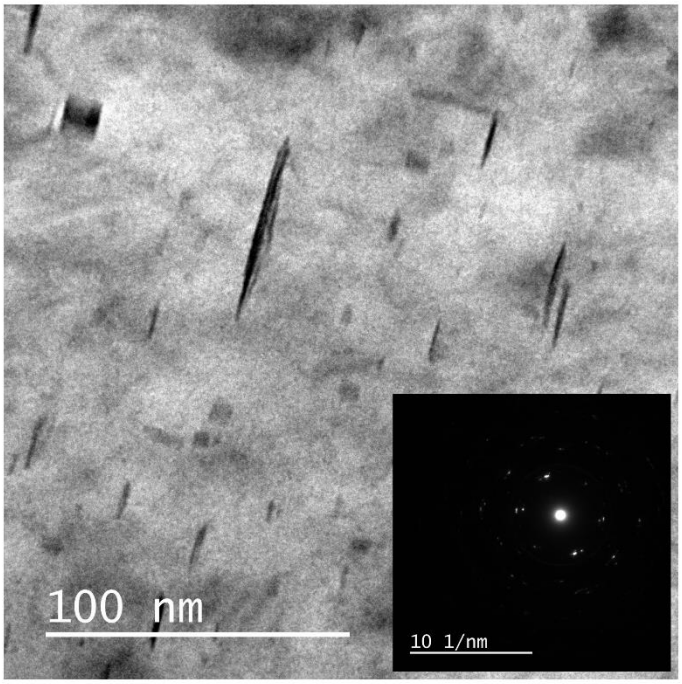

Figure 4.7 TEM analysis of Mg-Zn-Gd-Nd with granular phases

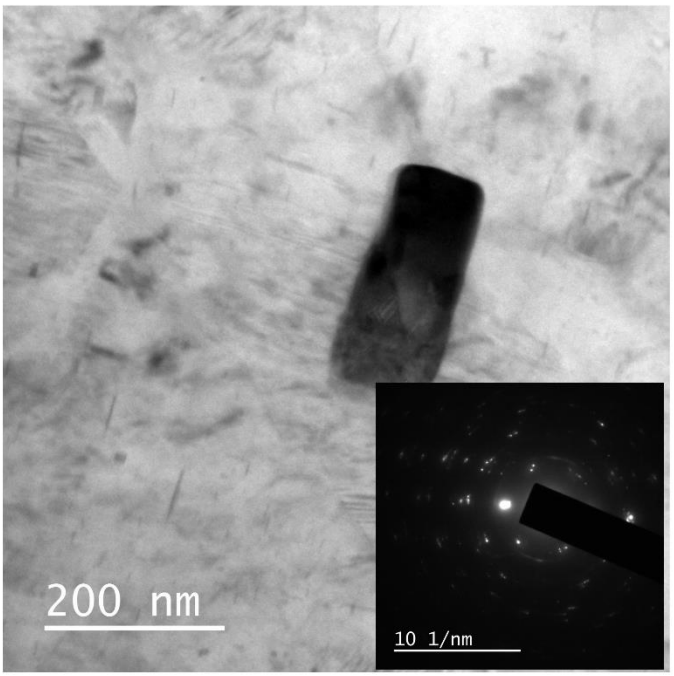

Figure 4.8 TEM analysis of Mg-Zn-Gd-Nd with rod phase

4.1.3 Phase analysis

Figure 4.9 shows the XRD patterns of as-cast alloys and all three alloys exhibit α-Mg as major phase. However, depending on the type of REE addition, the alloys showed peaks corresponding to different secondary phases such as Mg-Zn, MgZnDy and MgNd. The Mg-Zn-Gd alloy (**Figure 4.9 (a)**) shows two distinct peaks corresponding to $MgZn_2$ (Gao and Nie 2007) and $GdZn_2$. The alloy with Dy (**Figure 4.9 (b)**) shows Mg_7Zn_3, $DyZn_5$ and Mg_8ZnDy phases. The XRD and EDS composition analysis of these phases matches with earlier reports (Zhang et al. 2014a). The Mg-Zn-Gd-Nd (**Figure 4.9(c)**) spectra reveal the presence of $Mg_{12}Nd$ and MgZn phases (Zhang et al. 2012f).

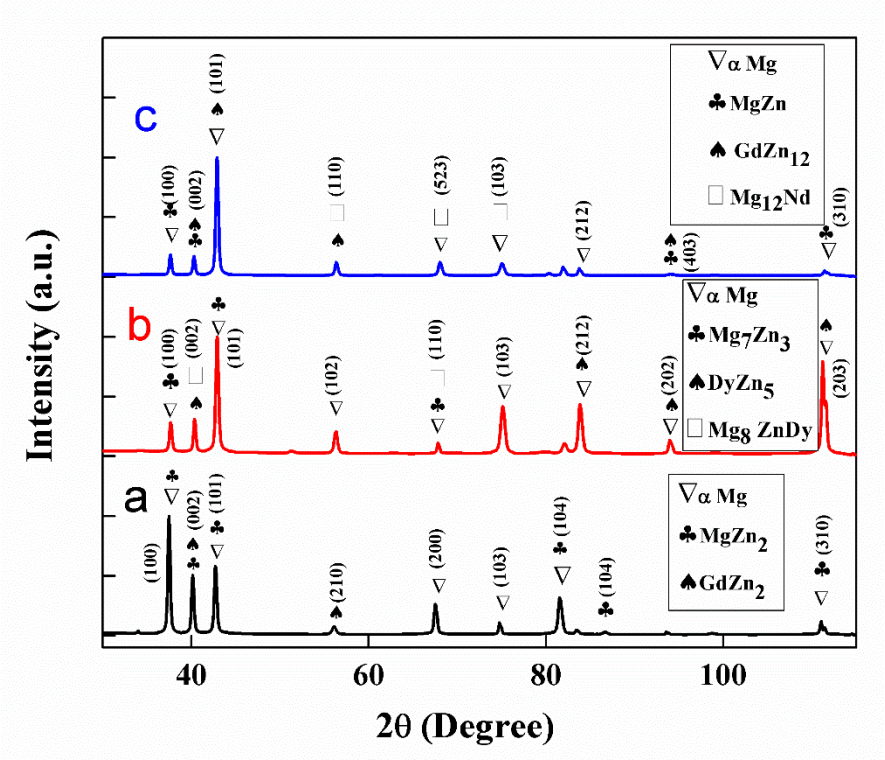

Figure 4.9 X-ray diffraction analysis of different phases in (a) Mg-Zn-Gd, (b) Mg-Zn-Dy and, (c) Mg-Zn-Gd-Nd alloys

4.1.4 *In-vitro* degradation-Immersion studies

It is well known that Mg alloys interact with HBSS and produce magnesium hydroxide, Mg^{2+} ion and hydrogen gas as per the following reactions (Yang and Zhang 2009)

$Mg \rightarrow Mg^{2+} + 2e^-$ (anodic reaction) **4-1**

$2H_2O + 2e^- \rightarrow H_2 + 2(OH)^-$ (cathodic reaction) **4-2**

$Mg^{2+} + 2(OH)^- \rightarrow Mg(OH)_2$ (total reaction) **4-3**

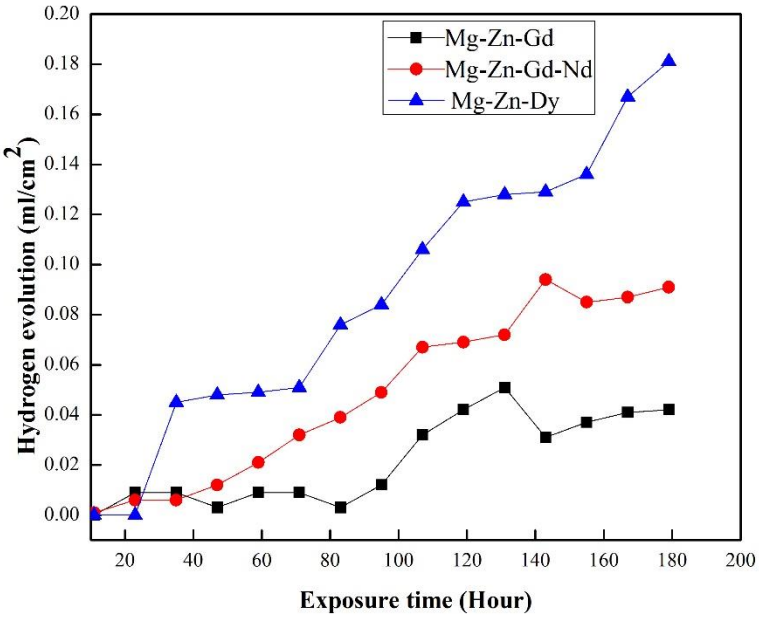

Figure 4.10 The rate of hydrogen evolution through immersion corrosion of the three developed alloys as a function of immersion time in HBSS

The measurement of hydrogen and Mg^{2+} ions release thus provides a good understanding of the overall degradation kinetics of these alloys (Zhao et al. 2008). The volume of hydrogen produced by the present Mg alloys during immersion in HBBS is presented in **Figure 4.10**. During the initial period of immersion up to 24 h the rate of hydrogen evolution appears to be small in all three alloys. The hydrogen production rates were observed to be 0.84 ml·cm^{-2}, 0.37 ml·cm^{-2} and 0.29 ml·cm^{-2} for Mg-Zn-Dy, Mg-Zn-Gd-Nd and Mg-Zn-Gd, respectively. As the immersion period increases, the corrosion rate also increases gradually. After about 35 h the Mg-Zn-Dy alloy degraded rapidly as evidenced by its high rate of hydrogen evolution (0.84 ml·cm^{-2}) which is higher than the other two alloys, Mg-Zn-Gd-Nd (0.37 ml·cm^{-2}) and Mg-Zn-Gd (0.29 ml·cm^{-2}). Moreover, the volume of hydrogen evolved by Mg-Zn-Gd and Mg-Zn-Gd-Nd alloys was significantly lower than that of Mg-Zn-Dy alloy at all time periods of

immersion tests suggesting a relatively poor in vitro corrosion resistance for Mg-Zn-Dy alloy. Further, the rate of increase in the hydrogen evolution rate (slope of hydrogen production vs. time) in **Figure 4.10** of Mg-Zn-Dy was also higher than for the other two alloys indicating its high corrosion rate possibly due to an unstable passive film on its surfaces. The final corrosion rates calculated by the hydrogen evolution are presented in the **Table 4.3**. Among all alloys, Mg-Zn-Gd alloy exhibits the lowest hydrogen evolution, indicating a superior corrosion resistance. Interestingly, the hydrogen evolution of this alloy was very stable up to ~ 85 h of immersion, followed by gradual increase with immersion time.

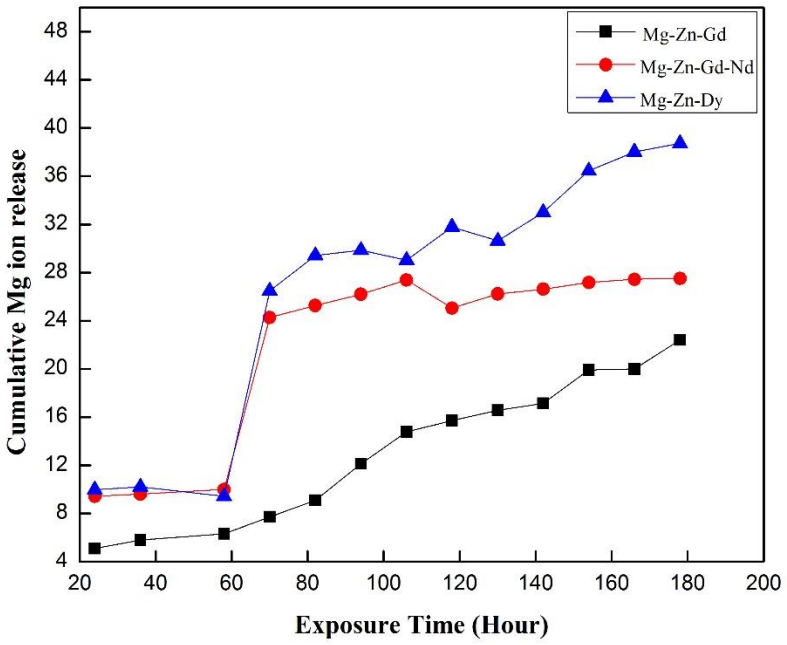

Figure 4.11 Amount of Mg^{2+} released through immersion corrosion of the three developed alloys as a function of immersion time in HBSS

The amount of Mg^{2+} ions released from the different alloys, after 180 h of immersion in HBSS, is shown in **Figure 4.11**. As expected and in line with the hydrogen evolution, the amount of Mg^{2+} ions released from these alloys also increases with the immersion time. Among all alloys studied, the Mg-Zn-Gd alloy shows a gradual increase in the Mg^{2+} ions release while the other two alloys reveal a sharp increase in the release at about 70 h of immersion. The maximum concentration of Mg^{2+} in the HBSS for Mg-

Zn-Gd alloy was determined to be 13.3 ppm which is almost 71 % lower than that of Mg-Zn-Gd-Nd (22.8 ppm) alloy and 103 % lower than that of Mg-Zn-Dy (27.1 ppm) alloy. The abrupt increase in the Mg^{2+} ion release, between 60 and 70 h, of Mg-Zn-Dy and Mg-Zn-Gd-Nd alloys is not clearly understood yet but it is presumed that the local disturbance in the surface passive film of these alloys could be one of the reasons. Another potential reason could be the size, shape and composition of the secondary phases formed in these alloys. The corrosion rate calculated by Mg^{2+} ion release was also found out and represented in **Table 4.3**. Maximum corrosion rate was observed for Mg-Zn-Dy and lower corrosion rate was observed for Mg-Zn-Gd alloy. The secondary phases distributed along the grain boundaries in Mg-Zn-Dy and Mg-Zn-Gd-Nd can form a galvanic couple with the Mg matrix and that would accelerate the corrosion of the α-Mg matrix (Srinivasan et al. 2014b). The galvanic corrosion mainly happened by the potential difference between the α-Mg phase and secondary phase which is formed in the Mg matrix. Song and Atrens (2003) studied AZ31 alloy and reported that secondary phase ($Mg_{17}Al_{12}$) formed in the alloy could either act as a corrosion behavior or galvanic cathode accelerating the corrosion. The role of corrosion process is mainly influenced by the volume fraction and distribution of the secondary phase. The continuous and fine distributed phase helps to act as a corrosion barrier and discontinuous coarse phase accelerates the corrosion (Bi et al. 2014). In the present study Mg-Zn-Gd alloy, the isolated LPSO (**Figure 4.2(a) Figure 4.4**) and $(Mg,Zn)_3$ Gd phases (**Figure 4.3**) present at the grain boundaries are more continuous and uniformly distributed (Zhang et al. 2012a), and these secondary phases act as a corrosion barrier. The better fraction of anode to cathode ratio should reduce the galvanic effect severity and lead to better corrosion resistance (Srinivasan et al. 2014b). Therefore, the large size and grain boundary precipitation of secondary phases in Mg-Zn-Dy and Mg-Zn-Gd-Nd could be responsible for their higher corrosion rate. Besides, Mg-Zn-Gd has decreased corrosion resistance as more coarse secondary phases are present at the grain boundaries (**Figure 4.2 (a)**). The secondary phase morphologies observed in this Mg-Zn-Gd also different from other two alloy systems. The presence of $(Mg,Zn)_3Gd$ phase with less volume at inderdendritic and grain boundaries will hinder the corrosion (Srinivasan et al. 2014b). In addition, the presence of LPSO also influences the corrosion process. The sharp increase in the Mg^{2+} ions release of other two alloys made

it difficult to compare the corrosion resistance of the three alloys. For example, after 70 h of immersion the rate of ion release (slope of ion release vs. time curves) appears to be low for Mg-Zn-Gd-Nd alloy compared to other two alloys. The estimated rate of Mg ion release, after 70 h of immersion, from Mg-Zn-Dy, Mg-Zn-Gd-Nd and Mg-Zn-Gd alloys were found to be 0.11 ppm·h^{-1}, 0.04 ppm·h^{-1} and 0.12 ppm·h^{-1}, respectively. This data indicate that by 130 h of immersion in HBSS the Mg-Zn-Gd alloy can release more Mg^{2+} ions than Mg-Zn-Gd-Nd alloy, suggesting a relatively poor long-term corrosion resistance relative to the Mg-Zn-Gd-Nd alloy.

Table 4.3: Corrosion rate of Mg-Zn-REE alloys derived from immersion corrosion measurements

	Corrosion rate (mm/year) comparison by immersion studies		
Material	Weight loss method	Hydrogen emission method	Mg 2+ ion release method
Mg-Zn-Gd	0.99±0.45	0.056±0.03	0.86
Mg-Zn-Gd-Nd	1.32±0.55	1.13±0.82	1.27
Mg-Zn-Dy	2.13±0.35	1.92±0.99	0.91

The corrosion rates by weight loss measurements as well as hydrogen emission are presented in **Table 4.3**. The lowest corrosion rate of 0.99 ± 0.45 mmpy is observed with the Mg-Zn-Gd alloy and the highest corrosion rate is exhibited by Mg-Zn-Dy alloy (2.13 ± 0.35 mmpy) by weight loss method. The Mg-Zn-Gd-Nd alloy presents medium corrosion rates. Cai et al. (2012), reported that the average corrosion rate of as-cast Mg-1%Zn was ~ 2 mmpy which is almost twice the corrosion rate of the present Mg-Zn-Gd alloy and significantly higher than that of Mg-Zn-Gd-Nd alloy. Same corrosion rate trend can be observed through hydrogen emission measurement also. Overall, the

corrosion rates estimated using the weight loss method corroborate the hydrogen evolution and Mg^{2+} ions release trends observed with these three alloys.

The severity of the corrosion damage and the corrosion products formed on the Mg-Zn-REE alloy surfaces after immersion tests were examined by SEM and XRD. The surface morphology of the alloy and XRD analysis of surface product after the 180 hours of immersion in HBSS is shown in **Figure 4.12** and **Figure 4.13.** The degraded surfaces of Mg-Zn-Gd and Mg-Zn-Gd-Nd reveal features that are different from those formed on Mg-Zn-Dy alloys. The Mg-Zn-Gd (**Figure 4.13(a))** and Mg-Zn-Gd-Nd (**Figure 4.13(c))** alloys present a compact continuous film covering the entire sample surface with bright precipitates. The formation of a continuous compact film on the surface of these alloys provides a protection against further degradation of the surface in HBSS. These two alloys exhibit in effect relatively better corrosion resistance than the Mg-Zn-Dy alloy. On the other hand, the surface morphology of the Mg-Zn-Dy **Figure 4.13(b)** alloy lacks the presence of a continuous surface film and present a large number of discrete precipitates, which relate to the release of loosely bound $Mg(OH)_2$. The volume changes associated with the formation of porous $Mg(OH)_2$ would have destabilized the surface film, leading to a poor corrosion resistance.

The EDS analysis was carried out at different regions for all the immersed samples. The white particles on the surface **Figure 4.13(a)** of Mg-Zn-Gd (labelled as (A)) **Figure 4.13(b)** of Mg-Zn-Dy (labelled as (A)) and Mg-Zn-Gd-Nd **Figure 4.13(c)** (labelled as (B)) consisted of O, Ca, P and Mg. The compact film formed on the alloy surface **Figure 4.13(a)** (labelled as (B)) in Mg-Zn-Gd and in **Figure 4.13(c)** (labelled as (A)) in Mg-Zn-Gd-Nd) appears to prevent further degradation of these two alloys. This film contains $Mg(OH)_2$ with small amounts of Ca and P. The Mg to O and Ca to P ratio of the corrosion products on Mg alloys can be used to assess the formation of $Mg(OH)_2$ and calcium phosphate on the surface of the alloy (Zander and Zumdick 2015). These products have mainly formed because of the interaction between Mg ions with the carbonate, phosphate and calcium ions which are contained in the HBSS (Atrens et al. 2011). The EDS data, indicate that the Mg to O ratio is 0.74, 0.68 and 0.11 for Mg-Zn-Gd, Mg-Zn-Gd-Nd and Mg-Zn-Dy alloy, respectively, which indicates

the formation of $Mg(OH)_2$ on the first two alloys as the ratio is more than 0.5 (Zander and Zumdick 2015). Corresponding $Mg(OH)_2$ peaks are observed in the XRD spectra analysis (Yang and Zhang 2009) **Figure 4.12** at 2θ of 18°, 32°, 38° and 62° mainly (Reference code 00-044-1482). The Ca to P ratio for Mg-Zn-Gd, Mg-Zn-Dy and Mg-Zn-Gd-Nd alloys is 1.7, 1.6 and 0.67 respectively. The standard ratio of Ca to P in hydroxyapatite is 1.67 (Nge et al. 2010), which confirm that the white particles at the surface of Mg-Zn-Gd and Mg-Zn-Dy alloy have shown the close presence of hydroxy apatite. The XRD spectra also show the presence of hydroxy apatite (HAp) (Reference code 01-076-0694), and calcium phosphate (00-009-0348). The formation of Ca and P compounds during immersion in HBSS on the present Mg alloys may assist them in bone bonding.

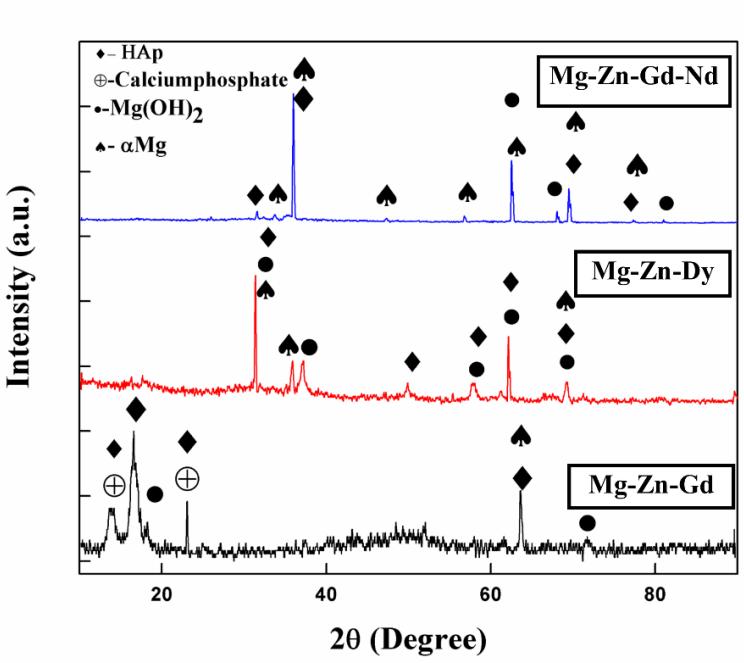

Figure 4.12 XRD analysis of alloy samples after 180 h of immersion

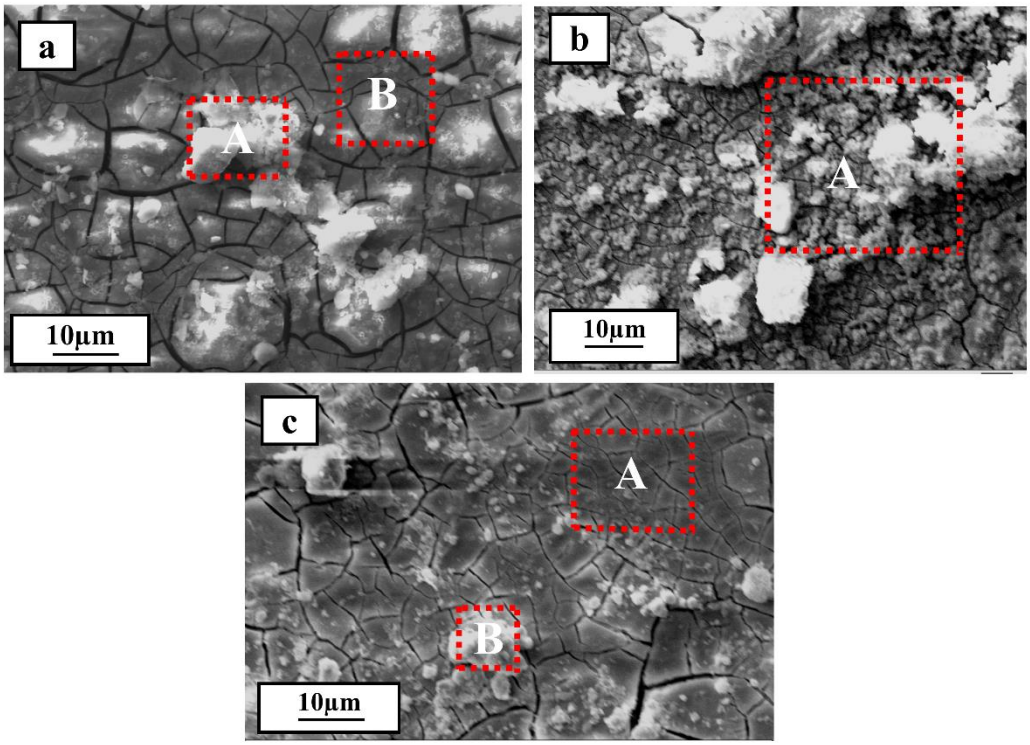

Figure 4.13 : SEM surface morphology of (a) Mg-Zn-Gd (b) Mg-Zn-Dy (c) Mg-Zn-Gd-Nd alloys samples after 180 h of immersion

4.1.5 Electrochemical behaviour

Figure 4.14 shows the Tafel plots of Mg alloys tested in HBSS at room temperature. The measured electrochemical parameters, corrosion potential (E_{corr}) and corrosion current (i_{corr}) from Tafel extrapolation, and the corrosion rate estimated using **equation 3-7** and are presented in **Table 4.4.**

.

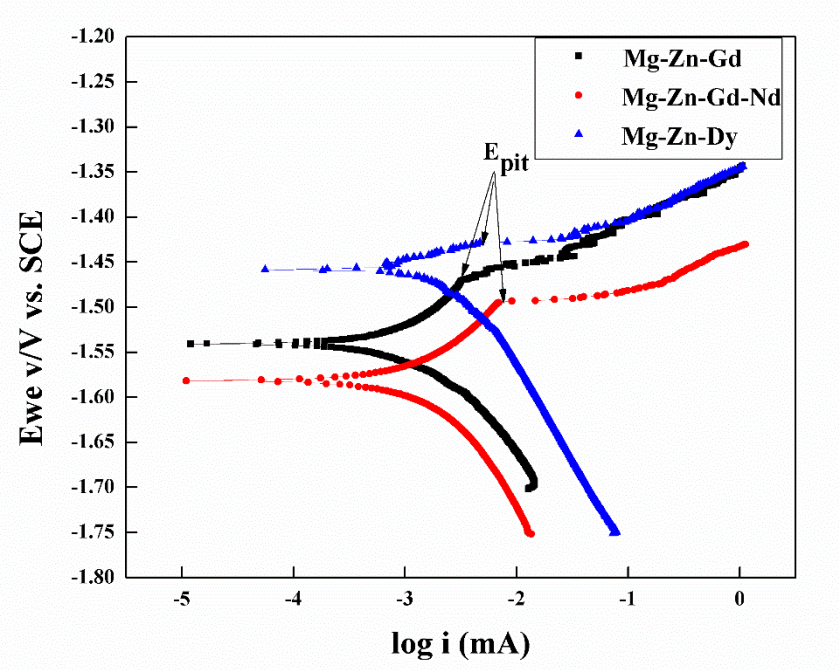

Figure 4.14 Tafel plot extrapolation of the Mg-Zn-REE alloys tested in HBSS

Table 4.4 Electrochemical properties derived from Tafel extrapolation

	Tafel extrapolation		
Material	E_{corr} (V *vs.* SCE)	i_{corr} (µA/cm ^{2})	Corrosion rate (mm/year)
Mg-Zn-Gd	-1.53	13.6±4	0.04±0.15
Mg-Zn-Gd-Nd	-1.58	25.1±9	0.07±0.02
Mg-Zn-Dy	-1.45	42.2±8	0.12±0.38

The results showed that i_{corr} was 13.6 µA·cm^{-2} for Mg-Zn-Gd alloy, 25.1 µA·cm^{-2} for Mg-Zn-Gd-Nd alloy and it was 42.2 µA·cm^{-2} for Mg-Zn-Dy alloy. These i_{corr} values indicate that the corrosion rate of the alloys would be in the order of Mg-Zn-Gd < Mg-Zn-Gd-Nd < Mg-Zn-Dy. However, the corrosion potential, E_{corr}, of these alloys showed slightly different trend. The lowest E_{corr} of -1.58 V vs. SCE was exhibited by Mg-Zn-Gd-Nd alloy and the highest potential was observed with Mg-Zn-Dy (-1.45 V vs. SCE). The E_{corr} of Mg-Zn-Gd alloy was measured to be -1.53 V vs. SCE. These corrosion potentials suggest that the initiation of corrosion would be difficult in Mg-Zn-Dy alloys compared to the other two alloys studied in this work. The easy initiation of corrosion

on Mg-Zn-Gd-Nd and Mg-Zn-Gd alloys can be clearly seen from the relatively high amount of hydrogen emission during the initial 24 h of immersion in HBSS, **(Figure 4.10)** The absence of hydrogen emission from the Mg-Zn-Dy alloy during the first 24 h of immersion clearly supports the observed high E_{corr} of the alloy during electrochemical testing. Once initiated the corrosion front appears to propagate rapidly in this alloy, as evidenced by a high i_{corr} and hydrogen emission. The corrosion rates of Mg-Zn-Gd, Mg-Zn-Gd-Nd and Mg-Zn-Dy alloys estimated using **equation 3-7** are 0.04 mmpy, 0.07 mmpy and 0.12 mmpy, respectively. The current density increases sharply as a function of applied potential, above OCP. A sudden change in potential occurs in the anodic branches of all three alloys, which is indicated as E_{pit} (**Figure 4.14**) The absolute value (E_{pit}-E_{corr}) of passive range of the Mg-Zn-Dy alloy is 0.02 V vs. SCE, which is very much less than for the Mg-Zn-Gd (0.08 V vs. SCE) and Mg-Zn-Gd-Nd (0.1 V vs. SCE) alloys. The higher value indicates that the passivation film formed over Mg-Zn-Gd and Mg-Zn-Gd-Nd is stable for longer time and hence forth any further corrosion is inhibited.

The trend of the corrosion rates determined from the electrochemical tests thus agrees well with the corrosion rates obtained from weight loss measurements. However, the corrosion rates of the alloys estimated following weight loss method were always higher than those obtained from electrochemical tests mainly because (Shi et al. 2010), (Song and Atrens 2003): measurement of the corrosion rate by the Tafel plot is fundamentally a technique repeating an instantaneous corrosion state. However, in the case of magnesium alloys, corrosion is not constant with the time in solution. Typically, corrosion initially starts at localized regions and after a time of immersion it slowly expands over the whole surface. In this respect weight loss measurement averages the corrosion rate over the time of immersion. This mainly shows that Tafel extrapolation tests require stringent evaluation of corrosion rate when being compared with immersion studies. After a certain period of incubation, corrosion typically starts as localized and slowly expands over the surface of the sample. This spreading of corrosion may not happen in the short span of test. Thus, evaluation of corrosion rate by short term test (Tafel extrapolation) may not agree with the corrosion rate measurement by long term test (Shi et al. 2010). So considering the above reasons,

degradation studies of laser melted alloys in the upcoming sections were carried out by adopting the immersion corrosion technique.

4.1.6 *In vitro* cell-materials interactions

The influence of REE addition on the *in vitro* cytotoxicity of Mg-Zn-REE alloys was assessed using the MTT assay. Results are presented in **Figure 4.15**. They demonstrate that all three alloys are biocompatible and did not induce any toxic effect after 1, 3 and 5 days of culture. Among the three alloy systems, Mg-Zn-Gd showed the highest cell proliferation after 1 and 3 days of culture. After the third days of culture, the cell viability on the alloys decreased slightly except for the Mg-Zn-Dy alloy. In general, the magnitude of cell viability on the three alloys are in the order of 80% (Mg-Zn-Gd-Nd), 80% (Mg-Zn-Gd) and 160 % (Mg-Zn-Dy) at day 5. The results also indicate that the viability of cells for the three alloys are greater than 70%, which is considered as good with respect to biocompatibility. **Figure 4.16 (a), (b), (c)** show the morphology of cells cultured on the different alloys. The cells were all well spread and flattened across the alloy surface. Also cells were seen to be connected to neighboring cells and to the substrate. **Figure 4.16(a),** present a uniform cell distribution over the Mg-Zn-Gd alloy (arrow) after the first day of cell culture. After that, the first day of cell culture the Mg-Zn-Gd-Nd (**Figure 4.16(c**)) surface shows a dome shaped cell formation. The cells which are grown on Mg-Zn-Dy (**Figure 4.16(b), Figure 4.15)** consist of few slender like structures which are attached to other cells and are forming a network. The different cell shapes formed on the surface may relate to different Zn, Gd, Dy and Nd additions and their varying concentration in the cell environment. In the Mg-Zn-Dy **(Figure 4.16(b))** alloy apart from the confluent cell layer, there is a white granular apatite spread nearer to the cell area. It shows that the distributed cells were even growing into the pores and are trying to establish a uniform cell network.

The results indicate that the prepared Mg-REE based alloys present a good biocopmaptabilty with cell culture. The cells tend to adhere on to the surface of the alloys. Hence, addition of REE elements improves corrosion resistance and cytocompatibility. This illustrates that these alloys are promising for clinical studies.

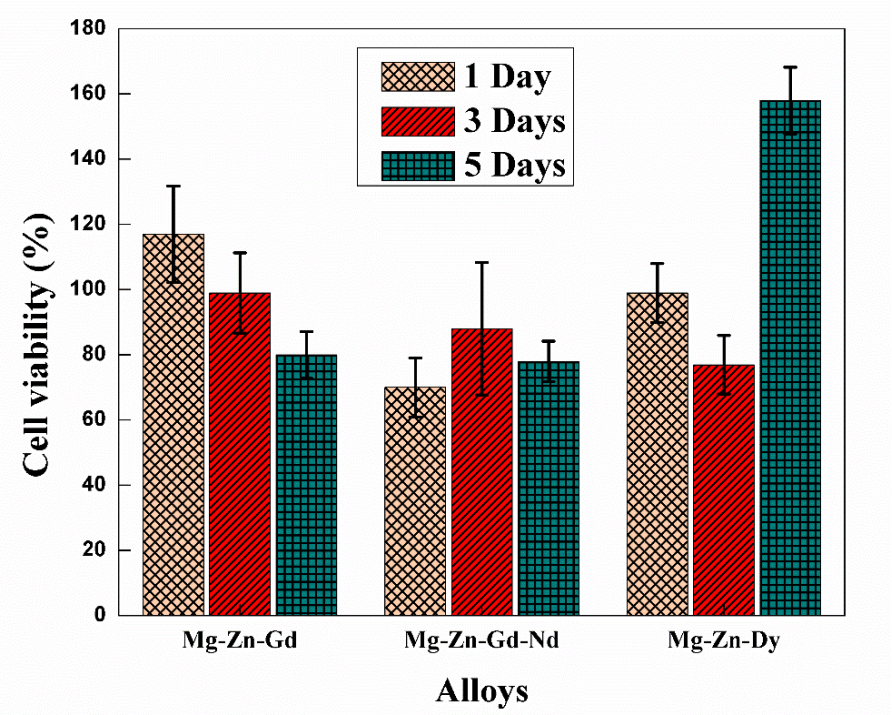

Figure 4.15 The influence of different REE addition on the *in vitro* cell viability,

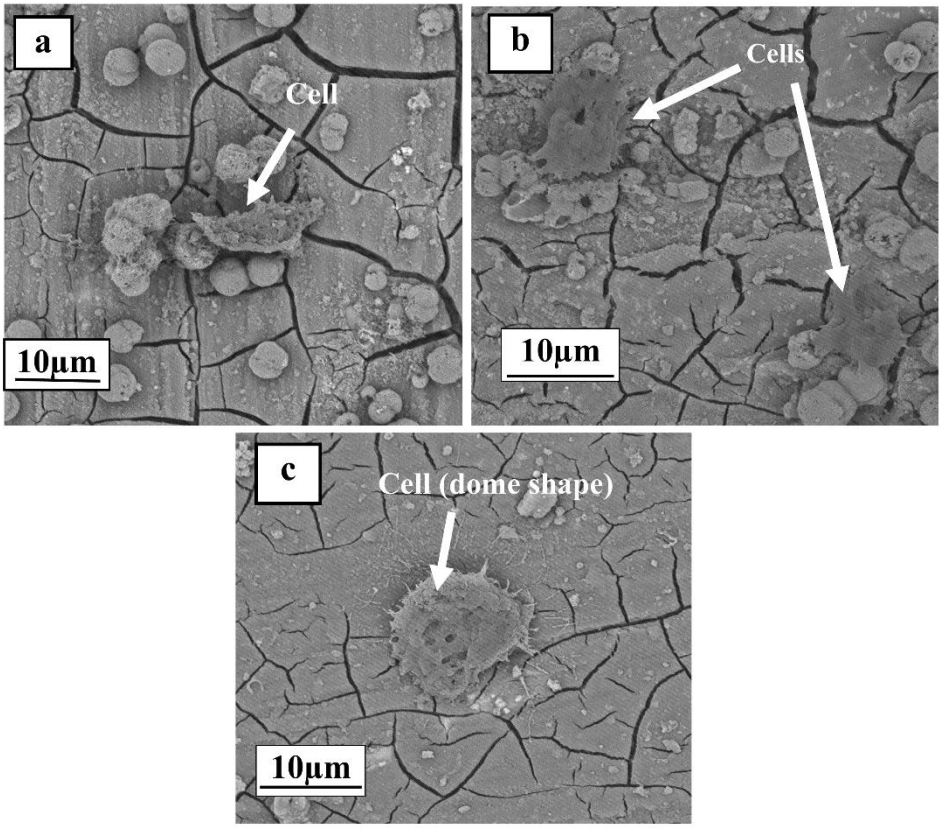

Figure 4.16 SEM micrographs with the morphology of NIH 3T3 cells in (a) Mg-Zn-Gd, (b) Mg-Zn-Dy and (c) Mg-Zn-Gd-Nd alloys after 1 day of cell culturing.

4.1.7 Mechanical properties

The tensile properties of as-cast Mg-Zn-REE alloy samples at room temperature are summarized in **Table 4.5**. Mg-Zn-Gd-Nd and Mg-Zn-Gd alloys showed relatively high yield strength (YS) compared to the Mg-Zn-Dy alloy. The higher strength of these alloys is primarily attributed to the presence of secondary phases and solid solution strengthening of the Mg matrix. Besides, it has also been reported (Xu et al. 2007) (Shao et al. 2010) that attachment of the secondary phase into the metal matrix induces more stress concentration at matrix/particle interface, which leads to nucleation of voids by debonding of matrix/particle interface leads to lowering of the yield strength. In addition, the dislocation pile-up at the interface due to brittleness of the secondary phases causes crack initiation and its easy propagation. This reduces the UTS and the ductility of the alloy. The LPSO phase observed here makes a weak interface with the Mg matrix which leads to the lowering of mechanical properties as compared to that of Mg-Zn-Gd-Nd alloy. The effect of solid solution strengthening due to Zn is also expected to decrease the strength of the alloy (Yang et al. 2008). The improvement in the elongation of Mg-Zn-Gd-Nd was mainly attributed to the changes in the microstructure induced by the increase in the amount of alloying elements (Srinivasan et al. 2014b). However, in Mg-Zn-Dy the formation of coarse secondary phase precipitates in the grain boundary region leads to low elongation (Lu et al. 2015). The fractured surface of Mg-Zn-Gd alloy (**Figure 4.17 (a))** shows a deformed river like pattern with raised edges. **Figure 4.17(b)** shows the fractured surface morphology of the alloy (Mg-Zn-Gd-Nd) illustrating the quasi cleavage fracture with large dimples (faceted texture). Zhang et al. (2012c) reported that the activation of non-basal dislocations changes the fracture pattern from cleavage brittle fracture to quasi cleavage fracture during tensile testing. The presence of these cleavage planes led to a quasi-cleavage mode of fracture. In the Mg-Zn-Dy alloy the presence of a eutectic phase (Mg_8ZnDy) determines the fracture behavior. Rough edges indicate a low bonding strength between the α-Mg matrix and the eutectic phase (Zhang et al. 2014a). It caused the failure of tensile sample at a lower UTS value of 107 MPa.

Table 4.5 Mechanical properties of as cast alloys

Alloys	Ultimate Tensile strength (UTS) (MPa)	Yield strength (YS) (MPa)	Elongation (%)
Mg-Zn-Dy	107±5	43±4	6±2
Mg-Zn-Gd	119±7	62±3	10±0.7
Mg-Zn-Gd-Nd	131±9	65±5	12 ±1

The SEM micrographs **(Figure 4.17 (c))** of Mg-Zn-Dy alloys show relatively flatter areas and cleavage planes with micro cracks. The EDS analysis show that micro cracks occur at the junction of Mg_8ZnDy precipitate and α-Mg matrix. The Mg-Zn-Gd-Nd alloy presents a higher strength (131 MPa) and elongation (12±1%). The eutectic phase which is precipitated along the grain boundary provides an additional barrier to the movement of dislocations resulting in an enhancement in tensile strength. The reported yield strength of Mg-1%Zn is 60.62 MPa (Cai et al. 2012). This shows that there is a significant improvement in the mechanical properties in alloys with addition REE addition as compared to the as-cast Mg-Zn alloy system.

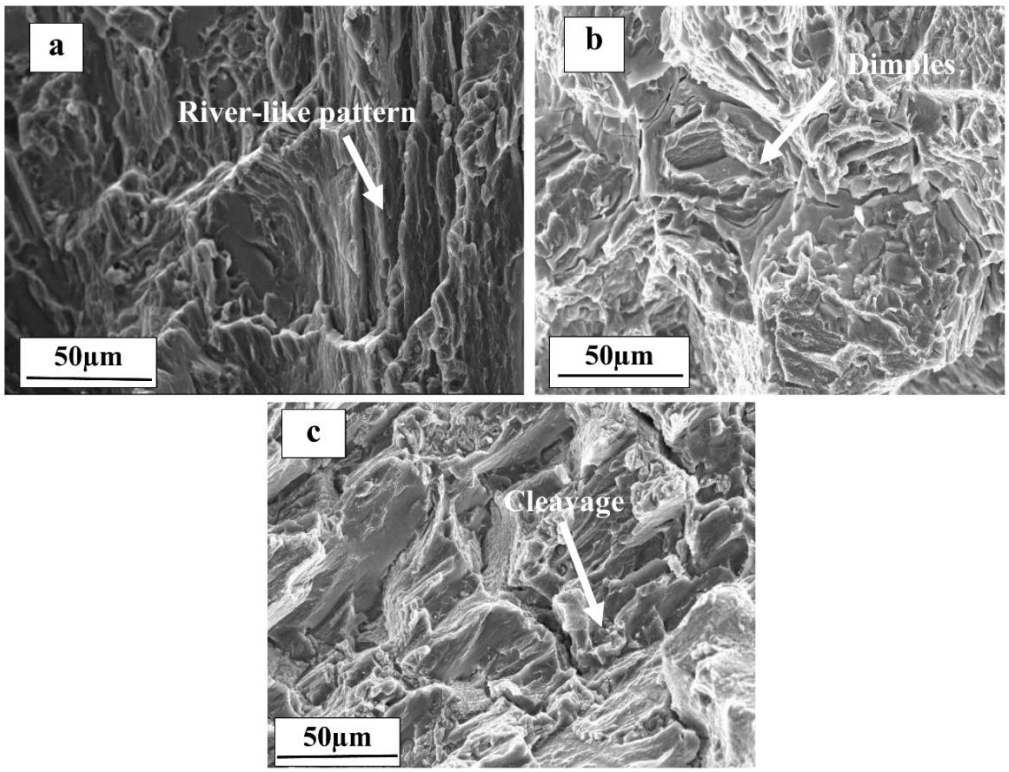

Figure 4.17 SEM micrograph revealing the tensile fracture surface morphology of the (a) Mg-Zn-Gd (b) Mg-Zn-Gd-Nd (c) Mg-Zn-Dy.

4.1.8 Conclusions

Based on the study of as-cast alloy systems, the following conclusions are drawn

- Microstructures of alloys predominantly consist of: lamellar LPSO phase in Mg-Zn-Gd alloy, Mg_8ZnDy particles in Mg-Zn-Dy alloy and $Mg_{12}Nd$ particles in Mg-Zn-Gd-Nd alloy. In addition, few binary phases such as Mg-Zn and Gd-Zn in the form of particles were also present in these alloys.
- The *in vitro* degradation of the alloys in HBSS is obtained and the results showed that addition of Gd to Mg-Zn alloy enhances the corrosion resistance. The corrosion rate obtained from the weight loss is in the order of Mg-Zn-Gd

< Mg-Zn-Gd-Nd < Mg-Zn-Dy. This same trend showed in the results of hydrogen evolution and electrochemical experiments.

- The cell culture study proves the good cytocompatibility of all three alloys. Dense cells adhered well and colonize on the whole surface of the alloys.

- The excellent ductility and tensile strength exhibited by the Mg-Zn-Gd-Nd alloy is due to the strengthening by the eutectic phase. The coarse and continuous LPSO phase at the grain boundaries in the Mg-Zn-Gd alloy leads to moderate ductility. The bulk continuous phase at the grain boundaries of the Mg-Zn-Dy alloy lowers its strength and leads to easy crack propagation.

The following subsections discuss the results of laser surface modified alloys (Mg-Zn-Gd, Mg-Zn-Dy and Mg-Zn-Gd-Nd)

4.2 Studies on laser surface melted (LSM) Mg-Zn-Gd alloy system

This particular section presents the results of the investigation carried out on laser surface melted Mg-Zn-Gd alloy in the aspect of microstructure, wettability behavior, surface hardness and *in-vitro* degradation properties.

4.2.1 Microstructural analysis

Figure 4.18 and **Figure 4.19** show typical cross sectional microstructures of LSM Mg-Zn-Gd alloy processed at different energy density conditions. Significant changes of the microstructures were observed in the LSM zone compared to the untreated substrate. LSM is characterized by rapid heating and cooling rates, which resulted in noticeable refinement in the microstructural features of melted region compared to the substrate. The microstructure of cast Mg-Zn-Gd alloy (as discussed in section 4.1) typically consist of α-Mg dendrites (marked A in **Figure 4.18 (a)**), a eutectic mixture of α-Mg and LPSO phases (marked B in **Figure 4.18 (a)**) and $MgZn_2$/Mg_7Zn_3(Srinivasan et al. 2014b) intermetallic phases (detail discussion in section 4.1). The semi-elliptical region marked in **Figure 4.18 (b)** is the laser-melted region. The depth of this melted region increased from 75 µm to 150 µm with increasing laser energy input (**Table 4.7**, **Figure 4.19**). In addition, the melt depth increased with the increasing laser power and decreasing scan velocity. A minimum depth of 75 µm was observed at 12.5 J/mm^2 (125 W, 20 mm/s) and maximum depth of 150 µm was recorded at 45 J/mm^2 (225 W, 10 mm/s). The depth of the melted region can potentially have strong influence on the corrosion front movement from the surface towards the substrate and therefore overall degradation of the alloy under physiological conditions changes depends on the depth of LSM region. The microstructure of the melt pool, shown **Figure 4.19 (b)** is found to contain an extremely fine equiaxed dendrite (enlarged view **Figure 4.18 (c)**) network at the top region and columnar network (enlarged view **Figure 4.18 (d)**) in the bottom region of the meltpool. In this highly refined zone the grain size was in the range of 1-2 µm and laser processing parameters appear to have measurable influence on grain size and meltpool depth **(Table 4.7).** The results showed that at low energy input the average grain size is slightly larger than higher energy condition. However, the grain size values are

statistically not different as the variation in the grain size within the same sample is high due to the variation in the cooling rates. The grain size of the substrate was about ~ 20µm (**Figure 4.18(a)),** which is significantly higher than that observed in LSM regions. The observed microstructural refinement is attributed to the high cooling rates associated with LSM. The coarser columnar dendritic network in **Figure 4.18 (b, d)** at the bottom of the melt pool is mainly due to the reduction in solidification rate with increased melt pool depth and also due to directional heat extraction through the substrate. As the population of equiaxed cells increased at higher energy condition, this indicated that high energy density leads to high temperature gradients (Ho et al. 2015b). A distinct heat affected zone (HAZ) was also seen **(Figure 4.18 (d))** at the interface of the laser melted region and substrate. In the HAZ the extended network of fine cells is randomly formed and is morphologically visible. The compositional distribution analysis by EDS shows that there is some enrichment and homogenization of Zn and Gd within the LSM region (same trend was oberved by Manne et al. (2018)). With increasing energy density the solute enrichment in the meltpool also increased. This is evident in the combinations 45 J/mm^2 (Zn = 2.2$\pm$0.8, Gd= 2.8$\pm$0.6), 12.5 J/mm^2 (Zn= 1.8$\pm$0.6, Gd = 2$\pm$0.8) where the heat input resulted in enrichments of solutes in the melted region as compared to as cast alloy (**Table 4.6**).

Table 4.6 Typical composition of laser melted zone and as cast Mg-Zn-Gd alloys analyzed by EDS (wt. %)

Sample conditions(Within the grain)	**Mg**	**Zn**	**Gd**
As cast alloy	96.9$\pm$0.8	1.2$\pm$0.4	1.7$\pm$0.6
12.5 J/mm^2	95.8$\pm$0.5	1.8$\pm$0.6	2$\pm$0.8
45 J/mm^2	94.7$\pm$0.5	2.2$\pm$0.8	2.8$\pm$0.6

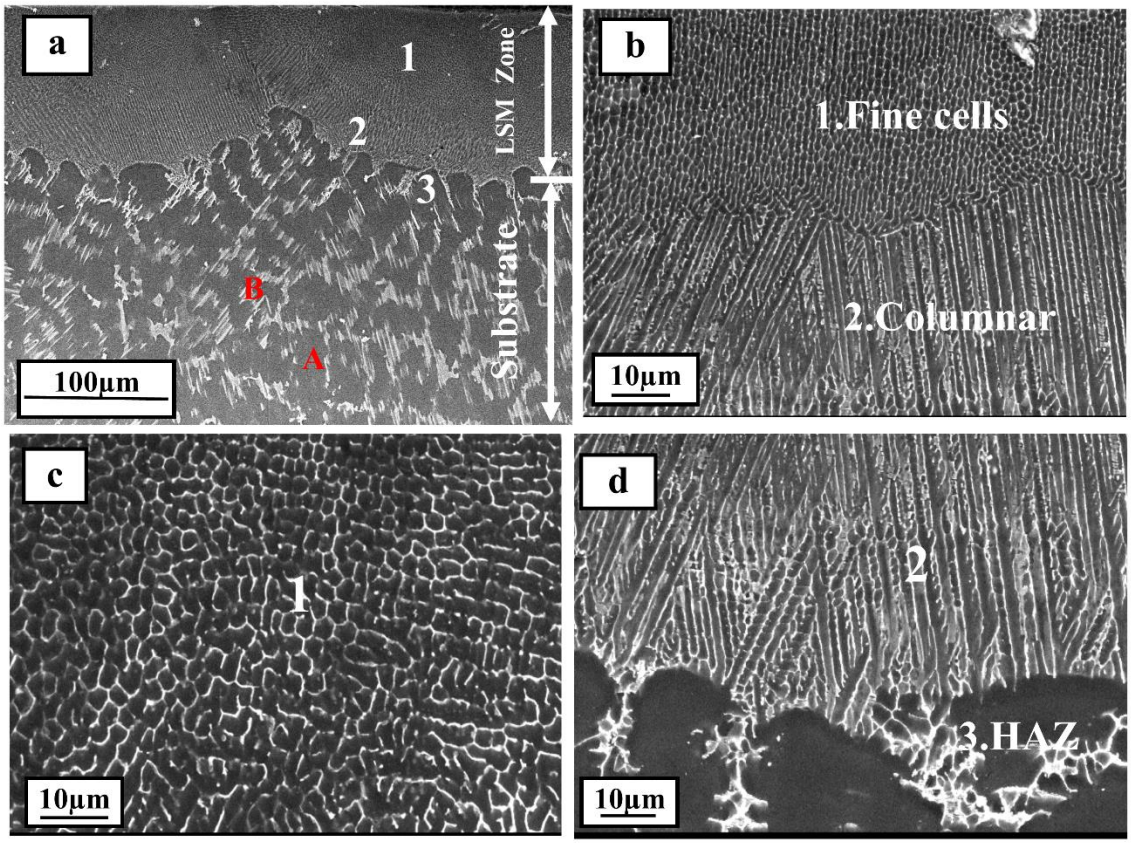

Figure 4.18 Typical cross sectional SEM microstructures of (a) Laser surface melted Mg-Zn-Gd alloy (b) enlarged LSM zone (at 25 J/mm^2) (c) enlarged view of top region of the melt pool (d) Bottom region of the melt pool with heat affected zone (HAZ).

Table 4.7 Laser parameters, melt pool depths, grain size and roughness of LSM Mg-Zn-Gd alloy.

Parameters (Power (W)/ Velocity mm/s)	**Laser energy density (J/mm^2)**	**Melt pool depth (µm)**	**Average Grain size (µm)**	**Roughness (S_q) (µm)**
As- cast	----	----	20±0.5	1.88±0.1
125/20	12.5	75±1	2.41±0.6	4±1
175/20	17.5	111±3	2.34±0.3	4.6±0.5
225/20	22.5	138±5	2.12±0.5	5.3±0.8
125/10	25	140±3	2.01±0.2	4.9±1
175/10	35	148±4	1.92±0.5	5.8±0.3
225/10	45	150±5	1.73±0.4	13±1

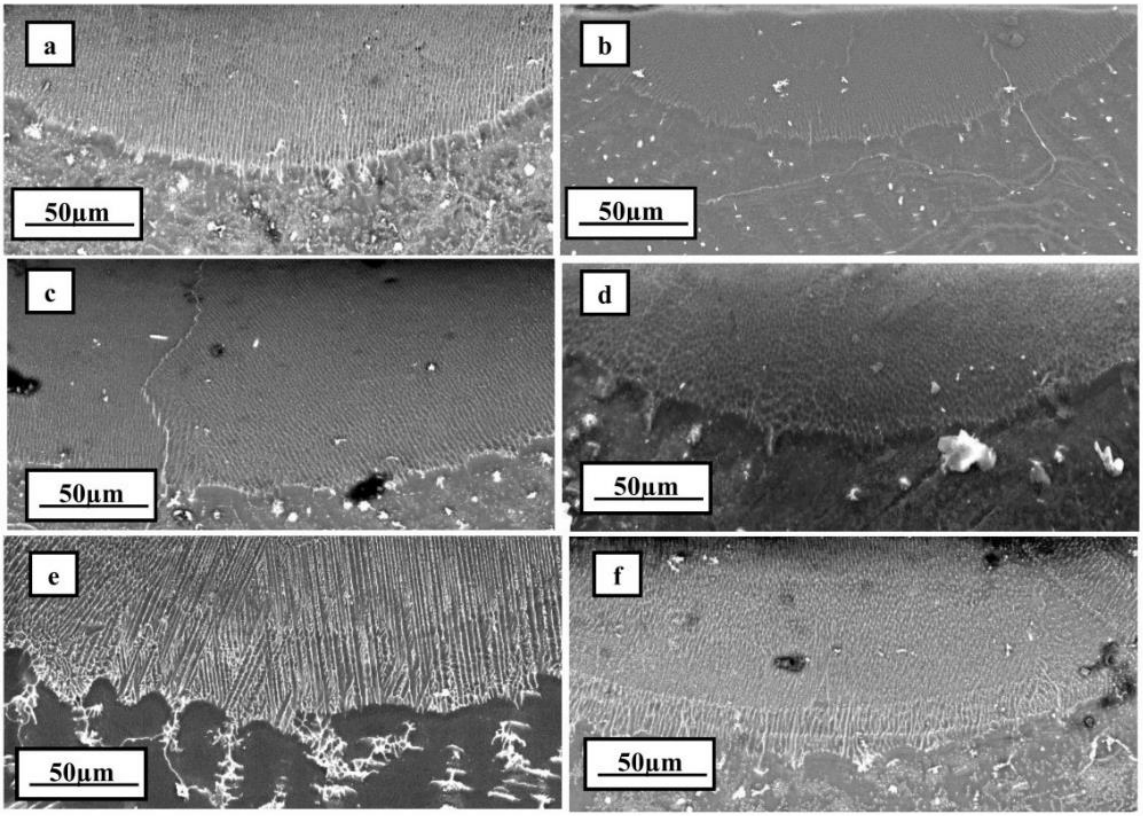

Figure 4.19 Cross sectional (SEM) micrograph of LSM sample with meltpool at energy densities of (a) 12.5 J/mm^2 (b) 17.5 J/mm^2 (c) 22.5 J/mm^2 (d) 25 J/mm^2 (e) 35 J/mm^2 (f) 45 J/mm^2

4.2.2 Phase analysis

Figure 4.20 shows the XRD pattern of as-cast and LSM Mg-Zn-Gd alloy. The results indicate that the major peaks of all samples correspond to α-Mg phase (ICDD-PDF file no: 00-004-0770). The remaining peaks of Mg_7Zn_3 (Datta et al. 2011) indicate the secondary intermetallic phases. It is noticed that the dominating diffraction peaks at 2θ =32.19 °, 34.4° and 36.63 ° could be assigned to (100), (002) and (101) planes of α-Mg respectively. After LSM the relative intensity of (101) increased, which suggests preferred grain orientation in the LSM region of the alloy. Some extra peaks were observed for the laser-melted sample along with the main peaks. This may be due to the change in lattice constants resulting from rapid melting and solidification which in turn leads to the formation of some intermetallic or metastable compounds (Ho et al. 2015a).

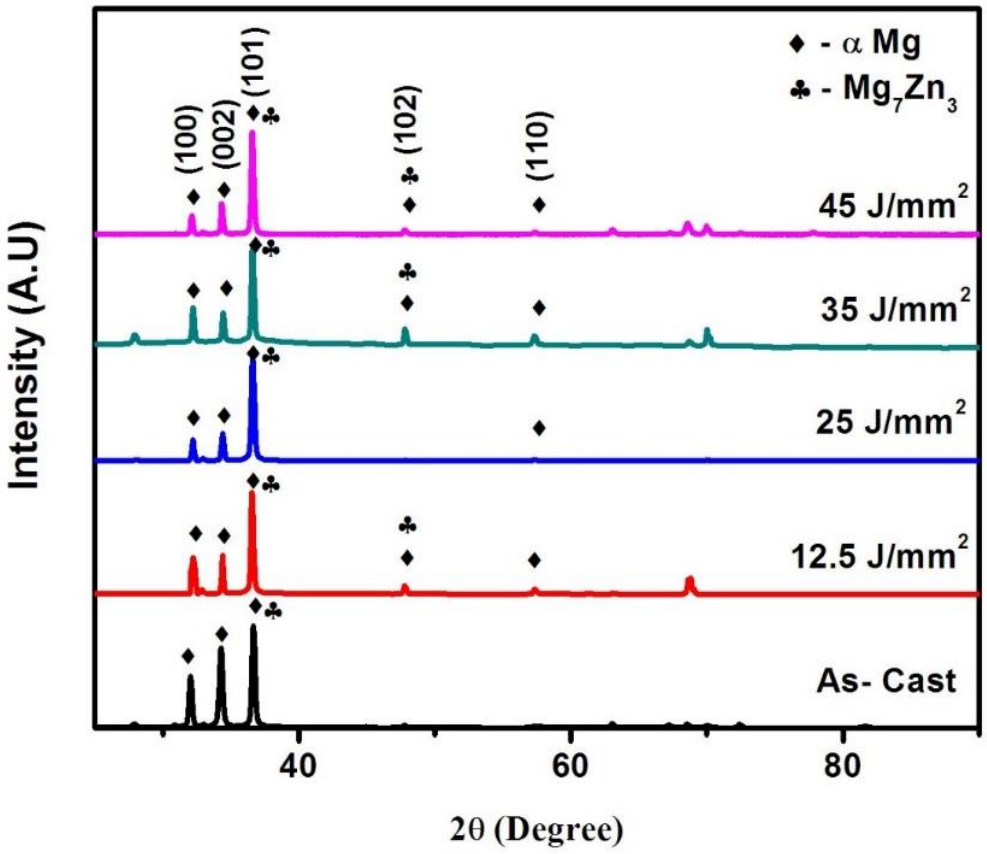

Figure 4.20 Comparison of XRD results of as cast and selected LSM Mg-Zn-Gd alloy

4.2.3 Microhardness distribution

The influence of LSM on the surface hardness of Mg-Zn-Gd alloy is presented in **Figure 4.21**. The average hardness of LSM samples ranged between 82 HV and 120 HV, whereas the hardness of the as cast sample is 75 HV. The improved hardness of LSM samples is due to grain refinement and solid solution strengthening (Wei et al. 2014). The average microhardness of laser melted alloy changed with the laser power and velocity. The samples exhibited low hardness at lower energy density conditions (12.5 J/mm^2), mainly attributable by the coarse microstructural features in the melted zone. Once the laser energy input increased to 17.5 J/mm^2, the hardness also increased as a result of formation of fine grains in the melt zone. Maximum hardness of 120 HV was observed in the samples processed at an energy density of 35 J/mm^2. This

improvement in hardness shows that more fine grains were formed at extremely rapid cooling rates. There is a slight decrease in hardness at an energy density of 45 J/mm^2. The reason for this decrease may be attributed to the grain size variations with increase in scan velocity.

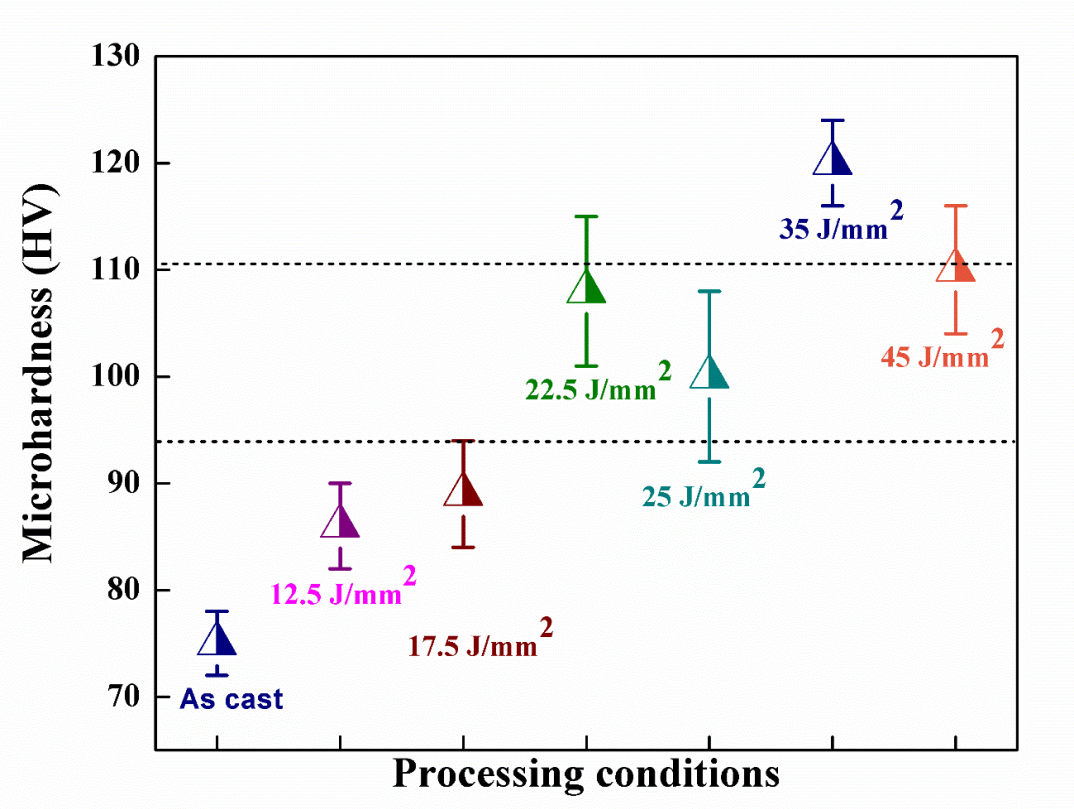

Figure 4.21 Hardness distribution in as cast and LSM Mg-Zn-Gd samples

4.2.4 Surface roughness analysis of LSM samples

The changes in the surface roughness of Mg-Zn-Gd alloy due to LSM are presented in **Table 4.7** and **Figure 4.22**. **Figure 4.22 (a)** mainly shows the typical SEM image of the laser treated surface. The selected area (white in colour) is the SEM image of LSM surface in **Figure 4.22 (a)** is scanned for surface roughness measurement. In general, the surface roughness increased with LSM and gradual increase in the roughness was also observed with increasing laser energy density. The surface roughness (S_q) of LSM samples ranged from 4±1 µm to 13±1 µm, when the laser energy density was increased from 12.5 J/mm^2 to 45 J/mm^2. Various researchers ((Semak and Matsunawa 1999), (Kurella et al. 2008), (Vora et al. 2012) and (Vora et al. 2013)) have reported that recoil

pressure due to rapid heating generates a hydrodynamic melt motion inside the melt pool. These motions of the liquid metal are sufficient to eject melt towards the material interaction zone and lead to the formation of liquid pile-up. Later on the gravitational force tries to pull back the liquid metal towards the melt pool (Semak and Matsunawa 1999). When the cooling rates are high during LSM, the liquid metal solidifies quickly, forming deep grooves and high peaks on the LSM surfaces (Ho et al. 2015a). The increase in the surface roughness with increase in the laser energy density could be due to high recoil pressure-induced shock waves at higher energy densities.

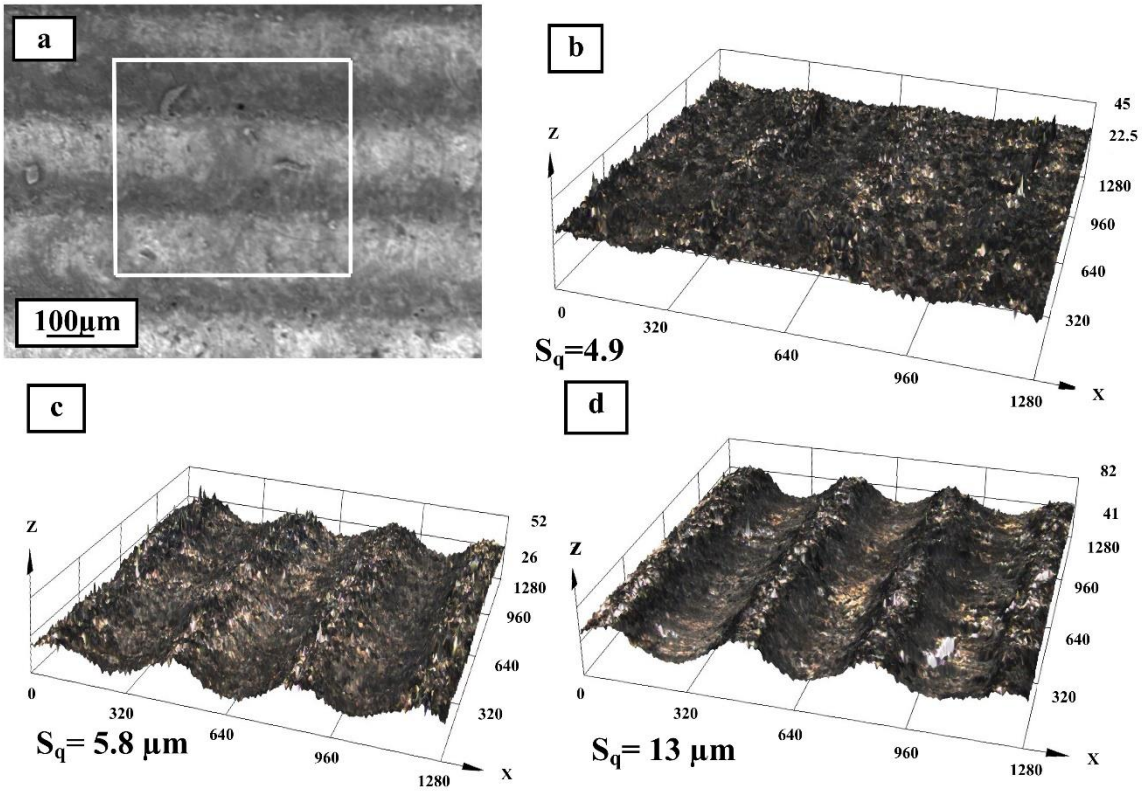

Figure 4.22 Surface topographies of laser treated Mg-Zn-Gd alloy (a) SEM image, Roughness (3D maps) profiles at (b) 25 J/mm^2 (c) 35 J/mm^2 (d) 45 J/mm^2

4.2.5 Wettability behaviour

The quantitative analysis of surface wettability of LSM samples, before and after polishing, was carried out using DI water (polar). **Figure 4.23** represents the schematic of wettability measurement on as-cast and LSM samples. **Table 4.8** shows the contact

angles and surface energy of as-cast, LSM and polished LSM samples. Growth and adhesion of cells on the surface of the laser processed alloys are influenced by surface characteristics such as surface energy, surface roughness, surface geometry, chemical composition (Rosales-Leal et al. 2010) and microstructural features such as grain size (Demir et al. 2014, Kurella et al. 2008 and Ho et al. 2015b). At low laser energy densities, the unpolished LSM sample surface was nearly hydrophilic and hence, can promote cellular adhesion. As a result, better mineralization could be achieved on these samples with low contact angles and higher surface energy (Ho et al. 2015a). As the value of contact angle increased gradually and reached 103 $\pm$ 10° with increase in the laser energy density, the surface energy of these samples was found to be low. At the highest energy density conditions (35 J/mm^2, 45 J/mm^2), the surface of the sample showed hydrophobic nature similar to as-cast samples (90 $\pm$ 3°), which can led to poor cell attachment on these samples. The changes in the solidification cooling rate as a function of laser energy density resulted in variations in the surface roughness, microstructural features and thereby altered the wettability of present samples (Ho et al. 2015b). As-cast samples with a roughness of 1.88 $\pm$ 0.1 µm and grain size of 20 $\pm$ 0.5 µm exhibited a surface energy of 30 $\pm$ 6 mN/m. However, after LSM the surface roughness of the samples increased significantly (**Table 4.7**) and up to 10 times lower grain size was achieved on these samples. Further, some solute enrichment was also observed in the LSM regions (**Table 4.6**). All these changes resulted in enhancement in the wettability of LSM samples. However, it is important to note that the LSM samples showed more or less similar wettability and surface energy irrespective of laser energy density. This could be due to small variations among the samples in terms of surface roughness and grain size (**Table 4.7** and **Table 4.8**). Overall, the LSM samples showed relatively better wettability and surface energy than as-cast samples. However, it is not clear whether this improvement is due to changes in the surface roughness or microstructure and small composition variations due to LSM. Therefore, the wettability of samples were assessed again after polishing the samples to ensure similar surface roughness (~ Sq= 1 µm) to understand the effect of microstructural and compositional changes due to LSM on wetting behavior. Since the polished samples have similar surface roughness the influence of surface roughness on wettability is ignored. The results show (**Table 4.8**) that after polishing the wettability and surface roughness of

as-cast samples did not change as there is no change in the microstructure and composition in these samples after polishing. On the other hand, the wettability and surface energy of polished LSM samples showed distinguishable change, which can be attributed to the changes in the microstructure (grain refinement) and solute enrichment in LSM region, which are absent in as-cast samples. Although small, the LSM samples showed relatively better wettability than as-cast samples. The variation in the contact angle is influenced by the reduction in average grain size (Ho et al. 2015b) and variations in chemical composition due to solute enrichment, presence of multiple phases (Kurella et al. 2008). The EDS results confirmed (**Table 4.6**) that the concentration of Mg, Zn and Gd in the grains and grain boundaries vary with different laser energy densities and therefore, the grain and grain boundary interactions with a water molecule appears to be different. These results also indicate that relatively better wettability on LSM samples can be achieved after polishing, where the direct influence of grain refinement and solute enrichment was observed.

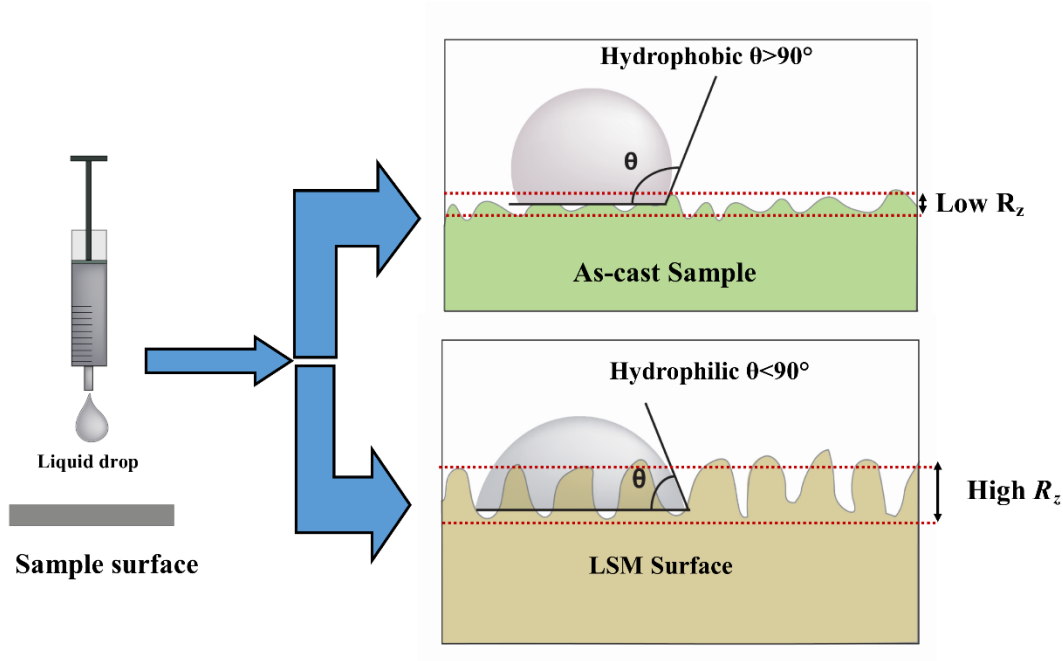

Figure 4.23 Schematic of contact angle analysis on as-cast and LSM sample surface by using polar liquid (DI Water) (R_z represents the line roughness)

Table 4.8 Effect of LSM at different laser energy densities on the surface energy and contact angle of as cast, LSM and polished LSM sample

	LSM samples		Polished LSM samples	
Parameters (J/mm^2)	contact angle (˚) DI water	Surface free energy (mN/m)	contact angle (˚) DI water	Surface free energy (mN/m)
As cast	90±3	30±6	90±3	30±6
12.5	72±7	39.0±8.3	75±8	40±5
17.5	79±9	34.3±5.6	75±8	39±4
22.5	83±6	35.3±3.7	77±4	37±5
25	83±8	33.5±5.9	80±10	37±3
35	91±7	28.01±4.9	84±8	37±3
45	103±10	32.2±3.5	89±8	35±2

4.2.6 *In-vitro* degradation-Immersion method

Overall degradation kinetics of laser treated Mg-Zn-Gd alloy was assessed in terms of hydrogen evolution and Mg^{2+} ion release during static immersion in HBSS as represented in **Figure 4.24** and **Figure 4.25**. All samples including as- cast alloy were fine polished to maintain Sq of ~1µm to eliminate the influence of surface roughness on corrosion. The measured hydrogen evolution of LSM samples compared to as-cast Mg-Zn-Gd during immersion in HBSS is represented in the **Figure 4.24**. At all processing conditions the release of hydrogen volume increases with increase in immersion time. The same trends have been reported in AZ91D alloy also by Taltavull et al. (2014). The sample processed at lower energy density (12.5 J/mm^2) exhibited the highest hydrogen evolution (1.35 ml/cm^2) suggesting its low corrosion resistance than as cast Mg-Zn-Gd. This could be mainly due to the unstable passive film formation during immersion in HBSS and the lower overlapping of meltpool (**Figure 4.28(b)**) The rate of hydrogen evolution was found to be high during initial ~ 100 h of immersion for samples treated with 12.5 J/mm^2 and 25 J/mm^2 laser processing conditions, which showed 1.35 ml/cm^2 and 1.6 ml/cm^2 hydrogen evolution, respectively. The slope of hydrogen evolution curves was relatively low for the samples processed at high energy density and exhibited a lower corrosion rate. For example, after 140 h of immersion the

hydrogen evolution almost became stable for samples treated at 45 J/mm^2, 35 J/mm^2 and 22.5 J/mm^2. Among all the processing conditions 45 J/mm^2 had higher corrosion resistance with the lowest hydrogen evolution. This could be due to a persistent stable passive film on its surface that shows the range of passivation is better in these conditions. The rate of hydrogen evolution up to 100 h (slope of hydrogen evolution vs. time) for 45 J/mm^2 also shows a lower value 0.0024 ml/cm^2/h compared to 12.5 J/mm^2 (0.02 ml/cm^2/h) and as-cast (0.16 ml/cm^2/h) conditions. Similarly, the hydrogen evolution at 22.5 J/mm^2 is 0.006 ml/cm^2/h which is very much lower than the 0.29 ml/cm^2/h measured at 35 J/mm^2 condition.

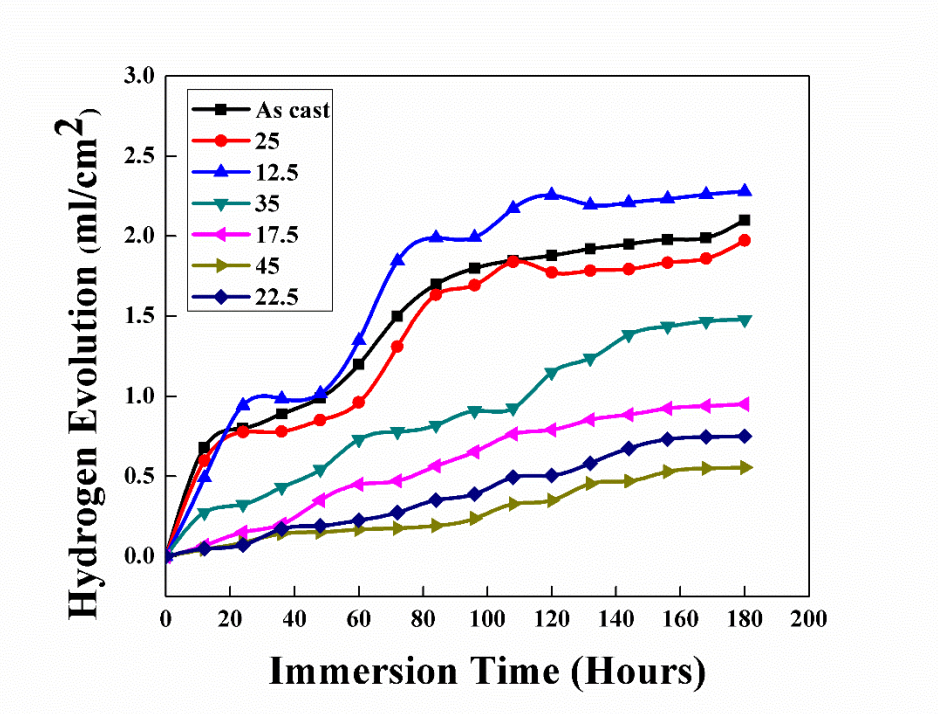

Figure 4.24 Rate of hydrogen evolution from as-cast and LSM Mg-Zn-Gd samples during immersion in HBSS (All the LSM units are in J/mm^2)

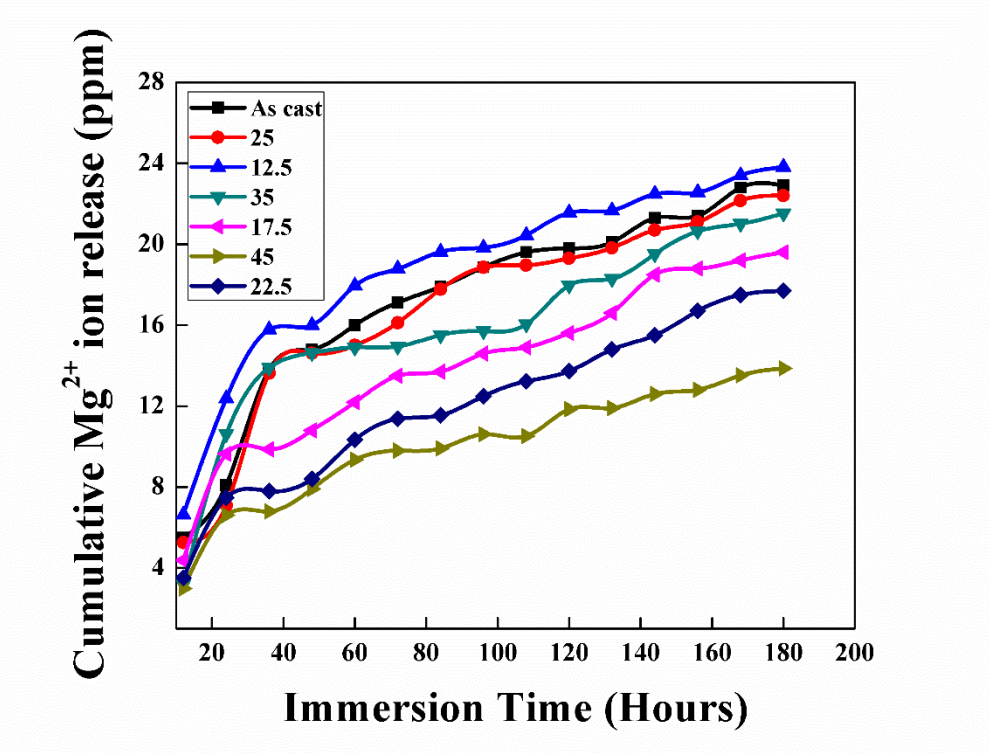

Figure 4.25 Cumulative Mg $^{2+}$ ion release from as-cast and LSM Mg-Zn-Gd samples during immersion in HBSS (All the LSM units are in J/mm^2)

The anodic reaction of Mg results in the formation of Mg^{2+} ions and therefore, analysis of Mg^{2+} ion release during immersion can give the extent of alloy degradation. **Figure 4.25** shows the cumulative Mg^{2+} ion release of different samples as a function of immersion time, the ion release trend was found to be in line with the hydrogen evolution trend. There is a sharp increase in ion release during the initial 20 h of immersion for all processed samples. This could be mainly due to high rate of anodic dissolution. Samples processed at higher energy density (45 J/mm^2) showed lower ion release (13.9 ppm) which matches the trend of the hydrogen evolution plot. This lower ion release could be due to the stability of the passive film which is formed and persistent after 140 h of immersion. As compared to the as cast samples there is strong reduction (~130 %) in Mg^{2+} ions release for sample processed at higher laser energy condition. The maximum possible Mg^{2+} release of 23 ppm was observed for 12.5 J/mm^2 condition with maximum damage on the surface as well as cross section (**Figure 4.27(b)**).

The highly reactive nature of Mg causes fast surface corrosion. Hence, it is essential to provide for a thicker LSM layer for extended corrosion protection. The corrosion rate of different samples, calculated using the weight loss method, is summarized in **Figure 4.26**. The *in vitro* degradation rates of LSM samples after surface polishing were found to match very well the hydrogen evolution and Mg^{2+} ion release data. The data clearly showed that LSM decreases the corrosion rate of Mg-Zn-Gd alloy. The corrosion rate of laser processed sample decreased by 53 % for 45 J/mm^2 samples compared to as-cast alloy. The decrease in trend could be due to the reduction in active ionic concentration and the reduction of any oxide layer which is formed during LSM. At high power and scan velocities of 10 mm/s and 20 mm/s, the corrosion rate decreased due to the homogenous chemical composition, higher enrichment of Zn and Gd in the melt zone and enhanced melt pool depth. This prolongs the corrosion propagation to reach the melt pool boundary. The samples processed at low energy density (12.5 J/mm^2) showed no improvement in corrosion resistance owing to solidification crack, insufficient melt pool track overlapping and shallow meltpool depth (**Figure 4.28(b)**). The corrosion in the current LSM Mg-Zn-Gd alloy is mainly due to the active ions present at the laser track, corrosion due to the formation of galvanic cell between α-Mg and secondary phases (between the remelted and unmelted region of the alloy). Once the corrosion starts, the propagation of corrosion front presumed to advance due to (i) the corrosion potential exist between the meltpool, meltpool boundary and the substrate (ii) differences in internal stress between substrate and meltpool, which could initiate stress corrosion. Therefore, samples with a low melt pool depth samples would experience higher degradation rates. In meltpool region of LSM, equiaxed and fine grains with or without secondary phases at the grain boundaries and extended enhanced solid solubility of alloying element leads to increased corrosion resistance (Datta et al. 2011) and (Wei et al. 2014). Moreover, suitable melt depth is required to make use of such benefits in the long time corrosion tests. However, the results shows that 25 J/mm^2 and 12.5 J/mm^2 samples have the corrosion rates of 1.8$\pm$0.4 and 2.1$\pm$0.3 mmpy which is higher than that of as-cast Mg-Zn-Gd (1.7$\pm$0.4 mmpy) mainly due to their shallow meltpool depth with lower overlapping and possible presence of cracks. At high heat input resulted enrichment of solute atoms in α-Mg matrix increased the resistance against the pitting corrosion (Coy

et al. 2010a). When compared to 45 J/mm^2 (0.8±0.2 mmpy) and 22.5 J/mm^2 (1.2±0.2 mmpy) conditions as-cast Mg-Zn-Gd alloy (1.7±0.4 mmpy) shows no higher enrichment of solute atoms leads to lower resistance to pitting mode of corrosion.

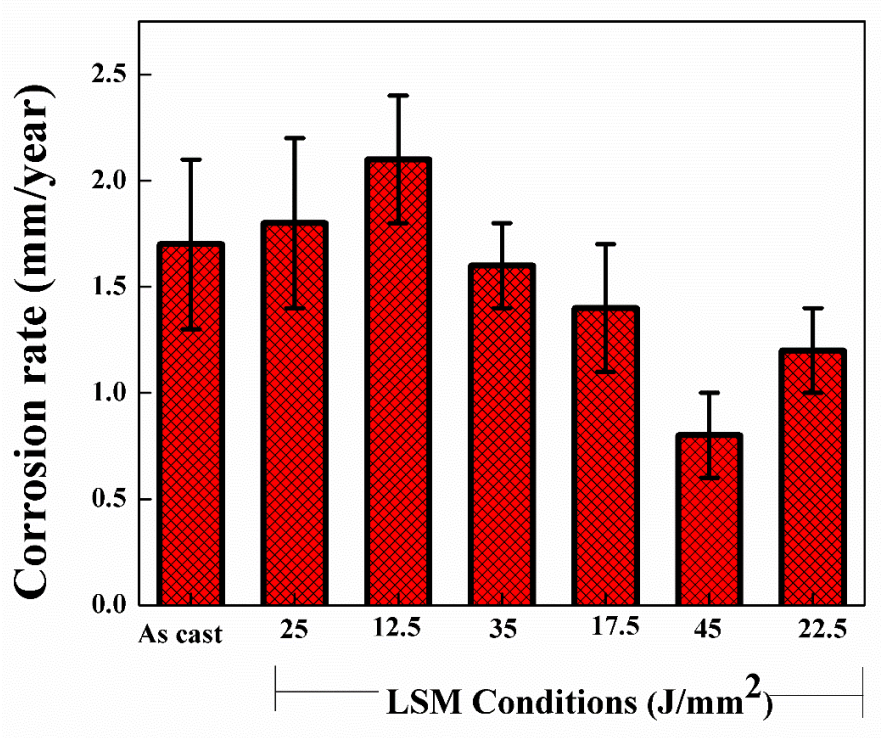

Figure 4.26 Corrosion rate comparison of as cast and LSM Mg-Zn-Gd alloy samples by weight loss method after 180 hours of immersion in HBSS

4.2.7 Corrosion damage characterization

To determine the depth of corrosion penetration and its correlation with meltpool depth, the microstructure of cross sectional samples of as-cast, 12.5 J/mm^2 and 45 J/mm^2 samples after 180 hours of immersion were studied with SEM. The corroded area extended deeply into the interior and formed a pit of 1.3 mm width and 1.1 mm depth in as-cast Mg-Zn-Gd alloy (**Figure 4.27(a)**). The 12.5 J/mm^2 LSM samples showed that the melt pool tracks did not significantly overlap (**Figure 4.28(b)**). This will lead to the faster corrosion propagation through the interface of the two successive laser scans. **Figure 4.27 (b)** shows that corrosion front slowly moves through the substrate by crossing the melt pool region. Owing to the difference in the anodic and cathodic ratio between the substrate and meltpool boundary, many corrosion sites will form.

These corrosion sites will further lead to pit formation (**Figure 4.27(b)**). However, for samples treated at 45 J/mm^2 condition with increased overlapping of meltpool (**Figure 4.28 (b)**) and enhanced meltpool depth prolong long term corrosion rate without visible penetration of corrosion (**Figure 4.27(a)**) thus, indicating their superior corrosion resistance.

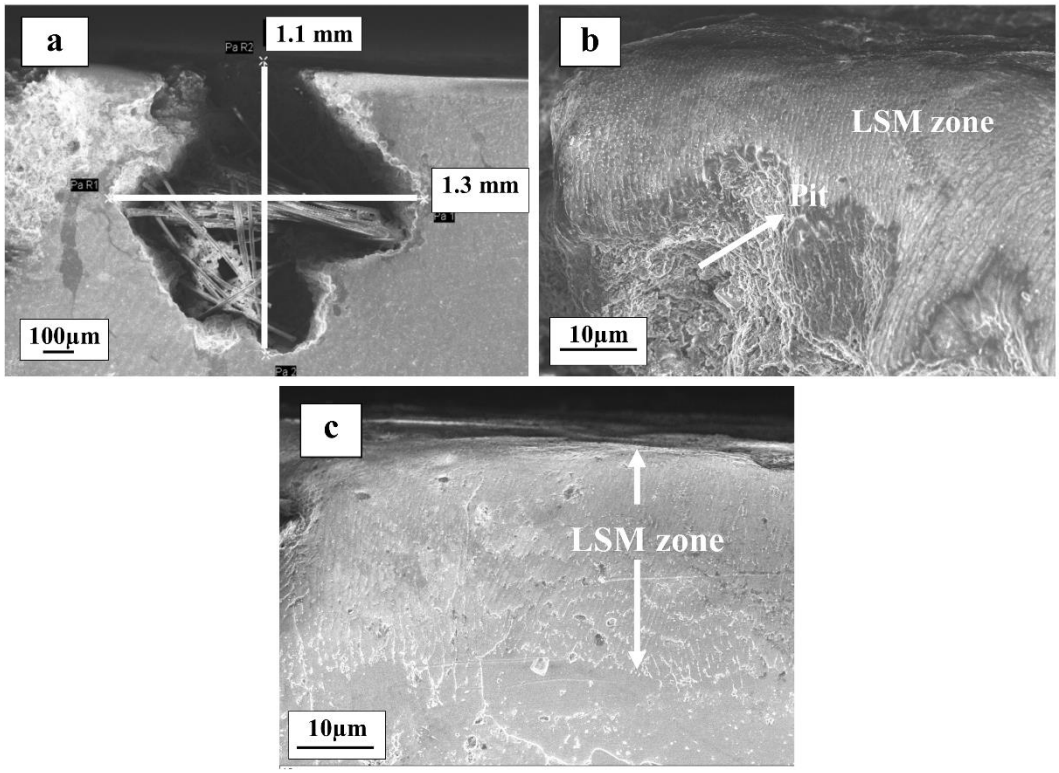

Figure 4.27 Cross sectional view of the corroded surface after immersion in HBSS for 180 h (a) As- cast Mg-Zn-Gd alloy and laser treated at (b) 12.5 J/mm^2 (c) 45 J/mm^2

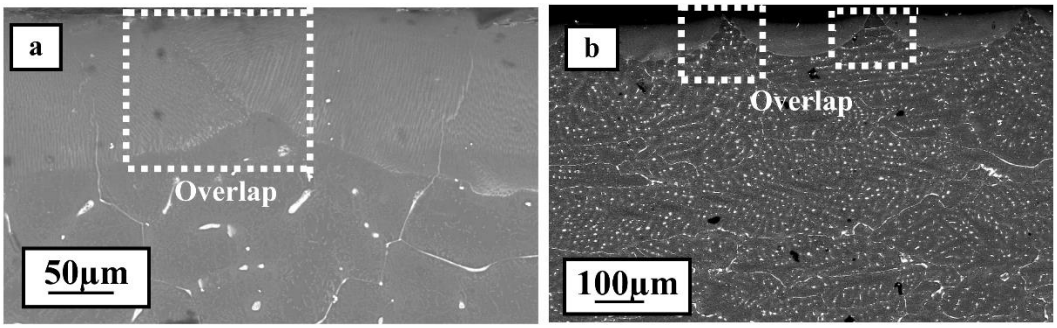

Figure 4.28 Cross sectional view meltpool overlapping variations at (a) 12.5 J/mm^2 (b) 45 J/mm^2

To gain improved understanding of the mechanism of corrosion, powder scrapped off from the corroded sample surfaces (25 and 12.5 J/mm^2) were examined by XRD, SEM+EDS and FTIR. **Figure 4.29(a-c)** show the SEM micrographs of top surface of laser melted samples after immersion in HBSS for 180 hours. It is observed that the entire surface has undergone localized corrosion. The SEM images show a porous layer covering the entire surface of the samples. LSM sample processed at 35 J/mm^2 exhibited cracks on the surface (**Figure 4.29 (b)**). When Mg alloy specimens are exposed to HBSS, the anodic reaction resulted in increased Mg^{2+} dissolution and the presence of Cl^- concentration in the solution (Yang et al. 2009). The presence of aggressive Cl^- transform the passive film $Mg(OH)_2$ into more soluble $MgCl_2$. This breakdown of $Mg(OH)_2$ reduces the protected area , finally promoting further corrosion of substrate (Xin et al. 2011) . The formation of $Mg(OH)_2$ was confirmed by XRD analysis shown in **Figure 4.30**. At low energy density (12.5 J/mm^2) (**Figure 4.29 (a)**), the corroded surface revealed a film with large size pits and increased corrosion products. On the other hand, the samples processed at high laser energy density, the amount of corrosion products was noticeably reduced and it is loosely bounded on the surface (**Figure 4.29(b)**). A crack, visible on the surface of corrode sample 35 J/mm^2 (**Figure 4.29(b))** indicates that the oxide films became porous and starts to peel off from the surface during long-term immersion in HBSS. The passive film of $Mg(OH)_2$ is more stable and further movement of corrosion front towards the substrate can be impeded by this layer.

A typical XRD spectrum of corroded surface is presented in **Figure 4.30**. The XRD results confirms the formation of HAp (ICDD-PDF file no: 00-009-0432), $Mg(OH)_2$ (ICDD-PDF file no: 00-044-1482) and $Ca_3(PO_4)$ (ICDD-PDF file no: 00-009-0348). After immersion in HBSS for 180 h. **Figure 4.29 (a.1)** indicates the formation of flower like structure (similar structure was reported by Thi et al. (2010)). The EDS analysis of these products showed the presence of Ca, P, O and Mg suggesting the formation of apatite which will support bone healing. The surface layer also quantifies the Mg and O atomic ratio of 1:2, which implies the presence of $Mg(OH)_2$ (Lei et al. 2012). The emerged $Mg(OH)_2$ film with different layer density favors the effective corrosion protection by slowing down the Mg dissolution. Therefore, considerable amounts of $Mg(OH)_2$ precipitated on the laser melted surface may act as a protection by preventing the direct contact with HBSS. FTIR analysis further confirm the presence of various compounds interpreted from the XRD and SEM + EDS. The FTIR spectra obtained from the corrosion product id shown in the **Figure 4.31.** The sharp absorption band at 3697 cm^{-1} is attributed to the presence of O-H stretching in $Mg(OH)_2$ (Zhu et al. 2011) . The broad absorption band from 3649 cm^{-1} to 3340cm^{-1} also represents the vibration of OH^- band indicates layer associated with apatite (Pekounov and Petrov 2008). The bands at 1066.4 and 552.5 cm^{-1} corresponds to the phosphate (PO_4^{3-}). Finally at weak band around 432 cm^{-1} represents the Mg-O stretching in Mg $(OH)_2$ (also reported by Wang et al. (2010)).

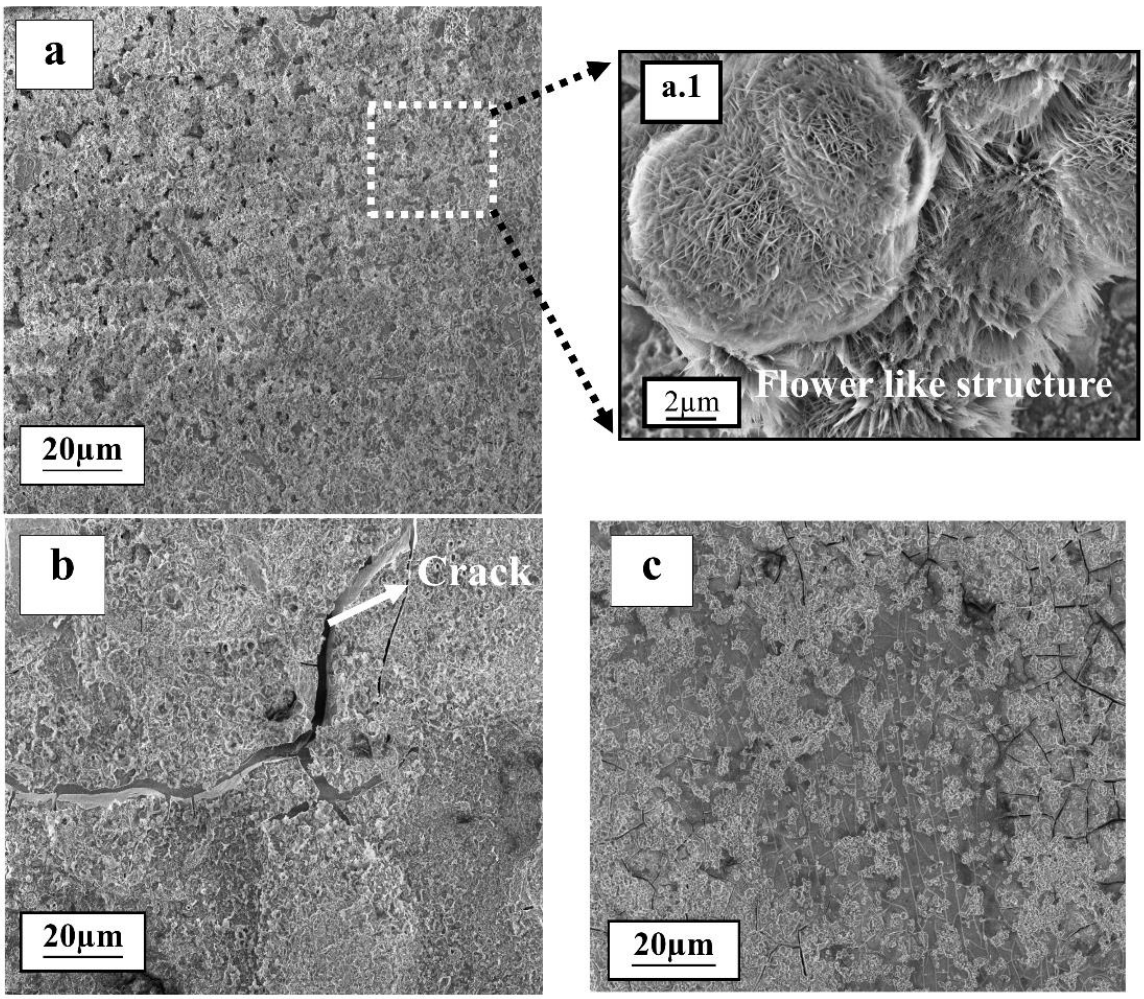

Figure 4.29 Surface morphology of degraded Mg-Zn-Gd alloy (a) 12.5 J/mm^2 (a.1) Enlarged view of the surface product (b) 35 J/mm^2 (c) 45 J/mm^2 laser melted sample immersed in HBSS for 180 hrs.

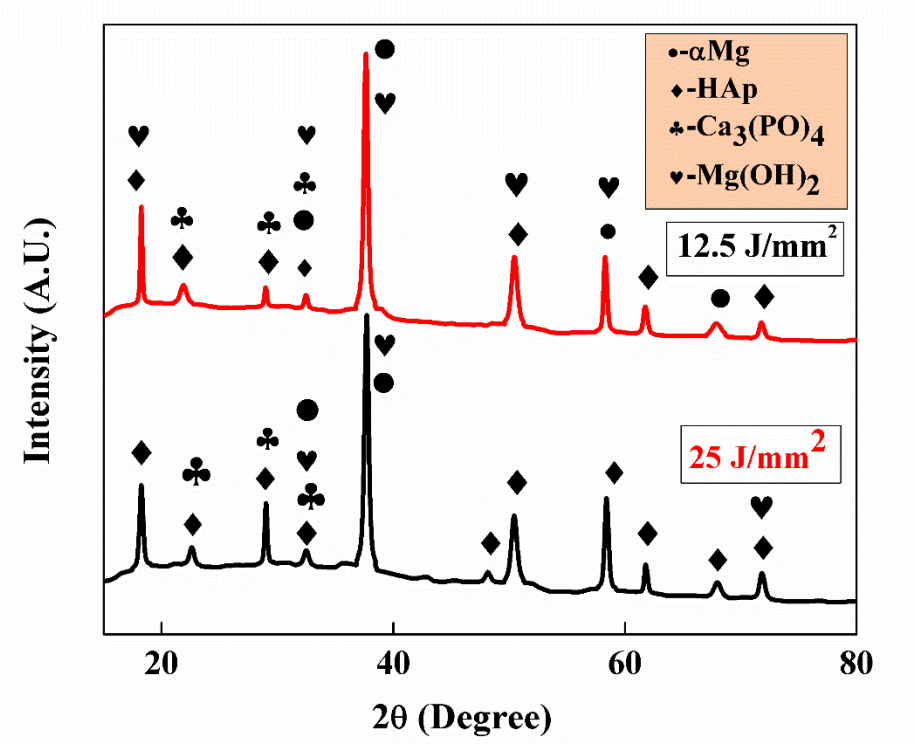

Figure 4.30 XRD spectra of corrosion product extracted from 12.5 J/mm^2 and 25 J/mm^2 laser melted sample immersed in HBSS for 180 hours

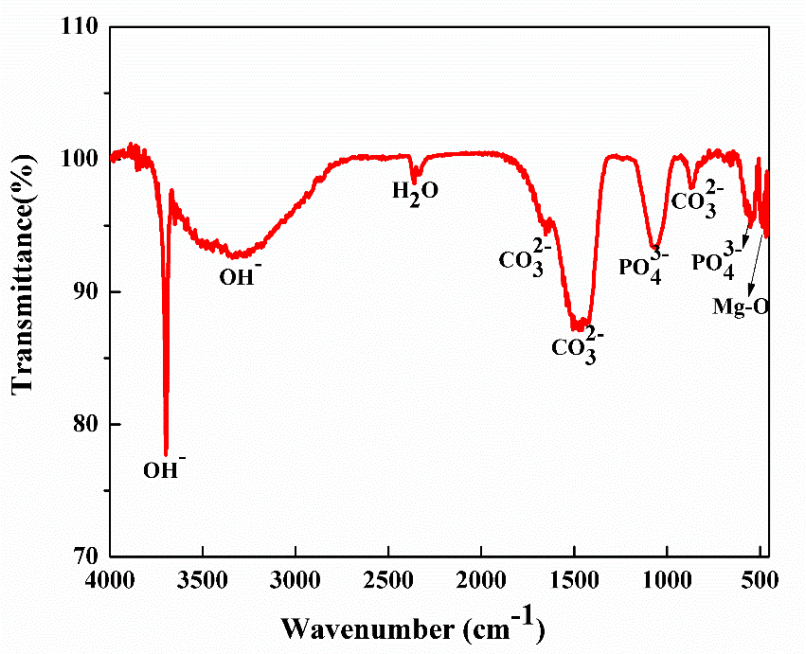

Figure 4.31 FTIR spectra of corrosion product of LSM Mg-Zn-Gd after immersion in HBSS

4.2.8 Conclusions

The effect of laser surface melting on Mg-Zn-Gd alloy was investigated, based on the presented results following conclusions can be drawn.

- Grain refinement and high degree of homogenization was observed due to LSM. The meltpool depth increased with increase in the laser energy density.

- LSM generates a rougher surface texture on the Mg alloy. Due to the rapid melting and vaporization, the induced recoil pressure at the laser material interaction zone generate high velocity melt flow, leading to the deeper valleys and peaks.

- The LSM samples exhibited improved wettability. A maximum surface energy of 40 ± 5 mN/m was obtained for polished samples with lowest contact angle of $75 \pm 8°$, which is expected to facilitate cell adhesion and proliferation on LSM-treated alloy surfaces.

- *In vitro* degradation studies showed clear improvement in corrosion resistance due to LSM. When the alloy was treated at 45 J/mm^2 the corrosion resistance increased by 53% as compared to as-cast samples.

4.3 Studies on laser surface melted Mg-Zn-Dy alloy

This section discusses the influence of laser surface melting on microstructural changes, hardness variation, wettability behaviour and degradation resistance in Mg-1Zn-2Dy (wt. %) alloy.

4.3.1 Microstructural analysis

Figure 4.32 shows the cross sectional microstructures of laser processed Mg-Zn-Dy at different laser energy density conditions. Compared to the substrate notable change in the microstructure were seen in the laser modified zone. Features of as cast microstructure were discussed in the section 4.1. In **Figure 4.32**(**a)** the laser surface melted (LSM) zone was seen as semi elliptical in geometry. There is a transition in the grain morphology from top to bottom of the laser melted zone. It is seen in **Figure 4.32**(**b**) that the top portion of the laser melted zone resolidified as fine cellular grains. This refinement of grains is mainly attributed to the high cooling rates associated in laser surface melting. While, the bottom portion of the laser melted zone is **Figure 4.32(c)**, found to have columnar grains. These elongated grains are mainly formed by the reduction in the solidification speed with increase in the depth of the LSM zone and there by directional heat extraction occurs through the substrate. Remelting at lower energy density promoted the formation of micro cracks in the melt pool zone due to the changes in the generated thermal stresses. The secondary phases (Mg_8ZnDy) present in the alloy were refined and distributed uniformly. The measured grain size of α-Mg in the laser melted zone was 2 µm which is much lower than the substrate grain size of 60 µm. The laser melted zone processed at 25 J/mm^2 and 35 J/mm^2 are represented in the **Figure 4.32**(**d)** and **Figure 4.32(e).** The depth of LSM region is an important factor that decides the life span of the components as the degradation due to corrosion starts from the surface and penetrates through the thickness. Therefore, detailed assessment on the variations in melt pool depth as a function of laser process parameters was carried out and the results are tabulated in **Table 4.9**. Minimum melt pool depth of 98 µm was observed at 45 J/mm^2 and maximum depth of 150 µm was noted at 25 J/mm^2. At higher energy density the depth of the melt pool decreases due to more loss of material from the surface as a result of evaporation during LSM. At lower energy density conditions comparatively continuous scan track with regular overlap of

meltpool was observed. Apart from laser power, velocity significantly affects the meltpool morphology. The depth of the melt pool increases with increase in the velocity. In LSM the melt pool dimensions can be related to laser energy density by **equation 4-4** (Balla and Bandyopadhyay 2010).

$$\mathbf{I = \frac{Q}{V \cdot D}} \qquad \textbf{4-4}$$

The total heat input (I) is related with laser power (Q), scan velocity (V) and diameter of the laser beam (D). It can be seen that with increasing laser power the heat input increases, which shall increase the melt pool size. However, the experimental results do not follow this trend (**Table 4.9**). This can be attributed to the partial evaporation of the alloy surface as a result of high melt pool temperatures generated at the surface of the meltpool due to higher resident time of laser beam at low scan velocities or high power (Manne et al. 2018). The resident time of laser beam on the alloy surface can be calculated as the ratio of laser beam diameter to scan velocity. This results in resident times of 0.5 s and 0.25 s for scan velocities of 10 mm/s and 20 mm/s respectively. Therefore, the partial evaporation of surface during the laser melting causes decrease in the meltpool depth. When the high power laser beam is incident on the surface, localized melting and evaporation of material starts by absorbing the laser energy. The increased incident power generally increases the vaporization rate and marangoni flow by increasing the temperature in the meltpool (Vora et al. 2012). When a higher energy density of 45 J/mm^2 is applied on the surface for a shorter incident time, it generates liquids to flow outwards to the pool edge to greater extent. This creates a meltpool with a concave bottom with reduced depth at higher energy density (similar meltpool morpholgy was reported by Fotovvati et al. (2018)).

Table 4.9 Laser processing conditions and measured melt pool depth

Power (W)/Velocity (mm/s)	**Energy density (J/mm^2)**	**Meltpool depth (µm)**
(125/120)	12.5	150±5
(175/20)	17.5	109±4
(225/20)	22.5	109± 6
125/10	25	142±5
175/10	35	100±4
225/10	45	98±6

During normal solidification of this alloy, the Dy atoms accumulate at solid/liquid interface due to their low solid solubility at low temperatures and cannot diffuse away from the grain boundaries (Guangli et al. 2016). Therefore, the concentration of Dy within the grains of as cast alloy will be low. However, during LSM the rapid heating and cooling rates do not allow the solute atoms to diffuse or precipitate out during solidification (Taltavull et al. 2014) leading to the enrichment of Zn and Dy in the laser melted zone as shown in **Table 4.10**. The elemental composition determined using EDS shows that the concentration of alloying elements is different in the melt pool compared to that in the substrate region. In the substrate, the concentration of Dy is more in the eutectic structure present at the grain boundary than in the α-Mg matrix. The EDS analysis of LSM zone confirms that there is no loss of alloying elements in the melt pool region. Moreover, the concentration of Dy in the LSM zone is relatively high, compared to substrate region, and this could be due to rapid cooling rates induced supersaturation of the liquid metal and potential evaporation of Mg during laser melting (Guan et al. 2009) (**Table 4.10**)

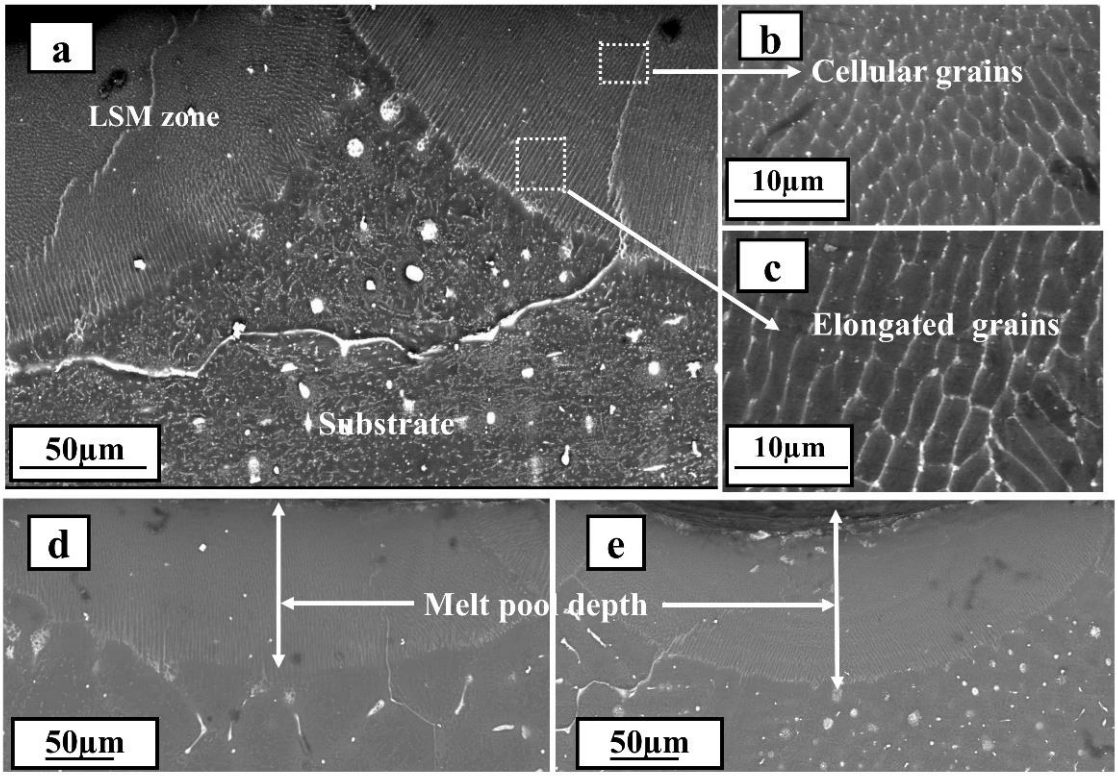

Figure 4.32 (a) Typical cross sectional microstructure of Mg-Zn-Dy alloy laser surface melted at 25 J/mm^2 (b) and (c) Enlarged view of microstructural changes in different regions, (d) and (e) Meltpool depth of the alloy processed at 25 J/mm^2 and 45 J/mm^2, respectively.

Table 4.10 EDS analysis of melt pool region and substrate (as cast) of Mg-Zn-Dy alloy

Alloy conditions (within the grain boundary)	**Mg**	**Zn**	**Dy**
	Weight percent		
As cast	93.5±3	2.1±2	3.2±4
12.5 J/mm^2	92.9±1	1.6±0.4	5.4±1
25 J/mm^2	91.2±2	2.2±1	6.2±2
45 J/mm^2	88.0±1	3.5±0.5	8.4±0.7

4.3.2 Phase analysis

Figure 4.33 shows XRD patterns of as-cast and LSM samples at different energy densities. Apart from major α- Mg phase, all samples showed secondary phases corresponding to Mg_7Zn_3 and Mg_8ZnDy. It is seen that all samples show a dominant sharp peaks at 2θ = 32.19°, 34.4° and 36.63° which are indexed to (100) (002) and (101) planes, respectively and correspond to α-Mg phase (JCPDF file no. 00-035-0821). It is also observed that the intensity of (101) peak increases with laser energy density while the intensity of other two dominant peaks (100) (002) gets reduced, which implies some preferred grain orientation along (101) in the LSM samples. The diffraction peaks at 2θ ranging from 40° to 80° show additional peaks related to the formation of secondary intermetallic phases (Mg_7Zn_3 and Mg_8ZnDy) (Guangli et al. 2016) (Zhang et al. 2014a) (Ho et al. 2015b). During laser melting, the concentration of Zn and Dy (**Table 4.10**) increased in the α-Mg matrix which leads to lattice parameters changes. The high concentration of these elements in the matrix is attributed to the loss of Mg due to evaporation and dissolution/disintegration in the concentration of intermetallic components in LSM samples (Liu et al. 2015). The enrichment of Zn and Dy causes changes in the lattice parameter which is observed in the XRD plot (**Figure 4.33)**. The diffraction peaks of lased melted samples gradually shift towards higher scattering angles due to decrease in lattice parameter of α-Mg phase.

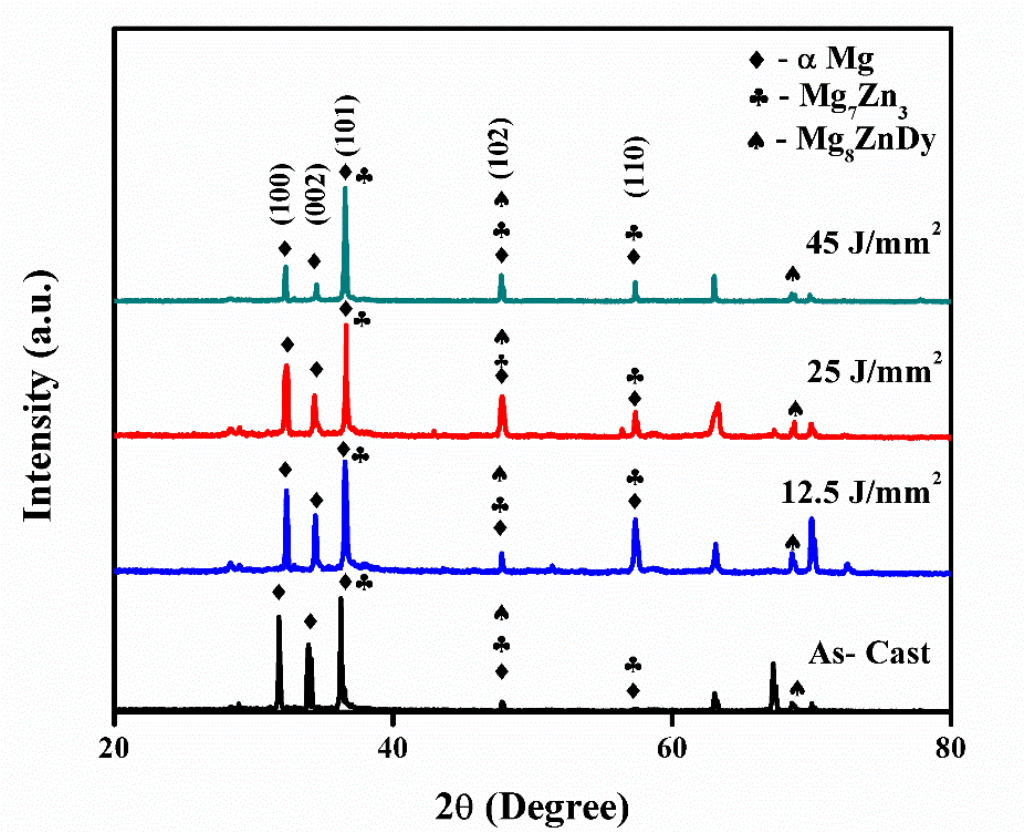

Figure 4.33 X-Ray diffraction analysis of different phases in as cast and laser melted Mg-Zn-Dy alloy

4.3.3 Microhardness distribution

The effect of LSM on the hardness of Mg-Zn-Dy alloy is presented in **Figure 4.34**. The range of average hardness of alloy samples varied from 73 HV for as cast to 94 HV for LSM samples. The improvement in the hardness of LSM samples is due to grain refinement and solid solution strengthening. When the laser energy was increased from 12.5 J/mm^2 to 35 J/mm^2 the hardness increased as a result of fine grains in the melt pool. Maximum hardness of 94 HV was observed at 175 W and 10 mm/s (35 J/mm^2) due to refined grains and dendritic region of the Mg-Zn-Dy structure.

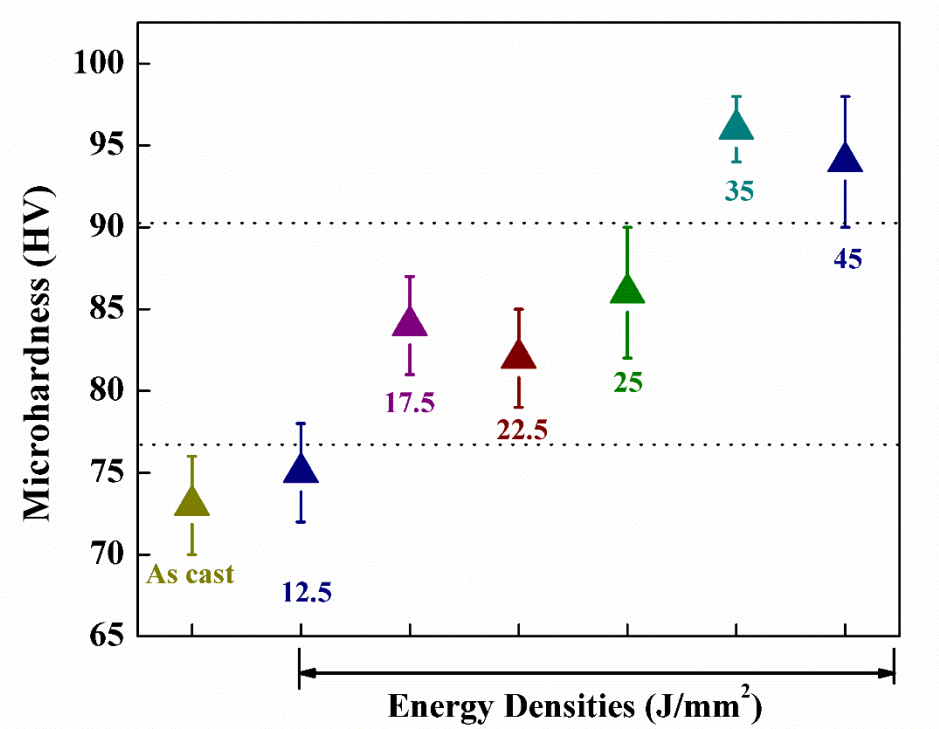

Figure 4.34 Microhardness distribution of as cast and LSM Mg-Zn-Dy alloy samples

4.3.4 Surface roughness analysis of LSM samples

The variation in the 3D surface roughness profile of LSM processed Mg-Zn-Dy alloy is shown in **Figure 4.35** and **Table 4.11**. The results of non-contact profiliometer showed increase in the surface roughness with increase in the laser power. Surface roughness parameter (Sq) of LSM samples varied between 3.9±0.3 µm to 9.2± 0.9 µm, when the laser energy density was increased from 12.5 to 45 J/mm^2. When the laser beam irradiates on the alloy surface, the part of the energy being received by the material leads to the melting and the extent of melting primarily depends on laser processing parameters and material properties. The high energy density condition create localized evaporation of the material. The evolved vapour from the melt zone (meltpool) creates a recoil pressure on the liquid melt zone. The consequence of recoil pressure is the generation of hydrodynamic melt motion and discharge of melt liquid towards the melt pool edges. Once the beam moves out from the interaction zone, the molten material solidifies quickly because of higher cooling rate and self-quenching effect. This repeated instant heating and cooling process leads to a noticeable surface topography at different laser processing conditions ((Semak and Matsunawa (1999),

Vora et al. (2013) and Ho et al. (2015a)). The increase in surface roughness with increase in laser power might be due to higher recoil pressure induced shock waves at the melt pool zone.

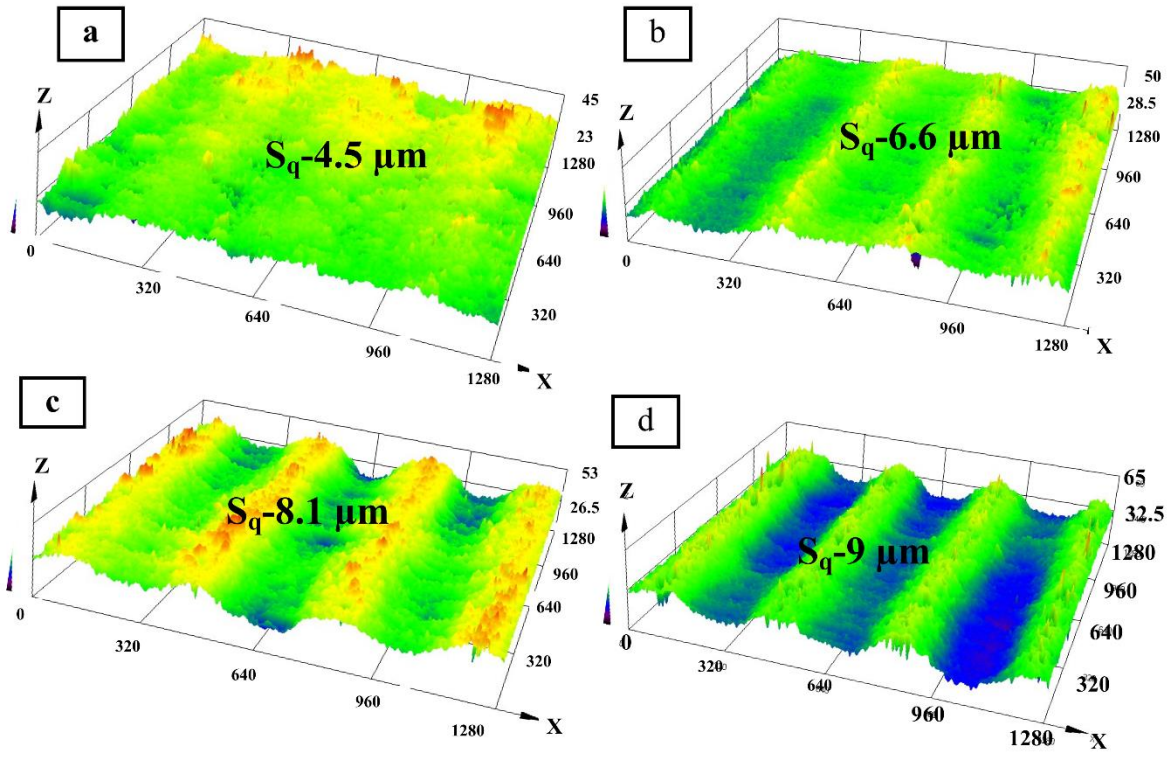

Figure 4.35 3D surface maps of LSM samples processed at (a) 12.5 J/mm^2 (b) 22.5 J/mm^2 (c) 35 J/mm^2 (d) 45 J/mm^2

Table 4.11 Surface roughness, surface energy and contact angles of laser melted and polished laser melted samples processed at different energy densities

Laser Energy density (J/mm^2)	**Surface roughness (Sq-µm)**	**Laser melted samples**		**Laser melted and polished samples**	
		Contact angle (˚)	Surface energy ($mN\cdot m^{-1}$)	Contact angle (˚)	Surface energy ($mN\cdot m^{-1}$)
As-cast		92±2	12±2	92±2	17±2
12.5	4.5±0.3	70±8	28±5	64±1	36±1
17.5	3.9±1	71±7	22± 3	65±2	34±3
22.5	6.6±0.2	74±2	21±3	72±2	32±2
25	7±0.3	77±7	19± 6	75±2	31±2
35	8.1±0.5	80±2	17±2	79±2	34±2
45	9.2±0.9	86±10	15±6	83±2	32±2

4.3.5 Wettability behaviour

Wetting behaviour of as cast and LSM samples before and after polishing were carried out using two different liquids and the surface energy of samples determined using contact angles are presented in **Table 4.11.** The effect of surface roughness and surface microstructure, and chemical composition on the wetting behaviour can be identified from the data of as processed and polished samples. Usually, contact angles less than 90° indicate favourable wetting by spreading the fluid over large surface area. The contact angle of the samples was determined in as-processed condition to assess the overall change in the wettability. The samples processed at different laser parameters showed different surface roughness, different microstructural features as well as some solute enrichment. Accordingly, the changes in the wettability of the sample in the laser melted samples are due to changes in their surface roughness, microstructure and composition during high energy laser melting. So in order to assess the influence of microstructural and composition changes on wettability the sample surfaces have been

polished. Polishing ensures similar roughness and then the contact angle has been assessed on these polished surfaces. The wettability of polished surfaces is expected to provide information on the influence of changes in the surface microstructure and composition on wettability. The results represented in **Table 4.11** exhibit notable changes in contact angle and surface energy. The recommended contact angle of biomedical implant is 70°. Hence, from **Table 4.11**, it can be seen that suitable hydrophilicity and surface energy obtained at energy densities of 22.5 and 25 J/mm^2. Compared to the grain size of as-cast alloy significant reduction has occurred in the grain size of LSM sample to the order of 2 µm which is 90 % less than the grain size of as cast alloy. The reduction in the average grain size with increasing energy density can be attributed to the increasing number of nucleation sites (Ho et al. 2015a). Further, this large grain boundary area with grains at different orientation changes the contact angle. These grains and grain boundaries could react to the DI water molecule differently. Consequently, smaller grains with large grain boundary area lead to heterogeneous chemical composition (Rosales-Leal et al. 2010). EDS analysis confirms that distribution of elements (Mg, Zn, and Dy) and chemical composition varies with different LSM processing parameters. The low wetting behaviour at higher energy density conditions is mainly due to the heterogeneous chemical composition of elements. Maximum surface energy of 36 mN/m at 12.5 J/mm^2 and a minimum of 31 mN/m at 25 J/mm^2 were observed for polished samples (**Table 4.11)**.

The laser melted samples, in as processed condition, showed superior wettability in terms of lower contact angles compared to as-cast alloy (**Table 4.11**). Further, the wettability appears to increase with laser energy density to an extent. The surface with lower contact angle shows better cell adhesion and it has been reported that better bone mineralization could be achieved with higher surface energy and lower contact angle (Ho et al. 2015b). As the value of contact angle increased from 64° to 83° in laser melted samples, the surface energy was found to be decreased from 28 mN· m^{-1} to 15 mN· m^{-1}. At lowest energy condition, surfaces are close to hydrophilic in nature and for the as cast alloy it is hydrophobic (92°) in nature and that can led to poor cell attachment. Further, the resulting surface energy of as cast alloy (12 mN·m^{-1}) was lower than laser processed samples. The surface topography generated on this alloy due to

laser melting is beneficial as it generally improves the cell adhesion and helps in osteointegration (Rosales-Leal et al. 2010). Suitable roughness at nano and micro-scales is a useful quantity that has been directly related to the wettability and surface energy (Zhu et al. 2004). Consequently, laser irradiated surface with hydrophilic nature presumably accelerated the wettability. The changes in the cooling rates and solidification rates at different energy densities corresponds to the changes in surface roughness (Ho et al. 2015a). As a result of laser processing, the surface roughness increased (Sq = 4.1 to 8.7 μm) with increasing energy density which eventually increased the surface energy from 12 to 28 $mN{\cdot}m^{-1}$. The less valleys and radial grooves at lower roughness (~ 4.5 μm) would impede the scattering of water droplet at the laser meted sample surfaces. Similarly, surfaces with more valleys and honed edges at higher surface roughness (8.7 μm) are no longer efficient of keep the water droplets at higher energy density conditions. Hence the samples exhibit higher apparent contact angle (83°) which is almost close to being hydrophobic in nature. Regarding the wettability of biomaterial surfaces, cells tends to attach and proliferate effectively on surfaces with contact angle of around 70° (Arima and Iwata 2007)(Wei et al. 2009). Therefore, present LSM samples show desirable degree of wettability and the results indicate that the surface roughness and related properties can be tailored by changing the laser processing parameters. The results showed that with respect to the nature of demand, the samples with roughness or without roughness can be considered for implant application.

4.3.6 *In-vitro* degradation-Immersion method

The degradation rate of laser melted Mg-Zn-Dy alloy and its kinetics were measured by weight loss, hydrogen evolution, magnesium ion (Mg^{2+}) release during the static immersion study in HBSS. All the laser melted as well as as-cast samples are fine polished to avoid the roughness effect on corrosion and maintained Sq value of ~1μm. The degradation rates of different samples are summarized and plotted in **Figure 4.39.** Better degradation correlation is made with laser energy density and it is represented in graph without the units for easy representation (eg. 12.5 J/mm^2 is represented as 12.5 on the graph). **Figure 4.36** shows the amount of hydrogen evolution trend measured at every 24 h of time. It is observed that the hydrogen evolution gradually increases in

trend up to 140 hours of immersion and later on it starts to decrease with increasing immersion time and similar kind of increasing trend has been observed in laser melted Mg-Zn-Gd alloy (Rakesh et al. 2018). The rate of degradation is rapid in as cast alloy compared to laser melted samples. Out of all processing conditions, low energy density (12.5 J/mm^2) processed sample shows higher hydrogen evolution during the immersion (maximum value 0.7ml/cm^2) time owing to the highest degradation rate. However, after a period of immersion (∼144 h) as cast and 12.5 J/mm^2 samples exhibits close matching in hydrogen evolution trace mainly attributed by stable passive film formation.

The lower corrosion resistance at 12.5 J/mm^2 and 25 J/mm^2 conditions are mainly due to the solidification crack during the laser melting process. It is seen that slopes of the curve (**Figure 4.36**) are higher during the initial period of immersion (∼ upto 96 h) which represent higher hydrogen evolution rate for as cast, 12.5 and 25 J/mm^2 samples, which is of order 0.004 ml/cm^2/h, 0.0042 ml/cm^2/h, 0.0038 ml/cm^2/h respectively. Further, lower hydrogen evolution rate of 0.002 ml/cm^2/h is observed for 45 J/mm^2 processed sample. The moderate amount of hydrogen evolution was observed for 35 J/mm^2 sample and during the initial period of immersion the slope of trace is steeper and at a later time (∼120 h) there is a drastic reduction which shows stable passive film formation. After 140 hours of immersion in HBSS the release of hydrogen evolution gradually retards mainly assisted by the insoluble protective layer formation. The volume of hydrogen released in the implanted magnesium alloys should be carefully monitored. If excess hydrogen gas evolves than the hydrogen absorption capacity of the tissues (which are surrounded to the implant area) this may cause detachment of tissues and gas embolism (Zhang et al. 2013c).

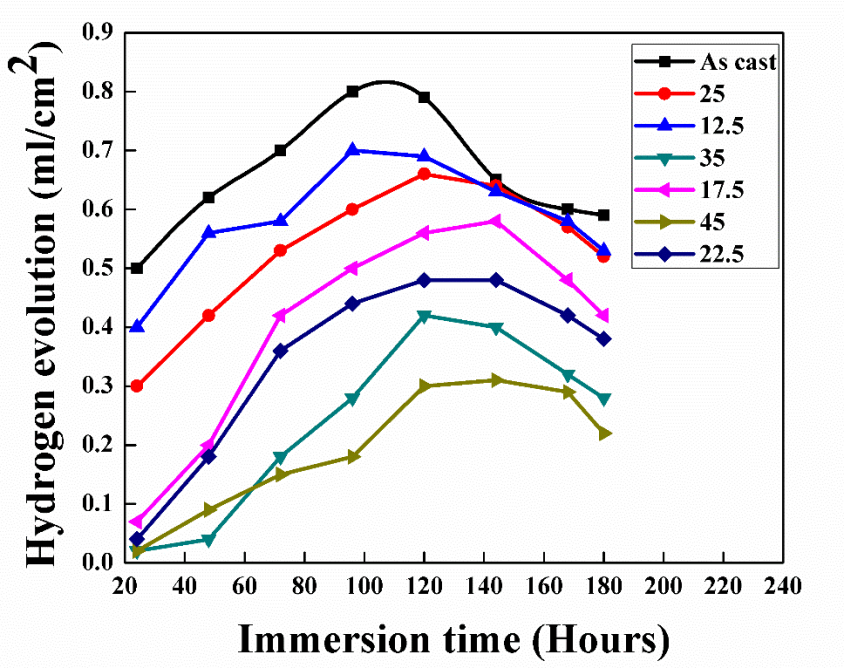

Figure 4.36 Hydrogen evolution extracted during the immersion study in HBSS

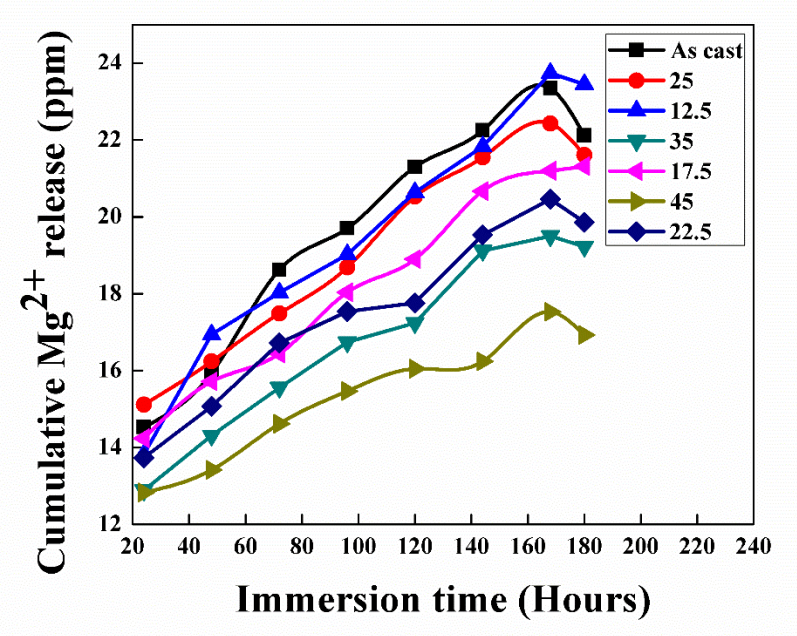

Figure 4.37 Mg^{2+} release extracted during the immersion study in HBSS.

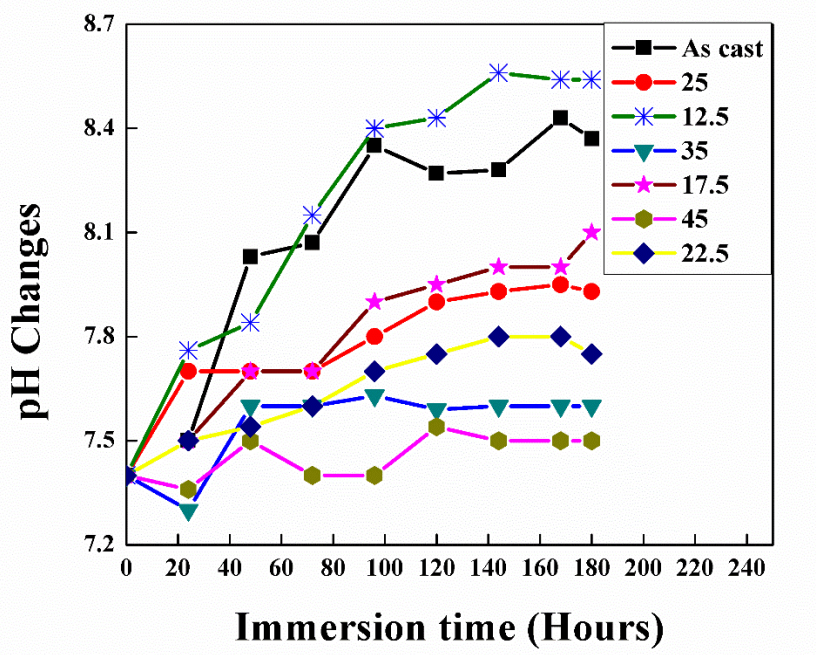

Figure 4.38 pH changes extracted during the immersion study in HBSS

The degradation process in HBSS solution is also complimented by the anodic reaction ($Mg \rightarrow Mg^{2+}+2e$) and the cumulative release of Mg^{2+} ion observed is represented in the **Figure 4.37.** With the increase in time of immersion, more of Mg^{2+} ions are dissolved into the solution. Studies reported that the release of Mg^{2+} retard the degradation because of magnesium containing precipitate ($Mg^{2+}+2OH^{-} \rightarrow Mg(OH)_2$) (Witte et al. 2007) formation on the surface of the samples. The observed ion release with respect to the immersion time are found to match with the hydrogen evolution trend (**Figure 4.36**). During the initial period of immersion (~100 h) higher anodic dissolution leads to sharp increment in the ion release promoting higher degradation. At higher energy density condition (45 J/mm^2), the maximum ion release is 17 ppm and which is found to be less than the as cast sample (23 ppm ion release). The maximum possible Mg^{2+} ion release observed among the laser processed samples is 23.7 ppm for 12.5 J/mm^2 and after 144 h of immersion it offers an increase in ion release trend than as cast sample. It was documented that magnesium in the orthopaedic implants could increase the sticking of osteoblastic cell (Zreiqat et al. 2002). Henceforth, magnesium could play a prominent role in the bone tissue growth. So in the present study the controlled release

of Mg^{2+} ion could have supported to the improved activity of osteoblast in the laser processed Mg-Zn-Dy alloy.

The human body pH is comparatively constant in between 7.35 and 7.45 (Woodrow 2004). Although there is possibility of pH fluctuation during the metabolic activity after implanting material and there by release of hydrogen ions. It is also evident that after bone implantation pH value at the fracture site reaches as low as 5.5 during the recovery period (Ng et al. 2010). So it is important to monitor change in pH during the immersion study to understand the mechanism of corrosion behaviour and bio-mineralization effectively for design of Mg based implants. **Figure 4.38** shows the change of the pH values of HBSS during the immersion study of samples. The typical increase in pH value was observed for all samples. The change in pH value (< 11) leads to anodic dissolution of Mg and cathodic reaction (hydrogen reduction and $(OH)^-$ release) (Pan et al. 2017). It can be observed from **Figure 4.38** that there is a sharp increase in the pH curve for as cast Mg-Zn-Dy and 12.5 J/mm^2 samples during the immersion of 180 hours. The value of pH starts to raise from 7.4 and reaches to 8.5 for 12.5 J/mm^2 owing to higher degradation rate. The samples processed at higher energy densities (35, 45 J/mm^2) show increase in pH during the initial period of immersion and become stable after 120 hours of immersion. The decreased corrosion rate due to the accumulation of corrosion product in a larger dimension occur at a pH of 7.4 and it became thicker in nature. EDS analysis (**Figure 4.42**) also shows that products formed on these surfaces are mainly hydroxides and with a part of phosphates. The volume of hydrogen, Mg^{2+} ion released are also found to be small at higher energy density conditions as determined by corrosion rates. The change in pH is moderate for samples processed at 17.5 and 25 J/mm^2 and it reaches a maximum pH of 8 during the immersion.

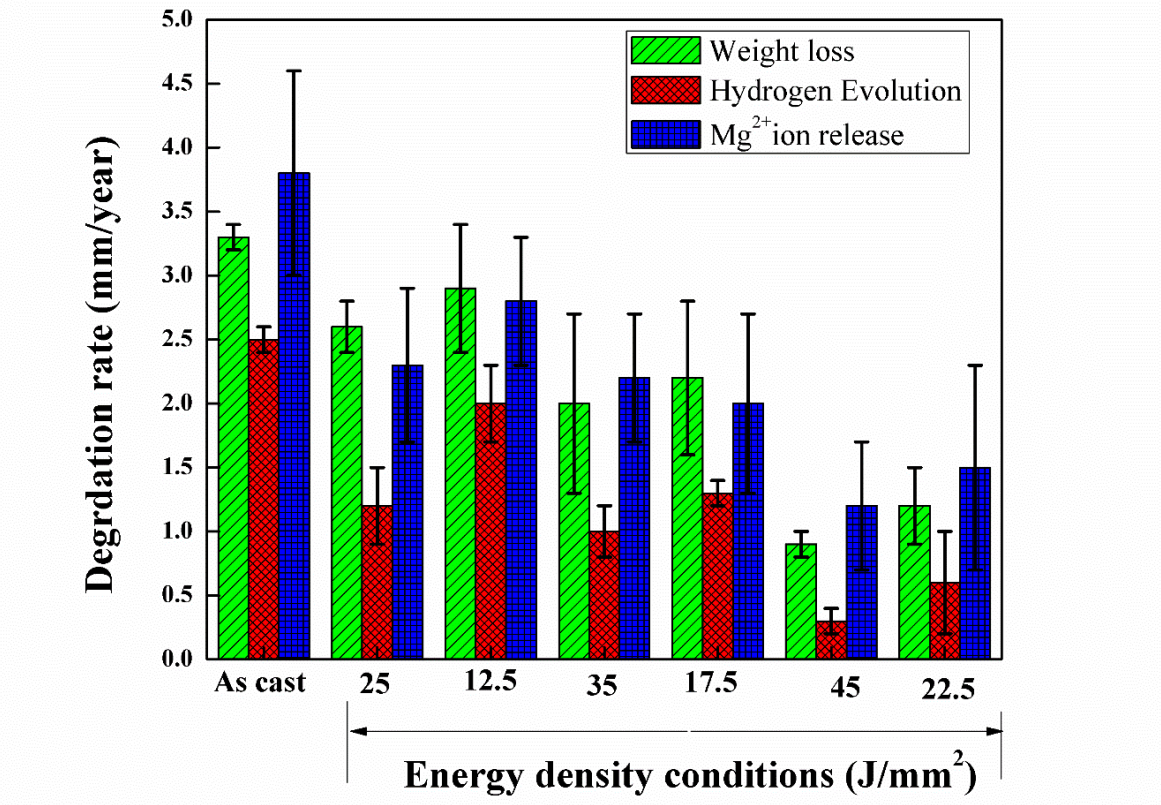

Figure 4.39 Measured degradation rate and it comparison after 180 hours of immersion in HBSS

The mass loss, hydrogen evolution and Mg^{2+} ion release rates are now reworked in terms of corrosion rate and are presented in **Figure 4.39**. The laser processed samples show a significant improvement in the *in-vitro* degradation rate at except lower energy density conditions for all three measurements. It was observed that there is a maximum of 72 % improvement of corrosion rate at 45 J/mm^2 laser processed sample as compared to as cast Mg-Zn-Dy alloy. The trends of the obtained degradation rates from three different ways of calculations are in agreement with each other. The samples processed at 12.5 J/mm^2 show higher degradation rate compared to other energy densities and as cast alloy mainly due to the formation of micro-crack at the meltpool and poor overlapping of successive meltpool (**Figure 4.40(d), Figure 4.40(e)**). These solidification cracks will further act as a corrosion site for corrosion propagation. The advancement of corrosion is also due to the corrosion potential between laser modified zone, HAZ and substrate. Moderate corrosion rate was observed for samples processed

at 35 J/mm^2 and 17.5 J/mm^2. The degradation of the as cast Mg-Zn-Dy can happen by the formation of galvanic couple between the secondary phases and α-mg matrix. Additionally, the distribution and amount of secondary phases and their morphology have great influences on degradation resistance (Song and Song 2007). The more finely and continuously distributed secondary phases in the laser melted region helps in improving the degradation resistance. Melting predominantly refines the grains and distribution of secondary phases along the grain boundary. This smaller magnitude of grain refinement leads to higher grain boundary area and thereby decrease the anode to cathode area ratio (Dutta Majumdar et al. 2003). In a similar way, in this study remelting of the secondary phases at higher laser energy densities (35 and 45 J/mm^2) lessen the galvanic corrosion induced by the potential difference between the matrix and secondary phases. As a result of that, occurrence of pitting corrosion is limited and more continuous passive film is formed. However, alloy treated with other lower energy conditions steadily react with the solution leading to pitting mode of corrosion and discontinuous corrosion layer. The higher energy density conditions offer a better *in-vitro* degradation resistance during 180 hours of immersion, but due to the lower meltpool depth as compared to other energy densities it is expected to have a lower prolongation of modified surface with the exposed solution.

4.3.7 Corrosion damage characterisation

The behaviour of degradation is now observed with cross sectional and surface SEM images. The formation of products and its features are studied by EDS and XRD analysis. **Figure 4.40** shows the cross section SEM morphology of the samples after 180 hours of immersion. Different magnification for the SEM images is considered for better understanding of corrosion mechanisms. For the as cast sample, (**Figure 4.40 (a)**) degradation followed by non-uniform distribution of secondary phases create a large area of pit with corrosion products and in some area it reaches a maximum depth of 2.3 µm. The surface of the as-cast sample in **Figure 4.41(a)** shows degradation is film form in nature. In contrast to that laser melted samples showed lower degradation depth except the samples processed at 12.5 J/mm^2. **Figure 4.40(b)** shows the samples with a pit of approximately 1.3 µm depth and 1.6 µm width, which is much higher than the pits formed in the other laser processed samples and slightly closer to as cast

samples. This higher rate of degradation observed mainly due to the solidification crack, which were clearly shown in **Figure 4.40 (b)** (marked with red colour) and enlarged at **Figure 4.40(d)**. However, in the case of 45 J/mm^2 the sample (**Figure 4.40(c)**) is less affected with damage and leaves shallow pits at the meltpool zone. **Figure 4.41** describes the surface damages of the samples after prolonged immersion. The degree of attack is considerably different in the as cast alloy samples. The corrosion reaction is assumed to be start with localised pits and grows deeper and spread widely over the surface. This mechanism of movement of corrosion similar to filiform corrosion (**Figure 4.41(a)**). It can be observed that visible pits in **Figure 4.41(b)** which are interconnected to the bulk material result into sizeable holes leading the laser track to slightly peel off from the surface. After prolonged immersion of samples in HBSS, localized pits are formed in the longitudinal direction in 17.5 J/mm^2 samples (along the laser track) (**Figure 4.41(c)**). At a later stage they progress to the nearest laser track. It can also be possible that due to the lower overlapping and coarse grain structure at the meltpool overlapping junction leads to constant pit formation (**Figure 4.41(c))**. At higher laser energy density conditions (35 J/mm^2 and 45 J/mm^2), the localised degradation diminishes significantly leaving a shallow pits (**Figure 4.40(c))** and less corrosion products by leaving more pronounced area of laser tracks (**Figure 4.41(d)**).

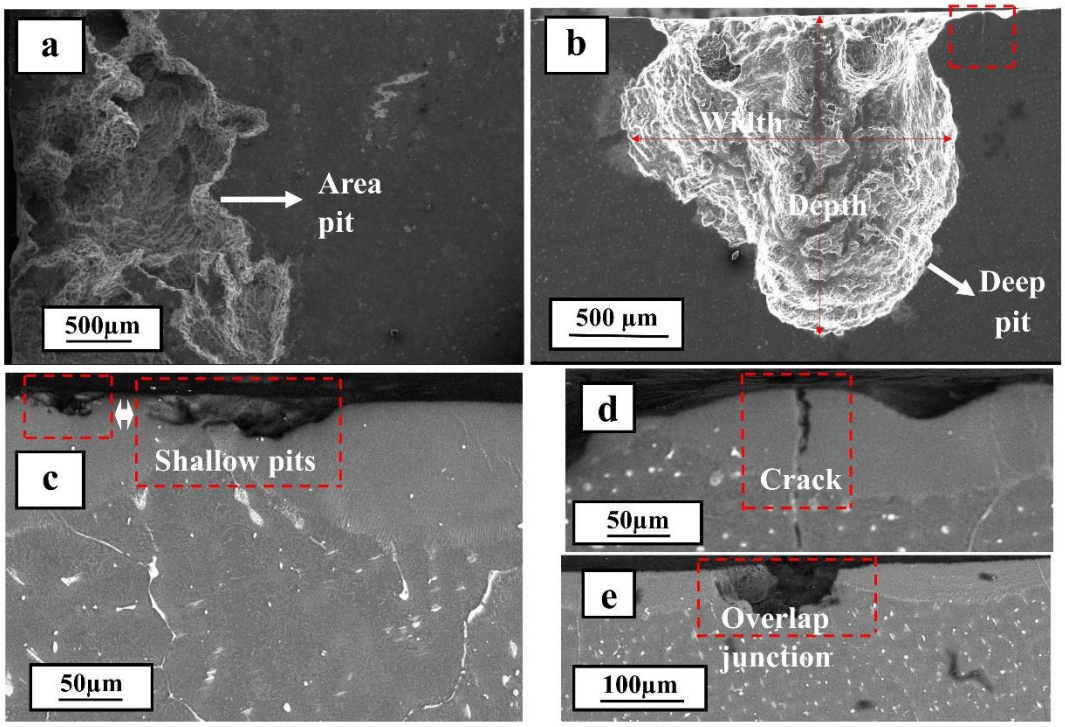

Figure 4.40 SEM image of cross sections of samples after 180 hours of immersion (a) as-cast sample (b) 12.5 J/mm^2 and (c) 45 J/mm^2 laser processed sample (d) Enlarged view of solidification crack (e) Pit at the overlapping zone

The corrosion products which were formed after the long term immersion of the samples were highly stable and were carefully scrapped off from the surface and studied in terms of bioactivity and corrosion resistance. The detailed analysis results are presented in the **Figure 4.43** . It was reported that (Li et al. 2008b) the necessary needs for a material to attach to living bone is the generation of bone like apatite once it is implanted in the body. So in vivo bone activity of new material can be evaluated by the apatite formation in HBSS. A discontinuous film formation with a large area of pit for as cast samples was observed. Although, in laser processed samples continuous film with smaller dimension of pits were observed. **Figure 4.43(a)** shows the surface product morphology on the surface of the laser treated sample. Initially the formation of magnesium hydroxide ($Mg(OH)_2$) precipitate at lower Mg^{2+} ion concentration (Johnston et al. 2015) (at higher energy density) permits the existence of stable passive film on the surface and this protective layer formation is confirmed by XRD analysis (**Figure 4.43)**. With increase in pH there is a swift nucleation of HAp with concurrent

formation of $Mg(OH)_2$. As the biodegradation proceeds the undissolved $Mg(OH)_2$ present on the surface of the alloy was also thought to bear feasible sites for nucleation of hydroxyapatite by consuming the calcium (Ca) and phosphate ions from the HBSS (Li et al. 2008b). The enlarged view (**Figure 4.43(a.1)**) indicates the dense cluster structure (rod like structure) (Yang et al. 2014) with calcium and phosphorus enriched areas similar to apatite formation. The XRD pattern of corrosion products showed a significant peaks of hydroxyapatite (HAp) at 2θ angle range from 18° to 70°, also showing that amount of formation of HAp is quite dominant on the surface of the sample. Immersion study also resulted in the formation of calcium phosphate and it is indexed at 2θ of 28°, 38° for 25 J/mm^2 and 22°, 59°, 61° for 35 J/mm^2 samples. The elemental composition and mapping was examined and results show that the surface is mainly distributed with good amount of Ca, O, P, Mg and lower amount of Na and K. The average Ca/P ratio at different locations of the surface product is 1.6 ± 2 which is very close to the stoichiometric ratio of Ca/P (1.67) (Yang et al. 2016) in HAp. The slight presence of carbon in the surface was due to the carbon dioxide dissolution (Yang et al. 2016). Further, the phase composition was analyzed by FTIR and major vibration bands are represented in **Figure 4.44**. The spectra of corrosion products agree with the results of XRD and SEM+EDS. The band at 3718 cm^{-1} represents OH^- and the same band which stretched out to 3386 cm^{-1} showing the evidence of apatite. Carbonate phases are represented by the presence of CO_3^{2-} band and is weak at 2351 cm^{-1} and strong at 1463 cm^{-1}. PO_4^{3-} band of smaller intensity at 569 cm^{-1} and sharp intensity band at 1049 cm^{-1} can be attributed to the presence of phosphate band (These peaks are also reported by Jebri et al. (2012) and Prekajski et al. (2016)). Spectra dominated with calcium phosphate and calcium carbonate precipitate which will help to hinder the corrosion attack to the surface (Aboudzadeh et al. 2018).

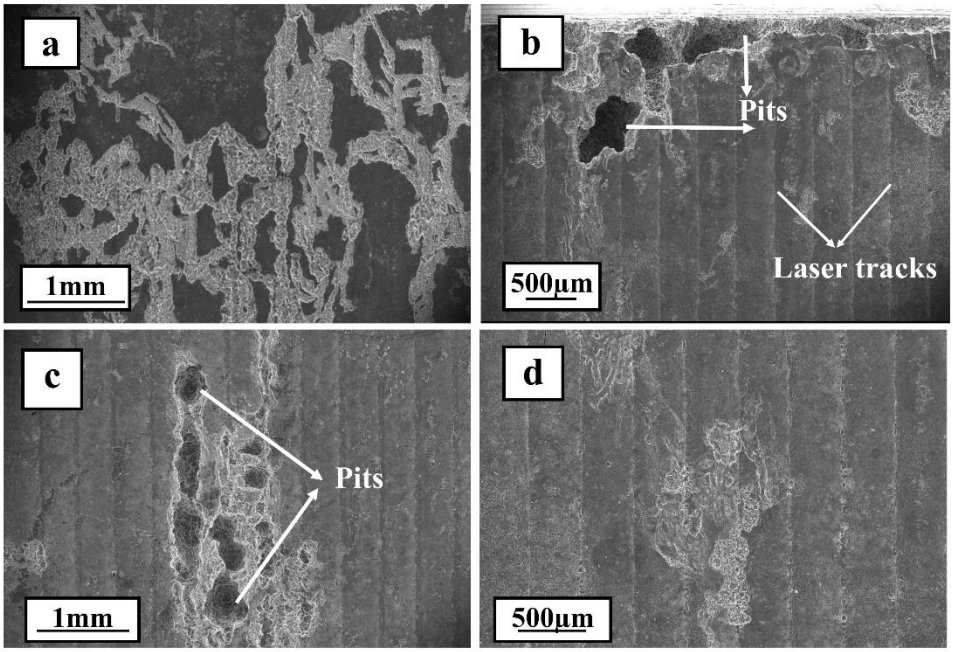

Figure 4.41 SEM images of surface after 180 hours of immersion (a) as cast alloy (b) 12.5 J/mm^2 (c) 17.5 J/mm^2 and (d) 35 J/mm^2 laser processed samples

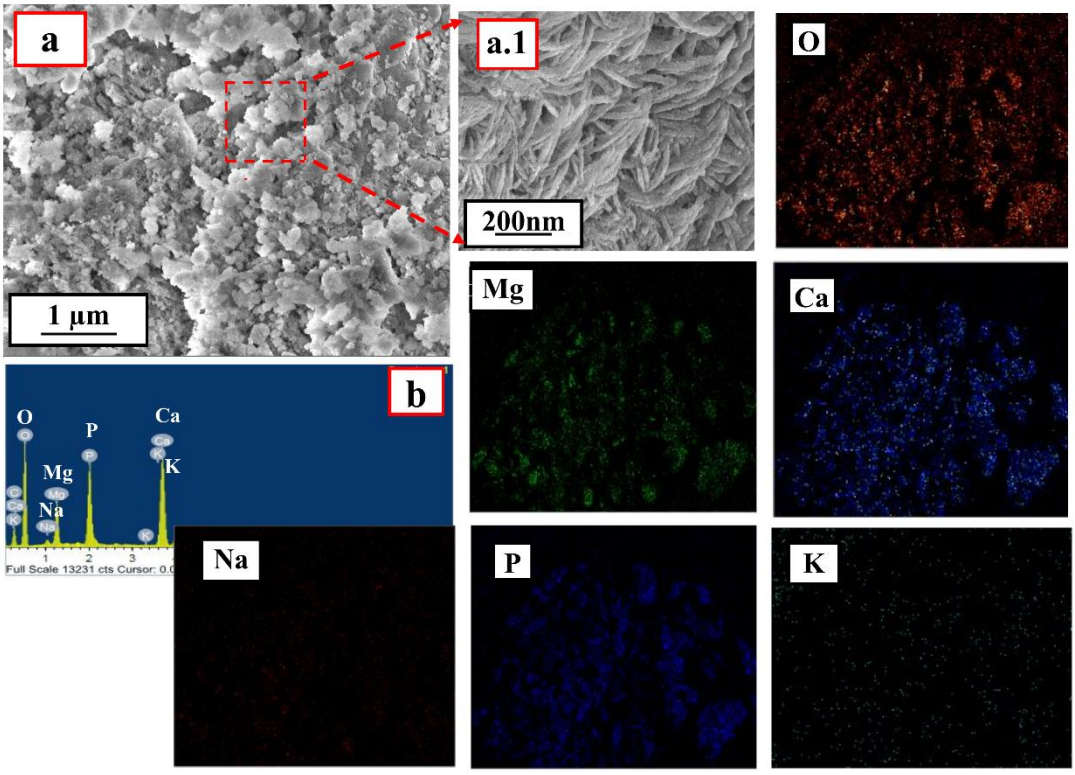

Figure 4.42 SEM+EDS mapping analysis of corrosion product after 180 hours of immersion in HBSS

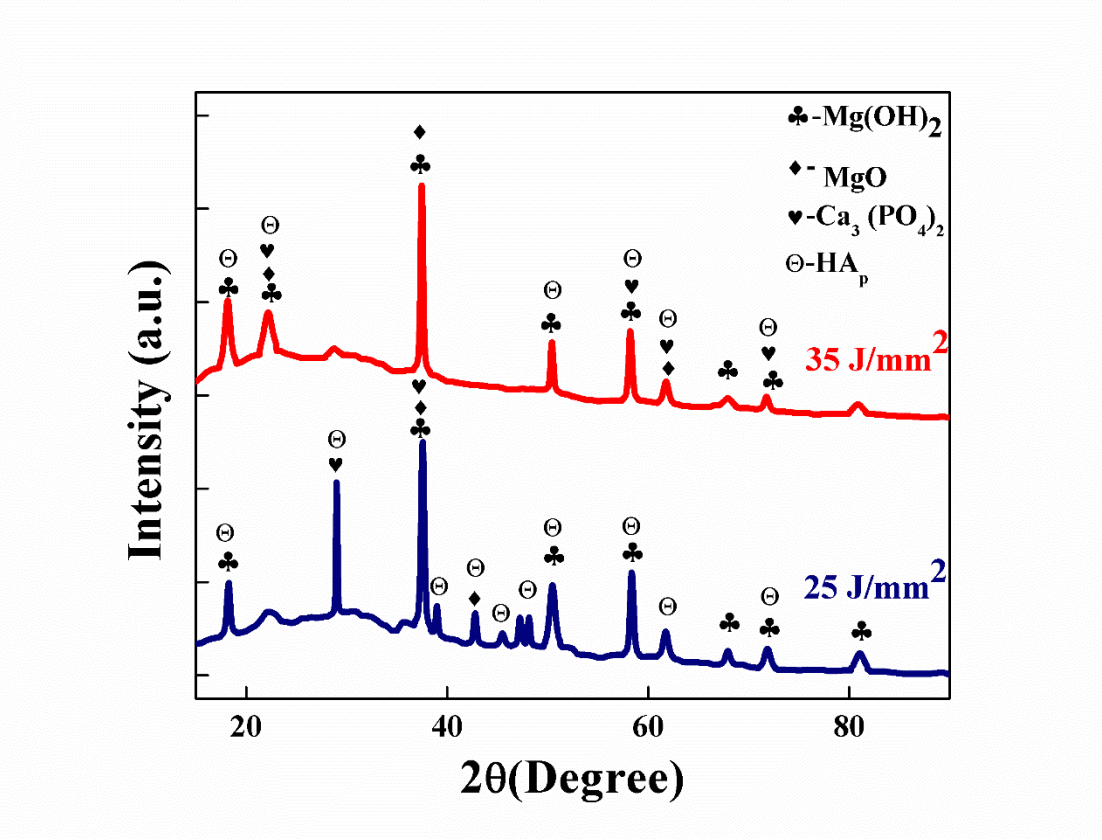

Figure 4.43 XRD analysis of corrosion product after 180 hours of immersion

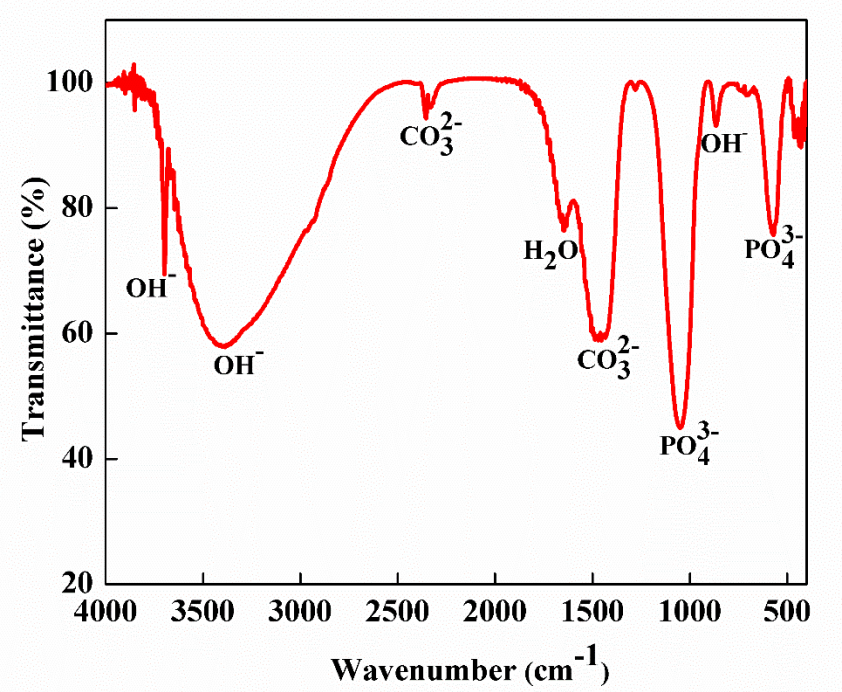

Figure 4.44 FTIR Spectra analysis of corrosion product extracted from corroded sample after 180 hours of immersion

4.3.8 Conclusions

The laser surface modification has been carried out on Mg-1Zn-2Dy (wt. %) alloy and following conclusions can be drawn.

- The increase in the laser energy density resulted in finer microstructures with high degree of homogenization and the depth of melted region increased from 98 µm to 150 µm.

- The wettability of the alloy was also improved due to LSM induced surface roughness, compositional and microstructural changes in the laser modified zones. Laser melting increased the surface roughness of the sample from 4 µm to 9 µm and enhanced the surface energy from 28 mN/m and 36 mN/m. The grain size reduction in the meltpool zone increases the area of grain boundary and homogeneity in chemical composition effectively improves the wettability.

- In vitro degradation shows 72% (weight loss method) improvement in laser melted sample at 45 J/mm^2 as compared to as cast alloy.

4.4 Studies on laser surface melted Mg-Zn-Gd-Nd alloy

This section discusses about the influence of laser surface melting on microstructure changes, hardness variation, wettability behaviour and degradation resistance of Mg-3Zn-1.5Gd-1.5Nd (wt. %) alloy.

4.4.1 Microstructural analysis

The preliminary investigation on microstructure of laser surface melted Mg-Zn-Gd-Nd alloy using TEM and SEM technique and the micrographs are shown and discussed here in first section **(4.1)** of the chapter 4. Cross sectional SEM morphology of LSM Mg-Zn-Gd-Nd alloy presented in **Figure 4.45**. After LSM, the large equiaxed grains changed to fine grain network at the localized regions where the laser irradiates. The laser modified zone referred to as meltpool and here there is a transition occurs in the grain morphology from top to bottom. According to the variation in the input energy density the depth of the meltpool changes and a maximum depth of 152 µm was observed at an energy density of 17.5 J/mm^2. A minimum depth of 102 µm was observed for the sample processed at 12.5 J/mm^2. **Figure 4.46** shows the meltpool depth variations as a function of laser power, and velocity (also as laser energy density). The variation in the meltpool dimensions can be attributed to the variations associated with the rapid cooling rates at different energy densities. The melt pool depth generally increases with increase in laser power generally but LSM of Mg-Zn-Gd-Nd at 17.5 J/mm^2 contradicts this general trend. By increasing the scan velocity and keeping the power constant the meltpool depth decreases. The meltpool depth observed was insensitive to the scan velocity at intermediate laser power 175 W. The depth of the meltpool has an influence on the corrosion propagation from the surface to substrate and thereby reducing the degradation rate (Rakesh et al. 2018).

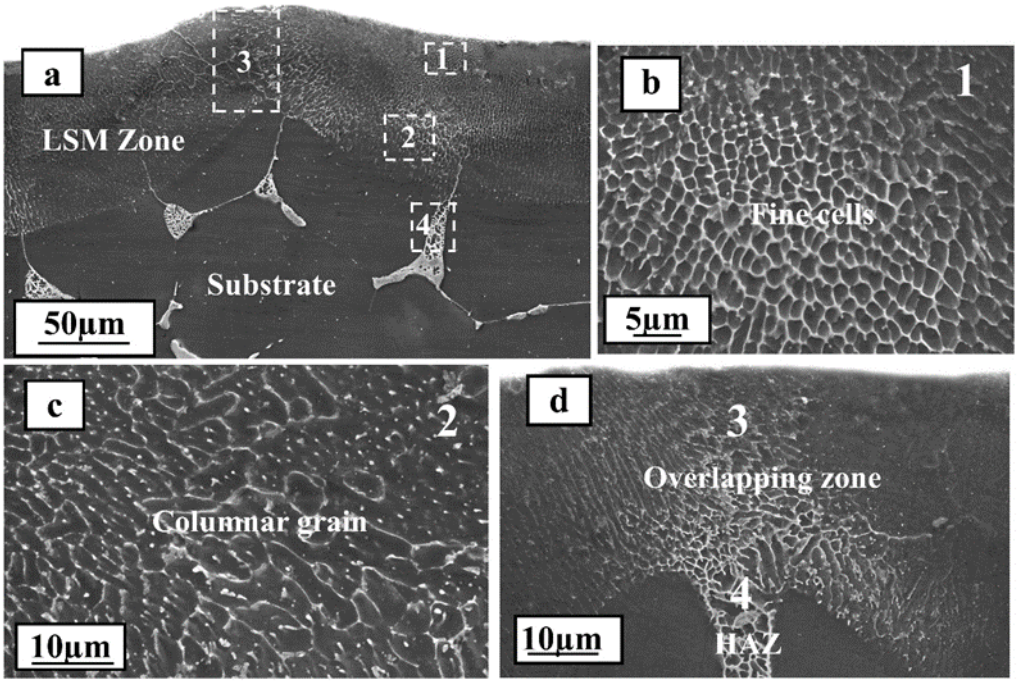

Figure 4.45 Cross sectional SEM morphology (a) LSM modified zone and substrate (b) fine cells in the meltpool (marked 1) (c) columnar grain in the meltpool (marked 2) and (d) overlapping zone and HAZ (marked 3,4 in the meltpool)

Irrespective of the laser energy densities the refinement of grains has happened almost uniformly for all the samples**. Figure 4.45** shows the transformation of microstructure at the meltpool zone. In the region marked in the **Figure 4.45(a)** there was complete melting which give rise to fine grain structure (**Figure 4.45(b**)) with homogenous phase distribution. The observed grain size of these fine cells are in the range of 1-2 µm, which is of about ~98% less than that of as-cast grain size. In region marked 2 in **Figure 4.45(a),** which is below regional columnar grains were observed. This region with partial transformation of microstructure at the substrate is termed as heat affected zone (HAZ) (marked 4 in **Figure 4.45 (d)**). Successive overlapping regions of the melt pools also refined significantly and the secondary phases are distributed uniformly in the grain boundary areas.

Power (W)	Velocity (mm/s)	Energy density (J/mm^2)	Meltpool geometry (µm)
125	10	25	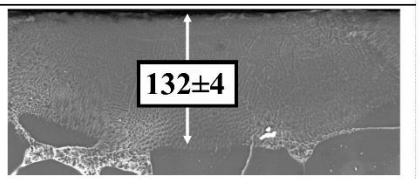
125	20	12.5	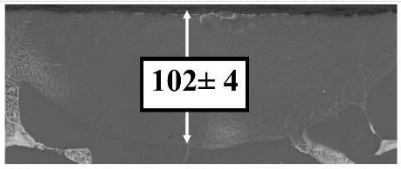
175`	10	35	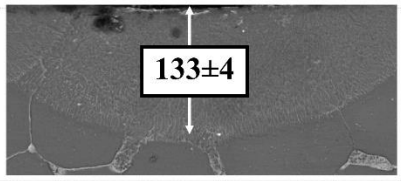
175	20	17.5	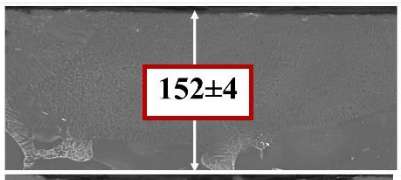
225	10	45	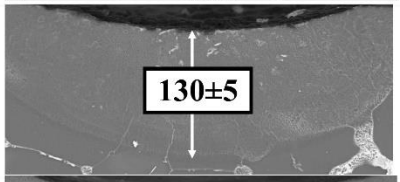
225	20	22.5	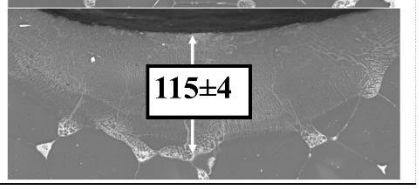

Figure 4.46 Laser processing parameters and meltpool depth variations

The compositional analysis by EDS in the meltpool shows that as the laser energy density increases the enriching of alloying elements (Gd, Nd and Zn) is better improved with in the α-Mg boundary. **Table 4.12** shows the quantitative elemental distribution analysis results. The formation and distribution of secondary phases is less likely to happen during casting because of the lower temperature. When the laser beam irradiates, the temperature rapidly increases up to above the melting point of α- phase. Under this molten condition the alloying elements start to diffuse into the matrix and the final composition is enriched primarily with Gd and Nd. So the microstructure

obtained after laser melting differs in elemental distribution because of the induced temperature at the molten zone at different energy density conditions.

Table 4.12 EDS analysis of meltpool region

Conditions (Within the grain boundary)	Mg	Zn	Gd	Nd
	Weight percentage (wt. %)			
Mg-Zn-Gd-Nd cast	97.3±1	0.2±6	1±7	0.6±6
12.5 J/mm^2	94.8±5	4±3	0.11±4	0.88±5
25 J/mm^2	88.8±6	4.2±5	4.9±5	1.3±6
45 J/mm^2	85.8±	5.8±4	6.2±5	2.2±4

4.4.2 Phase analysis

XRD patterns of as- cast and LSM samples of Mg-Zn-Gd-Nd alloy are shown in **Figure 4.47**. XRD patterns exhibited strong diffraction peaks at 32.19°, 34.4° and 36.63° indicating α-Mg phase. It is observed that the preferred orientation of the (101) plane was decreased with laser melting. The diffraction peaks from 2θ = 40° to 80° shows additional peaks with different relative intensities which strongly depend on the formation of secondary intermetallic phases (Mg_7Zn_3 and $Mg_{12}Nd$) (JCPDS reference code 03-065-2226 and 00-017-0401) due to rapid melting and solidification. Effective grain refinement was observed in the LSM samples and it is observed in the cross sectional SEM images (**Figure 4.45**). Debye-Scherrer's formula (Ozdemir and Karahan 2015) was also used to understand the variations in the grain size of as-cast and LSM samples from the XRD spectra.

$$\mathbf{D = \frac{0.9\lambda}{\beta\cos\theta}} \qquad \textbf{(4-5)}$$

In this formula, 'D' is the grain size, 'β' is the full width half maxima (FWHM) of the film at (101) plane and 'θ' is the Bragg's angle and λ is the incident ray wavelength that is considered to be 0.154 nm for Cu-Kα radiation.

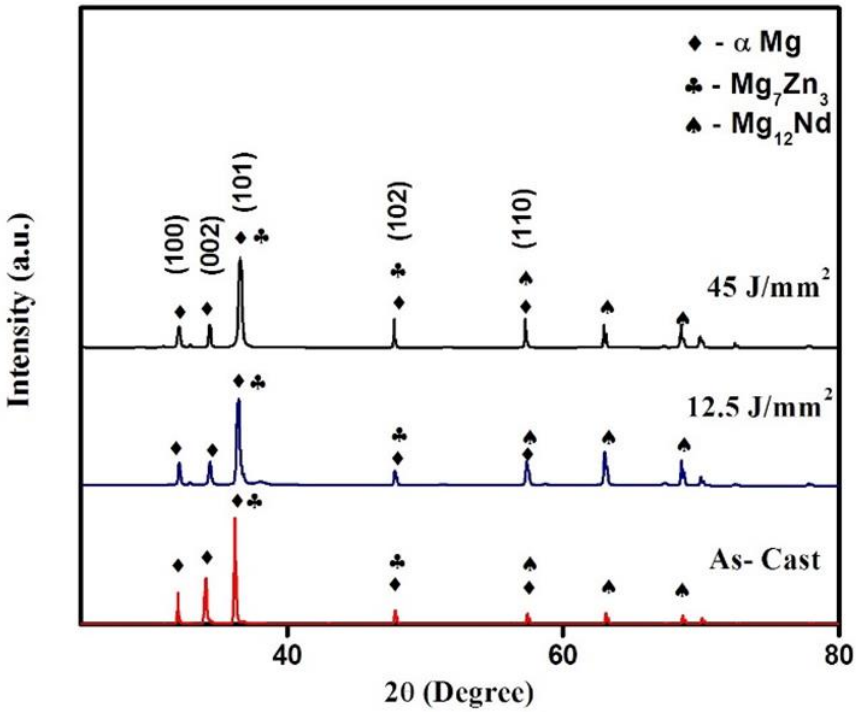

Figure 4.47 Phase analysis of as cast and LSM Mg-Zn-Gd-Nd alloy

The calculated values are tabulated in **Table 4.13**. The grain size is observed to decrease with increasing laser energy density which implies peak broadening and lowering the peak intensity. This grain refinement can be explained by rapid heating and cooling rates during LSM (Dutta et al. 2018). The enrichment of Zn and Nd (**Table 4.13**) in the α-Mg matrix due to the Mg evaporation and dissolution of intermetallic components is responsible for the change in lattice constant during laser melting (Ho et al. 2015a). The decrease in lattice constant of α-Mg phase results in a slight right shifting in diffraction peaks of laser melted samples (Liu et al. 2015).

Table 4.13 FWHM and grain size of the as-cast and LSM samples

Energy density	FWHM (°)	Grain size (nm)
As- cast	0.0960	87
12.5 J/mm^2	0.1771	47.2
45 J/mm^2	0.3050	27.42

4.4.3 Microhardness distribution

Figure 4.48 shows the hardness distribution of the as cast and LSM samples. The results reveal that there is a significant improvement (~1.3 times) in the hardness after LSM. Sample processed at 35 J/mm^2 exhibits a maximum hardness of 98 HV. There is an obvious grain refinement in the order of 2 µm was observed in the LSM samples at higher cooling rate condition. This grain refinement and uniform distribution of hardening of phases at the distinct location leads to the improved hardness mainly at 35 J/mm^2. For better understanding indentation points in the samples are represented in **Figure 4.48**. The average hardness distribution is in the range of 85 HV to 90 HV for samples processed at intermediate energy densities (17.5 J/mm^2, 22.5 J/mm^2 and 25 J/mm^2). Increasing energy density acts towards further reduction in grain size and that is attributed to the increase in hardness. The reduction in hardness at 45 J/mm^2 may be attributed to the changes in grain size and rapid cooling increase in the scan velocity. Furthermore, the change in the scale of solidification rate remarkably influences the grain coarsening at 45 J/mm^2 compared to 35 J/mm^2 . This cause the reduction in surface hardness (Balla et al. 2013) (Dutta et al. 2018) at 45 J/mm^2.

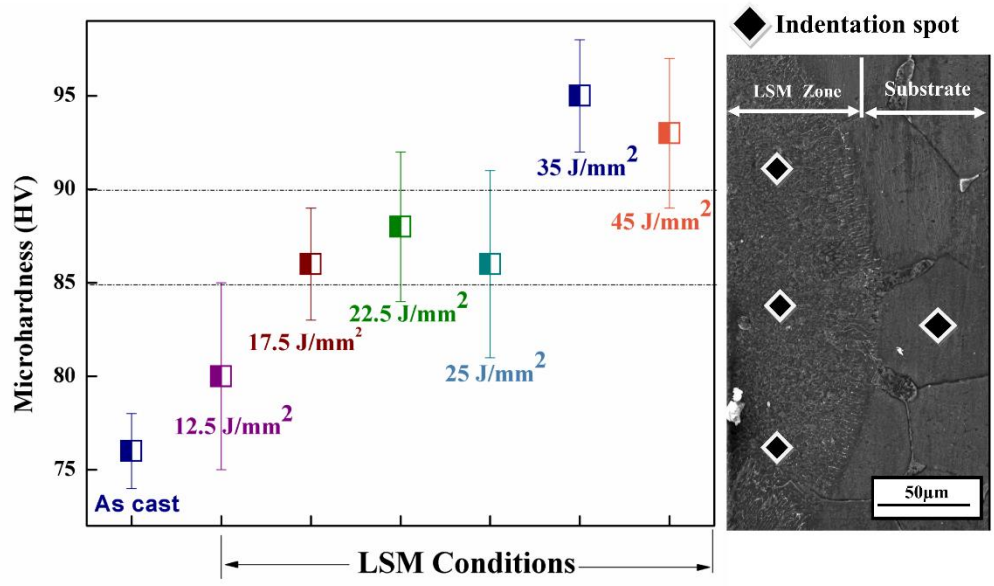

Figure 4.48 Micro hardness distribution and the cross sectional indentation spots in the samples

4.4.4 Surface roughness analysis of LSM samples

Surface roughness is a key parameter to be monitored to control the surface wettability of the material after LSM. S_q, average surface roughness is the main parameter measured for topography characterization and is represented in **Table 4.14**. Results indicate that increase in the energy density increase the surface roughness from 3.3 µm to 16.8 µm. Higher roughness values were observed in samples processed at higher energy densities especially at 35 and 45 J/mm^2.The intermediate energy densities such as 17.5 and 22.5 J/mm^2 did not show much variation in S_q value as it is affected with relatively similar hydrodynamic melt pressure. The measured surface topographical changes are mainly caused by the physics of hydrodynamic meltpool, recoil pressure and surface tension effects (Vora et al. 2012). The absorbed laser energy varies in accordance with the applied beam energy to the surface. The changes in the beam energy is attributed to the heating, melting and vaporization of the metal surface. The evaporation of the vapour particle from the laser material interaction zone tries to condense back to the meltpool by inducing a recoil pressure (Vora et al. 2013). This shock wave causes the ejection of liquid by hydrodynamic melt pool motion towards the edges of the meltpool. Further, the tangential stress exerted at the liquid crown due to the surface tension leaves a pronounced surface topography (Ho et al. 2015a). The shift in the applied energy density from lower to higher can be attributed to the changes in the cooling rate which also influences the instantaneous material solidification at the meltpool zone. The higher energy density conditions (35 and 45 J/mm^2) are effected with this higher magnitude of recoil pressure which results in higher surface roughness such as (15.8 and 16.8 µm). The profile of the surface has significant influence on contact and adhesion of the cells once the material is in the in vivo condition.

Table 4.14 Surface energy and surface roughness results of LSM and LSM polished samples

	Laser melted samples		**Laser melted and polished samples**	
Conditions	Surface roughness (S_q)	Surface energy (mN/m)	Surface roughness (S_q)	Surface energy (mN/m)
As-cast	1±2	10±5	1±2	10±5
12.5 J/mm^2	3.3±1	36.1±2	0.88±0.1	37.5±7
17.5 J/mm^2	6.3±1	19.8±3	1.14±0.5	37.5±7
22.5 J/mm^2	7±2	21.9±5	1.58±0.8	35.7±5
25 J/mm^2	9.4±0.5	17.9±8	1.04±0.3	36.6±6
35 J/mm^2	15.8±1	17.3±3	1.47±0.5	35.7±2
45 J/mm^2	16.8±2	13.5±4	1.6±6	33.7±4

4.4.5 Wettability behaviour of LSM samples

Static sessile drop method, is used to analyse the wettability of as-cast and LSM samples. This was carried out using DI water. The contact angle on different laser melted surfaces are shown in **Figure 4.49.** The wetting ability of LSM samples are direct reflection of surface energy, surface roughness, chemical composition and grain size (Ho et al. 2015a). But, it is difficult to explain which factor plays predominant role on surface wettability. There is a quantitative way to correlate the surface energy with contact angle and surface roughness (**Table 4.14** and **Figure 4.49**). At lower energy densities (12.5 J/mm^2- 25 J/mm^2), the change in melting and vaporization rate aids in decreasing surface energy from 36.1±2 mN/m to 17.9 mN/m corresponding to increase

in contact angle from 72.2±9° to 85.5±7°, indicating hydrophilic nature. It is found that the surface energy of LSM alloys decreases consistently and reaches a value of 17.3±3 mN/m, when the contact angle was noticed to be high (113.2±8 °). The water wetting behaviour of sample surface turn towards hydrophobic at an energy density of 35 J/mm^2. Notably, the varying surface energy alters surface roughness profile; a smoother surface could maximize surface energy (Zhu et al. 2004). The surface roughness (Sq) increased gradually from 6.3±1 µm to 16.8±2 µm with laser energy density. In the surfaces prepared at higher energy densities, water droplets sits on the surface with deeper valleys and taller peaks due to laser melting leads to reduction in wetting (Rosales-Leal et al. 2010).

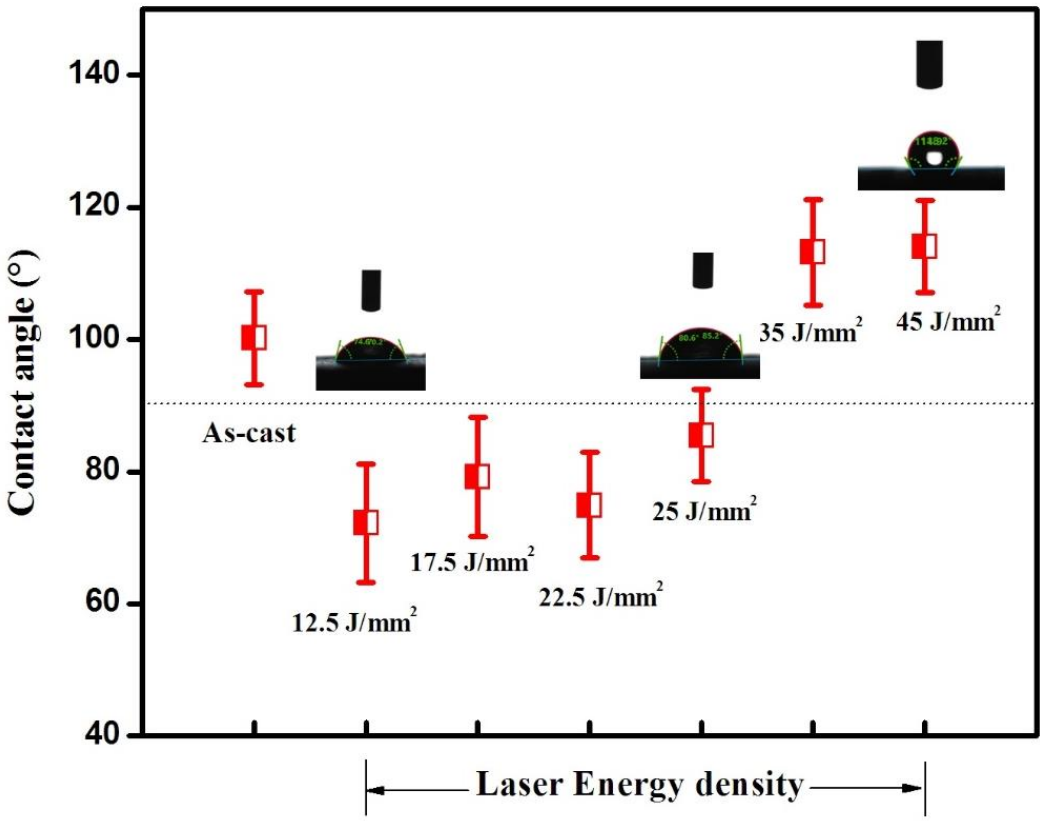

Figure 4.49 Contact angle variation in LSM samples with respect to the energy density and as cast conditions

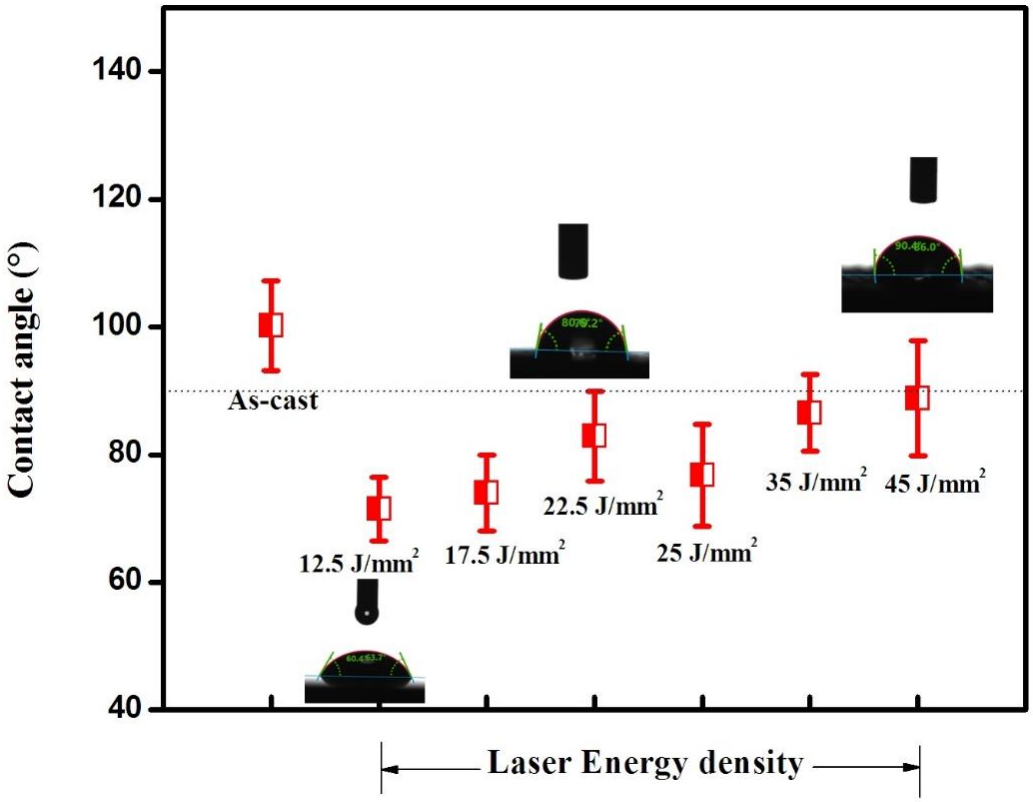

Figure 4.50 Contact angle variation in polished LSM samples with respect to the energy density and as cast conditions

In addition, grain refinement also played a key role on the wettability of LSM samples (Ho et al. 2015a). The variation in contact angle of polished LSM sample with respect to the energy densities is as shown in **Figure 4.50**. This grain size reduction is due to increase in nucleation sites with LSM. The dependence of grain size has been explained in terms of chemical composition (Mg, Zn, Gd and Nd) observed in grain and grain boundaries by EDS analysis (**Table 4.12**). Hence, the grain-grain boundary reactions towards water drop are different (Rakesh et al. 2018) (Lincks et al. 2006). A uniform chemical composition obtained at lower energy density condition, yields effective wetting due to larger grain size and smaller grain boundaries. The poor wetting behaviour of the LSM polished samples is influenced by very fine grain size with non-uniform chemical compositions at higher laser energy densities (Ho et al. 2015b).

In order to study the feasibility of using LSM sample surface with minimum roughness in implant application , the deeper valleys and taller peaks are smoothened out from

LSM samples with polishing and thereby attaining uniform surface roughness (~ Sq = 1 µm) to understand the wetting behaviour. The surface energy and contact angle data for polished surfaces followed the same trend as unpolished surfaces. The reason for the trends shown by unpolished surfaces has been explained above. LSM polished samples show better wettability than LSM samples for implant applications.

4.4.6 *In-vitro* degradation-Immersion method

The degradation behavior of as cast and LSM Mg-Zn-Gd-Nd alloy were studied by static immersion methods and the results are discussed here. Mg and its alloys undergo dissolution primarily by the production of Mg^{2+} (anodic partial reaction) and hydrogen gas evolution (cathodic partial reaction) (Thomas et al. 2015). So the effective understanding of degradation behavior is assessed through hydrogen evolution, Mg^{2+} ion release and weight loss methods during and after the immersion of samples in HBSS.

Figure 4.51 represents the hydrogen evolution trace. From the figure it is evident that the trend is changing with the immersion time. It is observed that the initial release of hydrogen is linear to the immersion time and this shows drastic shift in the corrosion trend. The maximum hydrogen evolution is observed for as cast (without LSM) and 12.5 J/mm^2 LSM processed samples. The lower release of hydrogen is mainly observed for higher energy density processed samples (35 and 45 J/mm^2). The initial slope of the hydrogen evolution trace versus time was measured and it is enlarged and represented in the **Figure 4.51 (a.1).** The larger slope value of 0.014 ml/cm^2/h was observed for as cast and 12.5 J/mm^2 during the period of ~80 hours of immersion. During this period, the maximum amount of hydrogen production varies between 0.83 ml/cm^2 and 0.7 ml/cm^2 for as cast and 12.5 J/mm^2 sample. The minimum slope value of 0.003 ml/cm^2/h was observed at 45 J/mm^2 and maximum hydrogen release rate of 0.29 ml/cm^2 which is very less than the maximum values of other samples. The intermediate slope values of 0.01 ml/cm^2/h, 0.006 ml/cm^2/h and 0.005 ml/cm^2/h were observed for 17.5 J/mm^2, 22.5 J/mm^2 and 25 J/mm^2. The amount of hydrogen evolved for LSM samples at higher energy density conditions was significantly lower than untreated as cast sample for entire period of immersion studies, owing to relatively good in *in-vitro* degradation

resistance. The traces are becoming almost in stable condition (especially for 45, 35, 22.5 J/mm^2 samples) after 100 hours of immersion indicating the passive film formation. At higher energy density processed samples (45, 35 and 25 J/mm^2) the H_2 evolution trends are even decreasing during the last hours of immersion suggesting to existence of stable products on the surfaces. The final corrosion rate calculated from the hydrogen evolution is represented in the **Figure 4.53.** Among all samples, LSM sample processed at 45 J/mm^2 showed a lower corrosion rate which is also indicated by a lower hydrogen production trend.

The evolution of Mg^{2+} ion during the immersion of 180 hours is shown in **Figure 4.52 (b)**. As observed with the hydrogen production, the Mg^{2+} release also linearly varied with immersion time. The slope of the Mg^{2+} release versus time curve enlarged at different time intervals (~20-80 and ~ 90-140) to understand the increment in the ion release appropriately and are represented in **Figure 4.52 (a.1), (a.2).** During the initial period (**Figure 4.52 (a.1)**) the release of ions are drastic and maximum slope of 0.08 ppm/h and 0.06 ppm/h were observed for as cast and 12.5 J/mm^2 samples. Similarly, these samples showed maximum release of Mg^{2+} of 24.5 ppm and 24 ppm for 12.5 J/mm^2 and as cast samples. During the initial period of immersion as cast samples showed a higher Mg^{2+} release but nearly after 120 hours the 12.5 J/mm^2 sample trace was over crossed the as cast sample trace and leaving a higher slope of 0.16 ppm/h for 12.5 J/mm^2 compared to as cast sample (0.12 ppm/h). The minimum concentration of Mg^{2+} in HBSS was observed to be 13.9 ppm which is less (almost 43 %) than that of as cast sample. During the period of ~90-140 h (**Figure 4.52 (a.2**)) there is a sharp increase in slope as compared to the initial stages of immersion. The abrupt changes in the ion release could be due to the local destruction of passive film. At the same period, the slope at the higher energy density conditions were almost similar in magnitude and it is of 0.047 ppm/h for 35 J/mm^2, 0.45 ppm/h for 45 J/mm^2. The slope 0.16 ppm/h was observed at 12.5 J/mm^2 . This is found to be maximum calculated slope from the **Figure 4.52 (a.2**). The fluctuations in the trend at 12.5 J/mm^2 is mainly due to the defects caused due to the low energy melting of the alloy. The trend of the Mg^{2+} ion getting stabilized after 140 h of immersion is noticed mainly for 17.5 J/mm^2, 22.5 J/mm^2 and 35 J/mm^2 energy densities. There is a small decrement in ion release at the same time

for the 45 J/mm^2 and 25 J/mm^2 samples. The corrosion rate calculated from the Mg^{2+} release is also represented in **Figure 4.53.**

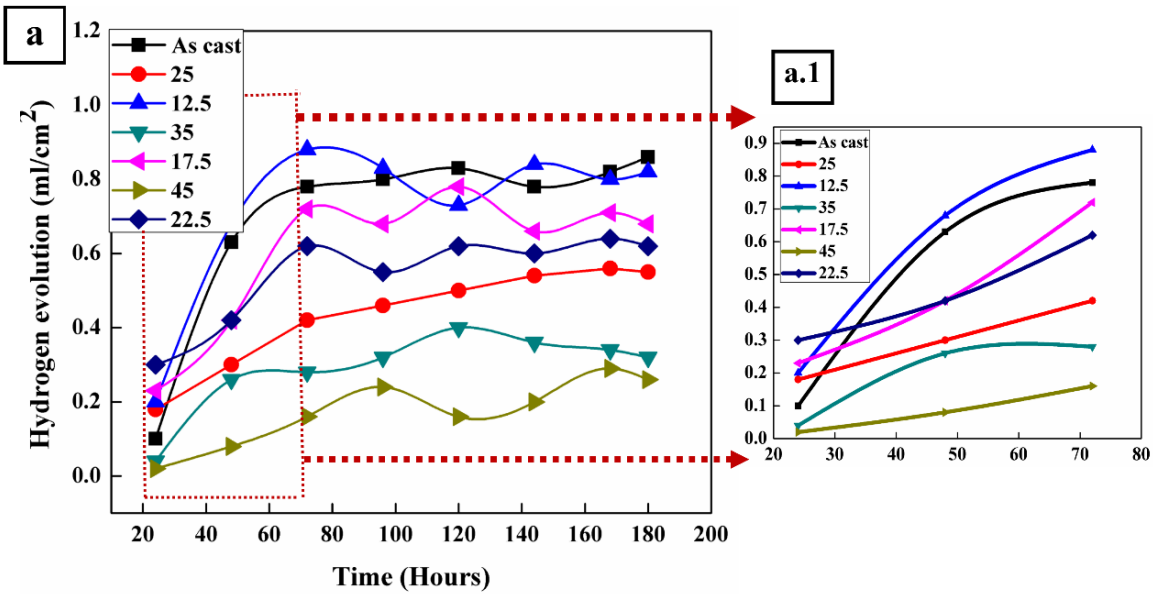

Figure 4.51 (a) The hydrogen evolution trend (a.1) enlarged view as a function of immersion time in HBSS

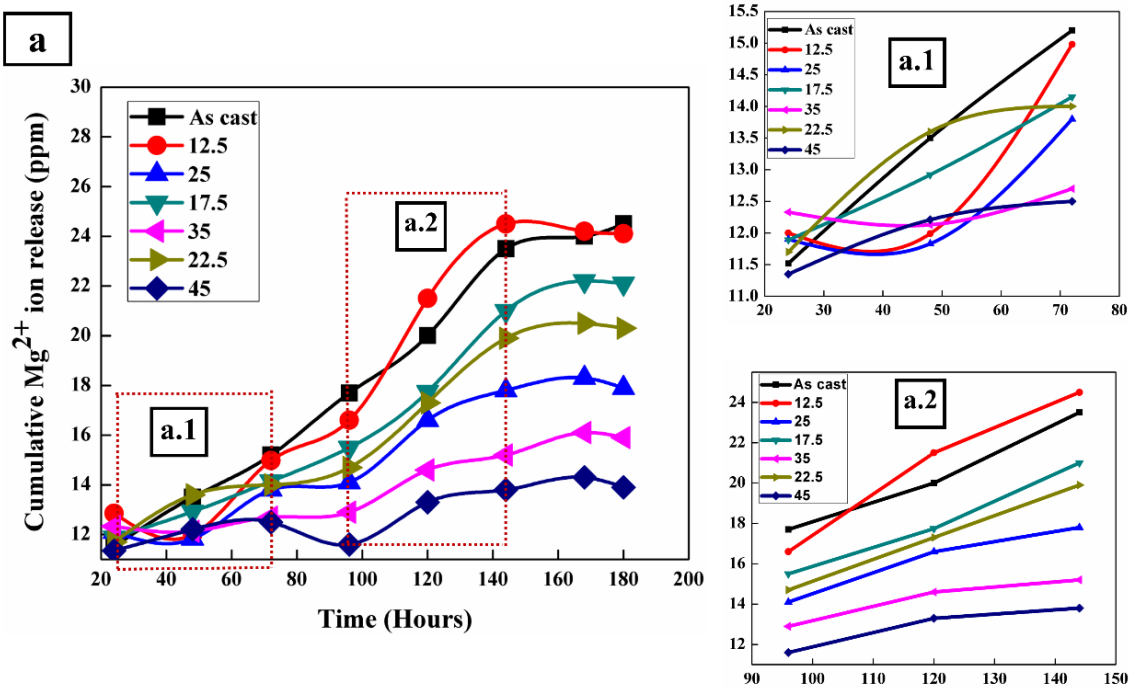

Figure 4.52 (a) Mg^{2+} ion release rate during the period of 180 hours of immersion in HBSS, enlarged views (a.1) and (a.2) as a function of immersion time

The corrosion rates calculated through different ways are compared and presented in the **Figure 4.53**. The corrosion data showed that LSM improves the corrosion resistance and the corrosion rate trends from the three methods are in agreement with each other. The changes in the corrosion behavior of the LSM specimens are mainly due to the factors such as (Mondal et al. (2008), Coy et al. (2010b) and Abbas et al. (2005)) (a) modifications in the microstructure (b) changes in the composition, roughness(Walter and Kannan 2011) or residual stress (Kouadri and Barrallier 2011) caused by the means of high energy laser beam. Microstructures of as cast and LSM samples are taken into account for understanding the corrosion characteristics. The secondary particles precipitated in the as cast alloy were found to be with Gd/Nd particles. These particles were dissolved partially which could be due to the high melting point of both Nd and Gd. Mg_{12} Nd and T-phase (Mg_7Zn_3RE) particles were observed in the alloys and these precipitates are large in size and are non-uniformly distributed. Therefore, the untreated alloy undergoes severe damage by the dissolution of α-Mg matrix near to the secondary phase by galvanic couple formation. When the time of immersion increases, the number of corrosion pits largely formed and expanded. The LSM samples mainly showed improved corrosion resistance due to the grain refinement and uniform distribution of corrosion resistance intermetallic phases such as $Mg_{12}Nd$ and Mg_7Zn_3 due to the rapid solidification. Studies (Alvarez-Lopez et al. (2010) and Hamu et al. (2009)) have reported that because of the fine grain structure more grain boundaries are created and this will act as barrier for corrosion. $Mg_{12}Nd$ phase present in the alloy has little more corrosion potential than Mg (Zhang et al. 2012c). So enrichment and uniform distribution of these phase after LSM leads to positive influence on degradation properties. Under lower energy condition (12.5 J/mm^2) reduced corrosion resistance was observed (3.3 mm/year from weight loss) than as cast alloy mainly due to the solidification cracks at the meltpool region and partially melted phases. It leads to the further galvanic cell formation and leads to a major corrosion pit formation on the exposed surface **(Figure 4.55(b)).** The minimum corrosion rate of 0.5 mm/year was found for 45 J/mm^2 sample which is 83 % higher than the untreated as cast sample. Lower corrosion rate values were observed at low energy density conditions (12.5, 17.5 and 22.5 J/mm^2) which are in the order of 3.3,

2.8 and 2.7 mm/year respectively. The drastic reduction is mainly observed at higher energy density conditions predominantly at 35 and 45 J/mm^2. Apart from other factors, LSM improved the solid solubility of Gd and Nd elements (**Table 4.10**). This enrichment again reduces the corrosion susceptibility of α-Mg by reducing the potential difference between the phases (Liu et al. 2015).

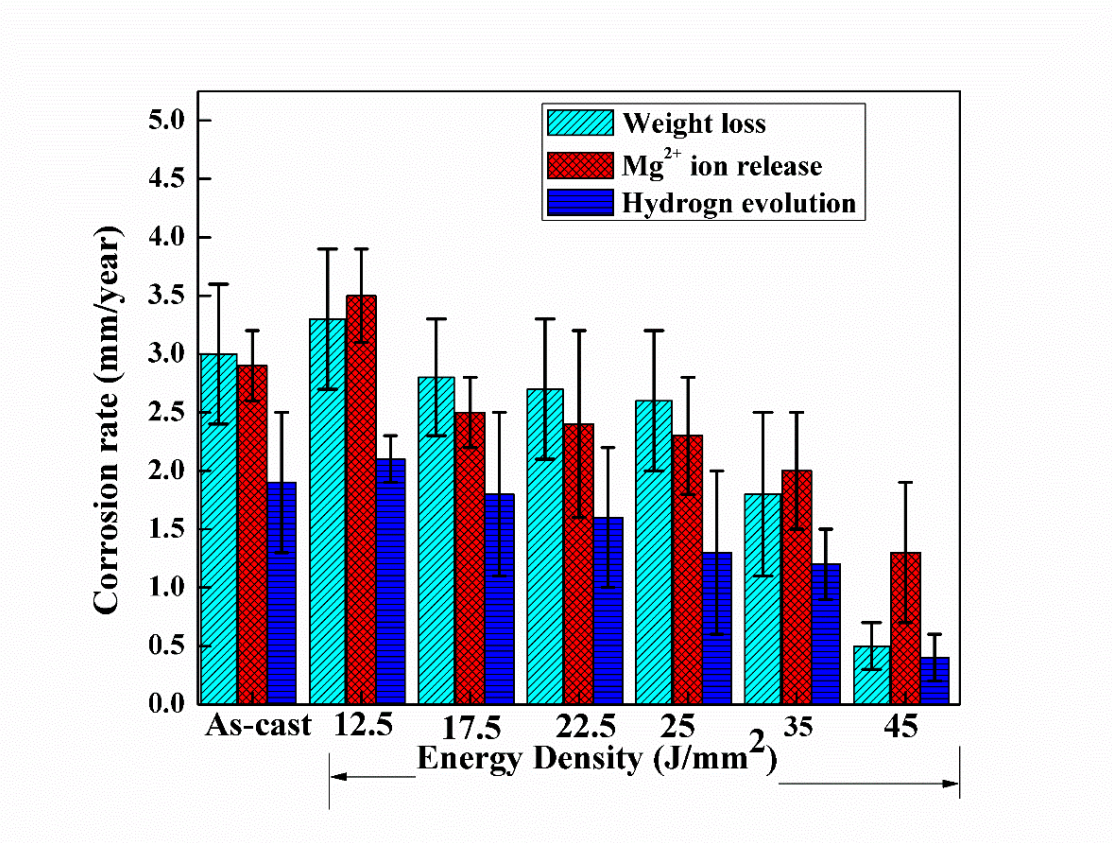

Figure 4.53 Degradation rate comparison through different methods

4.4.7 Corrosion damage characterization

The depth of the corrosion damage and its mechanism can be represented in the cross sectional SEM images of the samples (**Figure 4.54)** after 180 hours of immersion. Out of all the combinations of energy densities, only the once that showed significant variations in the SEM micrographs are discussed here. **Figure 4.54 (a)** shows the as cast sample, where in corroded area is deeply enlarged to the interior and forms a larger pit leaving isolated grains (dashed square) across the region. The LSM processed sample at 12.5 J/mm^2 shows severe damage. The melt zone is completely dissolved into the solution and forming a boat like pit (melt zone pit). An island like melt region

(enlarged view in the **Figure 4.54** (**b)**) was also observed after the corrosion attack on the surface. The potential difference formed between the solidification crack (defects) and the melt zone leads to the formation of corrosion site and this will start to propagate rapidly towards the substrate region (Rakesh et al. 2018). Further difference in the cathode to anode ratio between the melt zone boundary and the substrate promotes the localized corrosion combined with number of corrosion pits (Manne et al. 2018). The formation of smaller pit with slightly affected melt zone was observed in **Figure 4.54** (**c)**, which is processed at 35 J/mm^2. This is an intermediate zone where the corrosion progression was limited. The propagation and the life of the sample depends on the microstructure and depth of the refined zone by the LSM treatment. The maximum depth of 152 µm (**Table 4.7**) was observed at 35 J/mm^2 and is expected to give longer immersion life in HBSS. An area with more pronounced melt zone and with a continuous network of fine cells was observed in the 45 J/mm^2 sample **(Figure 4.54 (d)).** In spite of these, almost no depletion was observed after the immersion for 180 hours at this processing condition.

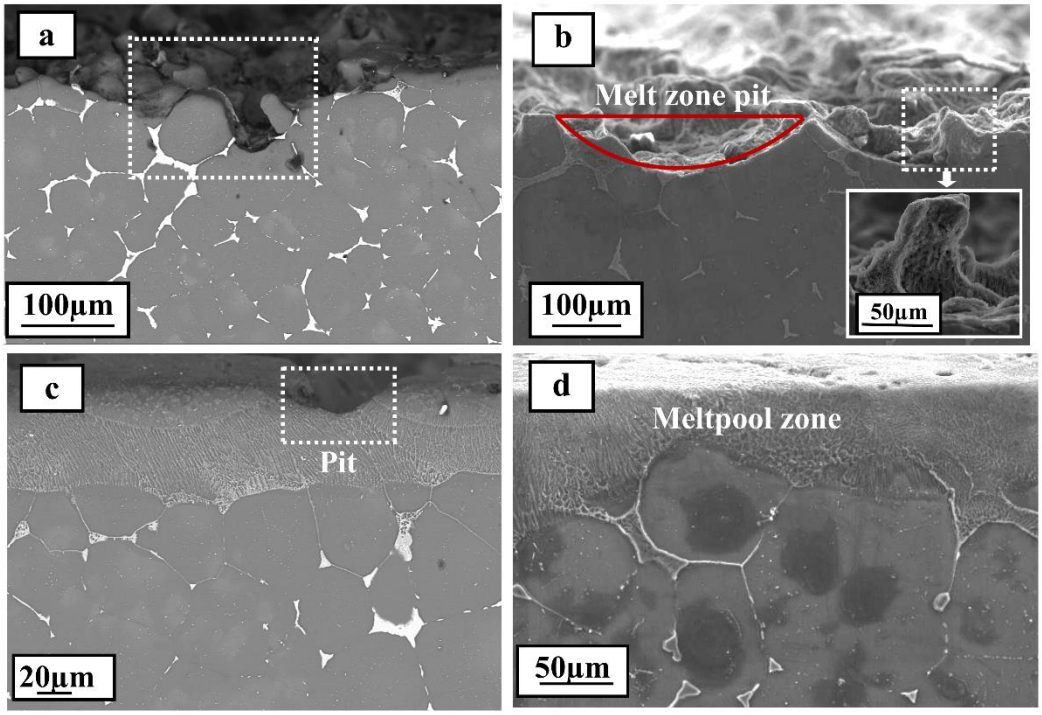

Figure 4.54 Cross sectional SEM images of (a) as cast (b) 12.5 J/mm^2 (c) 35 J/mm^2 (d) 45 J/mm^2 samples after 180 hours of immersion in HBSS.

The exposed area of the surface to HBSS is now accounted in the study and the SEM images are presented in **Figure 4.55.** The degradation characteristics of the LSM samples exhibit pitting combined with modest dissolution of the modified secondary phases (Chang et al. 2007). The surface of the as cast sample shows (**Figure 4.55 (a)**) deep pits at the eutectic compound ($Mg_{12}Nd$) due to the micro galvanic cell formation between this cathodic phase and α-anodic matrix. As a consequence of this galvanic cell formation the corrosion was spread out to the grain boundary region and dissolves the eutectic phase. Finally, the matrix phase isolated with deeper pits (arrow 1 in **Figure 4.55 (a)**) at the grain boundary and random broader pits (arrow **2** in **Figure 4.55 (a)**) were also observed. Number of tiny pits, were formed and spread over the matrix region. This is enlarged and represented in the **Figure 4.55 (a) (**arrow **3**). The corrosion was more advanced on the surface of lower energy density (12.5 J/mm^2) processed sample. After prolonged immersion, different areas were appeared at the exposed surface of 12.5 J/mm^2 sample. Some areas are unaffected and seen as honeycomb like structure **(Figure 4.55 (b)** arrow **1** LSM zone). There are areas where complete dissolution of LSM region and appeared substrate matrix phase on the surface (**Figure 4.55 (b)** arrow **2**). **Figure 4.55 (c)** indicates the surface of 35 J/mm^2 LSM sample with laser track seen after the immersion. The more the surface track seen lesser is the corrosion affected region. The enlarged view shows the presence of the passive film retained on the surface even after removing the corrosion products. The EDS result of this products reveals the formation of protective $Mg(OH)_2$ phase. The degree of attack is considerably lower at 45 J/mm^2 sample and it is represented in **Figure 4.55 (d)**. The formation of smaller pits were observed and it is enlarged (arrow **1**).

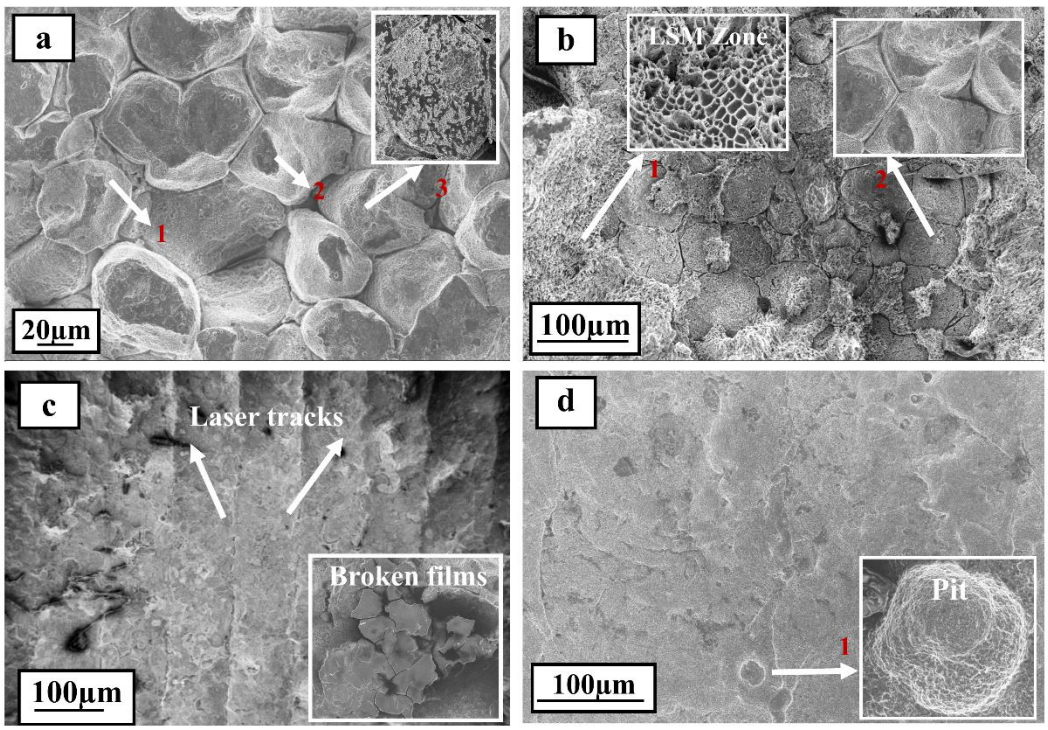

Figure 4.55 Surface morphology of (a) as cast (b) 12.5 J/mm^2 (c) 35 J/mm^2 (d) 45 J/mm^2 samples after 180 hours of immersion in HBSS taken in SEM.

Protective film generation and its involvement on the metallic surface after long term immersion in HBSS was studied by careful removal of corrosion products from the surface. The scrapped corrosion product features are analysed in SEM and are shown in **Figure 4.56**. During the initial stages of immersion, oxides from the solution initiate the corrosion process in metal-solution interface. The continued dissolution of protective layer is followed by oxidation and precipitation of corrosion products (Sikora-Jasinska et al. 2018). The degradation products progressively become thick and it is difficult to remove them from the LSM treated surface. The morphologically different products were formed at the surface at different phases of immersion. It is observed that nearly uniform mode of corrosion results in the LSM treated 25 and 35 J/mm^2 samples. After certain period of immersion, interactive diffusion of the elements from the substrate and HBSS is ceased with increased carbonate/phosphate or hydroxide layer. At the initial stage of immersion the Mg ions are liberated from the surface through the porous layer by capillary action to the solution metal interface. Similarly, various ions from the HBSS propagate in the opposite direction and reacted

with the ions present at the metal surface and new products gets deposited and densified. The formation of protective/passive film further slows the degradation rate. It is observed that the bright and randomly distributed flakes (**Figure 4.56**) consist of Ca, O, P, Mg and Cl. EDS mapping results of this products shows the distribution intensity of these elements. The enlarged SEM (**Figure 4.56** arrow **1**) morphology shows the dense cluster with calcium and phosphate rich phase similar to apatite formation. It stipulates that $H_2PO_4^-$, HPO_4^{2-}, HPO_4 and OH- ions from the HBSS reacted with one other and formed the products effectively on the exposed surface (Zhang et al. 2012e). The XRD results **(Figure 4.57)** shows that degradation products are importantly $Ca_3(PO_4)_2$ (calcium phosphate), $Ca_5(PO_4)_3OH$ (Hydroxyapatite). The major peaks are indexed as 2θ = 31.5°, 45.3°, 56°, 75° and 83.4° for HAp (Hydroxy apatite-Reference code 00-024-0033) and it is bit dominant on the surface. Similarly, calcium phosphate is also suitably indexed (Reference code-00-009-0348). HAp is the essential element in the human bone and the deposition of HAp accelerates the bone tissue growth. Consequently, the formation of products supports the *in-vivo* bone activity of the material and the ratio of Ca/P (1.7) is well above than the actual stoichiometric ratio of Ca/P (1.67) for the better apatite formation (Yang et al. 2016). The presence of Cl^- from the corrosive media transform the $Mg(OH)_2$ passive film into soluble $MgCl_2$ and change the dynamic balance of degradation during the period of immersion (Song et al. 2009). FTIR spectra (**Figure 4.58)** of the corrosion products also confirms the precipitation of phosphate, carbonate and hydroxide components. The intensity band of PO_4^{3-} lies at 563 and 1049 cm^{-1}. This P-O bond shows the indication of hydroxyapatite in crystalline form. The obtained OH^- band at 3430 cm^{-1} is relatively wide and other band observed at 3696 cm^{-1}. CO_3^{2-} group formed a weak peak at 2351 cm^{-1} and comparatively a strong peak observed between 1418 and 1490 cm^{-1} . During the period of immersion the stable calcium phosphate and calcium carbonate precipitate formation might restrict the further corrosion attack on the surface of the sample (Aboudzadeh et al. 2018). One peak of water (H_2O) band was observed at 1642 cm^{-1}. The obtained intensity bands were correlated with the reported studies (Prekajski et al. 2016) (Jebri et al. 2012).

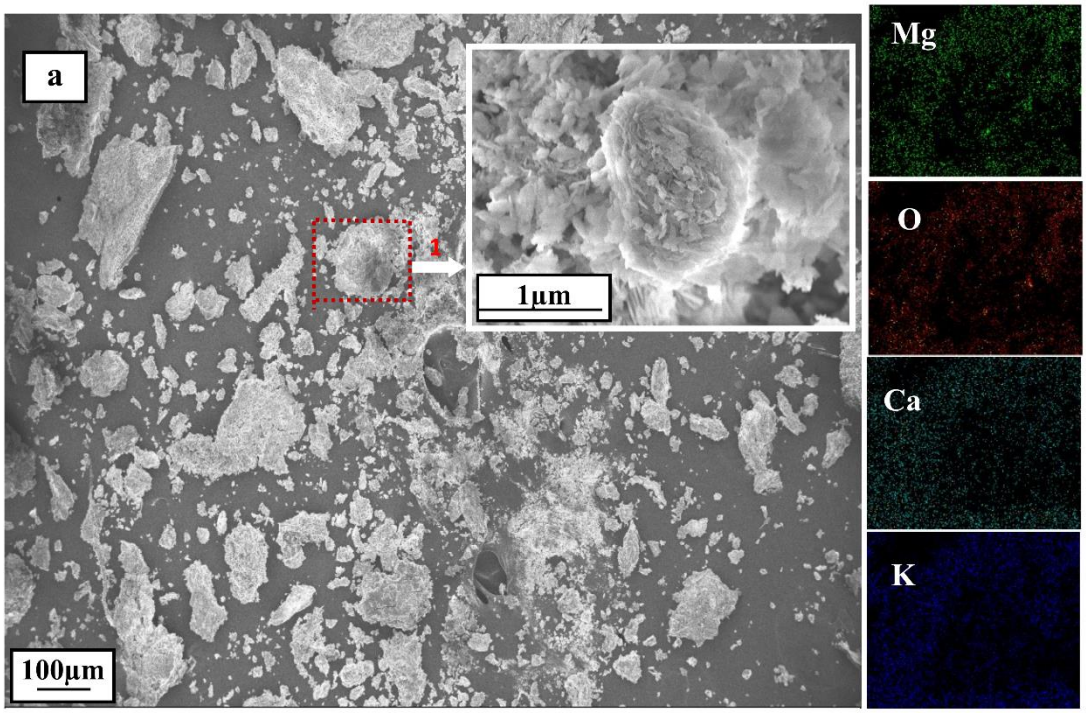

Figure 4.56 SEM + EDS mapping of surface product after immersion study

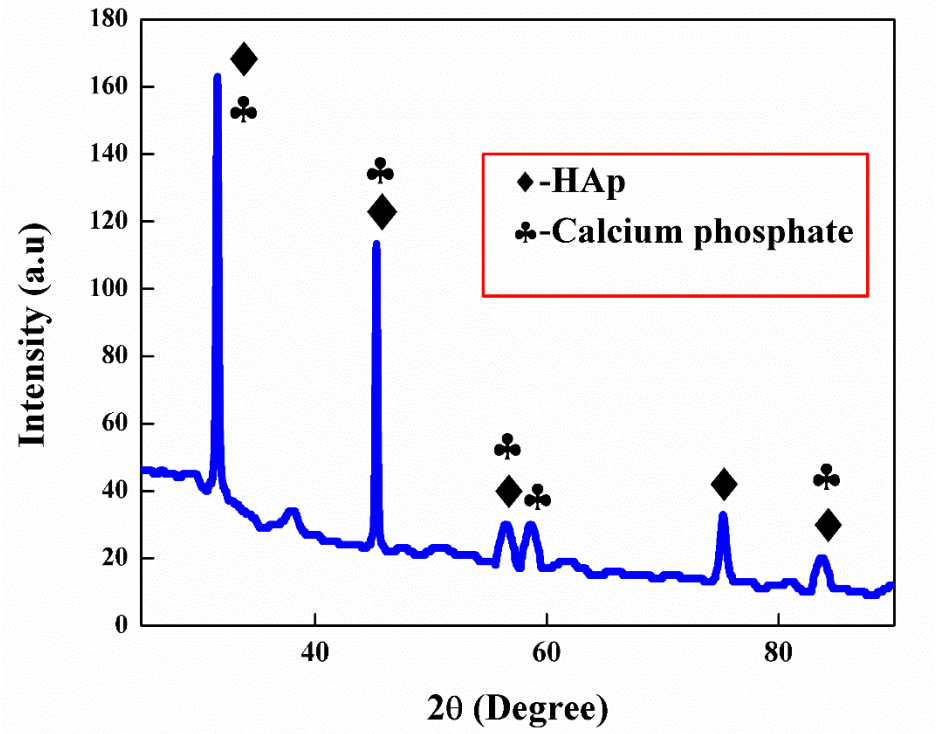

Figure 4.57 XRD spectra of corrosion product after immersion in HBSS for a period of 180 hours

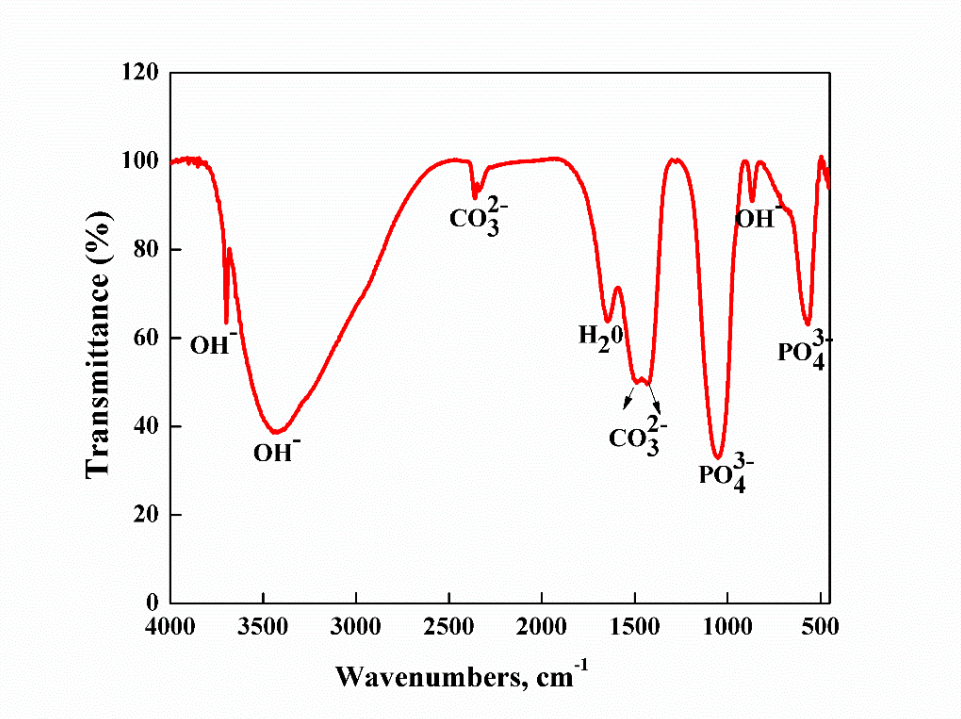

Figure 4.58 FTIR Spectra of corrosion products extracted after 180 hours of immersion in HBSS

4.4.8 Conclusions

- The microstructure of the melt zone consist of equiaxed fine grains of α-mg phase after LSM. The grain refinement (96 % reduction in size) occurs in the meltpool zone was due to high cooling rates and rapid solidification.
- The surface microhardness in the confined meltpool region increased with decrease in grain size. The hardness value slightly decreased at higher energy density (45 J/mm^2) condition due to the grain coarsening at higher scan velocity
- The interaction force, surface energy enhanced from 17.3 mN/m to 36.1 mN/m with decrease in roughness from 15.8 µm to 3.1 µm. Full range of surface wettability is shown to be with better hydrophilic behaviour and these are influenced by the factors of surface roughness, grain size and chemical composition of the processed region.
- The increased corrosion resistance of laser treated specimen at higher energy densities (35 and 45 J/mm^2) could be well associated with dissolution of cathodic particles (Mg_{12} Nd).

CHAPTER 5
5 Conclusions and Future work

5.1 Overall conclusions

Objectives of the present work were to develop Mg-Zn based rare earth element alloys (Mg-1Zn-2Gd, Mg-1Zn-2Dy and Mg-3Zn-1.5Gd-1.5Nd (all in wt. %)) and their surface modification by laser surface melting (LSM). Mechanism of grain refinement, mechanical and corrosion properties were studied and correlated. From the studies carried out on the as-cast and LSM alloys the following conclusions are drawn.

5.1.1 As-cast alloys

- The microstructural features such as LPSO and inderdendritic eutectic phases were formed apart from α-mg phase in Mg-Zn-Gd, Mg-Zn-Dy and Mg-Zn-Gd-Nd alloys.
- The long term degradation studies showed that Mg-Zn-Gd alloy displayed better resistance against degradation and the products which were formed on the surface can support bone cell bridging. The difference in the degradation is mainly influenced by the barrier effect of uniformly distributed intermetallic phases. The improved strength of Mg-Zn-Gd-Nd is also influenced by the strengthening of eutectic phase. Cytotoxicity studies have revealed that all the three alloys are nontoxic.

5.1.2 Laser surface melted alloys

- Average grain size decreases after LSM of the developed alloys. The range of grain size and depth of refinement zone were influenced by the laser processing parameters.
- Laser surface melting improved the corrosion resistance of the alloys. The improvement is due to the combined influence of grain refinement, intermetallic phase dissolution and retention of rare earth elements in the laser melted zone.
- The secure cell adhesion on long term biological response is controllable by the surface morphology of the material. Wettability behaviour on the alloy surface

showed that laser surface melting is a better approach to tailor the surface properties such as roughness and surface energy.

5.2 Future work

In this research, Mg-Zn-REE alloys were developed as resorbable biomedical materials. Further, surface properties of these alloys were tailored by laser surface melting approach. Studies such as microstructure changes, mechanical behavior, corrosion behavior and cytotoxicity were carried on as cast and LSM alloys. The following tasks have been identified as future research directions.

- Evaluate the effect of heat treatment on as cast and laser surface melted alloys.
- Carry out fretting wear studies on LSM alloys and correlate the effects of energy density on wear behaviour.
- Various in-vitro cell interaction studies such as MTT assay, gene expression and ALP assay can be scientifically explore on as cast and LSM alloys.
- In vivo studies in animals can be carried out before going into clinical stages.

REFERENCES

Abbas, G., Liu, Z., and Skeldon, P. (2005). "Corrosion behaviour of laser-melted magnesium alloys." *Appl. Surf. Sci.*, 247(1–4), 347–353.

ABOUDZADEH, N., DEHGHANIAN, C., and SHOKRGOZAR, M. A. (2018). "In vitro degradation and cytotoxicity of Mg-5Zn-0.3Ca/nHA biocomposites prepared by powder metallurgy." *Trans. Nonferrous Met. Soc. China (English Ed.)*, 28(9), 1745–1754.

Alvarez-Lopez, M., Pereda, M. D., Valle, J. A. Del, Fernandez-Lorenzo, M., Garcia-Alonso, M. C., Ruano, O. A., and Escudero, M. L. (2010). "Corrosion behaviour of AZ31 magnesium alloy with different grain sizes in simulated biological fluids." *Acta Biomater.*, 6(5), 1763–1771.

Andrews, E. W. (1917). "absorbable metal clips."

Arima, Y., and Iwata, H. (2007). "Effect of wettability and surface functional groups on protein adsorption and cell adhesion using well-defined mixed self-assembled monolayers." *Biomaterials*, 28(20), 3074–3082.

Atrens, A., Liu, M., and Zainal Abidin, N. I. (2011). "Corrosion mechanism applicable to biodegradable magnesium implants." *Mater. Sci. Eng. B Solid-State Mater. Adv. Technol.*, 176(20), 1609–1636.

Atrens, A., Song, G.-L., Liu, M., Shi, Z., Cao, F., and Dargusch, M. S. (2015). "Review of Recent Developments in the Field of Magnesium Corrosion." *Adv. Eng. Mater.*, 17(4), 400–453.

Atrens, A., Song, G., Cao, F., Shi, Z., and Bowen, P. K. (2013). "ScienceDirect Advances in Mg corrosion and research suggestions." *J. Magnes. Alloy.*, 1(3), 177–200.

Baier, R. E. (2006). "Surface behaviour of biomaterials: The theta surface for biocompatibility." *J. Mater. Sci. Mater. Med.*, 17(11), 1057–1062.

Bakhsheshi-Rad, H. R., Abdul-Kadir, M. R., Idris, M. H., and Farahany, S. (2012). "Relationship between the corrosion behavior and the thermal characteristics and microstructure of Mg-0.5Ca-xZn alloys." *Corros. Sci.*, 64(June), 184–197.

Balla, V. K., and Bandyopadhyay, A. (2010). "Laser processing of Fe-based bulk amorphous alloy." *Surf. Coatings Technol.*, 205(7), 2661–2667.

Balla, V. K., Das, M., Bose, S., Janaki Ram, G. D., and Manna, I. (2013). "Laser surface modification of 316 L stainless steel with bioactive hydroxyapatite." *Mater. Sci. Eng. C*, 33(8), 4594–4598.

Banerjee, P. C., Raman, R. K. S., Durandet, Y., and McAdam, G. (2011). "Electrochemical investigation of the influence of laser surface melting on the microstructure and corrosion behaviour of ZE41 magnesium alloy – An EIS based study." *Corros. Sci.*, 53(4), 1505–1514.

Bi, G., Fang, D., Zhao, L., Lian, J., Jiang, Q., and Jiang, Z. (2011). "An elevated temperature Mg–Dy–Zn alloy with long period stacking ordered phase by extrusion." *Mater. Sci. Eng. A*, 528(10–11), 3609–3614.

Bi, G., Li, Y., Zang, S., Zhang, J., Ma, Y., and Hao, Y. (2014). "Microstructure, mechanical and corrosion properties of Mg–2Dy–xZn (x=0, 0.1, 0.5 and 1 at.%) alloys." *J. Magnes. Alloy.*, 2(1), 64–71.

Boehlert, C. J., and Knittel, K. (2006). "The microstructure , tensile properties , and creep behavior of Mg – Zn alloys containing 0 – 4 . 4 wt .% Zn." 417, 315–321.

Brar, H. S., Wong, J., and Manuel, M. V. (2012). "Investigation of the mechanical and degradation properties of Mg–Sr and Mg–Zn–Sr alloys for use as potential biodegradable implant materials." *J. Mech. Behav. Biomed. Mater.*, 7, 87–95.

Cai, S., Lei, T., Li, N., and Feng, F. (2012). "Effects of Zn on microstructure, mechanical properties and corrosion behavior of Mg-Zn alloys." *Mater. Sci. Eng. C*, 32(8), 2570–2577.

Cao, P., Qian, M., and Stjohn, D. H. (2005). “Native grain refinement of magnesium alloys.” 53, 841–844.

Cha, P., Han, H., Yang, G., Kim, Y., Hong, K., Lee, S., Jung, J., Ahn, J., Kim, Y., Cho, S., Byun, J. Y., and Lee, K. (2013). “Biodegradability engineering of biodegradable Mg alloys : Tailoring the electrochemical properties and microstructure of constituent phases.” *Sci. Rep.*, 3, 1–6.

Chang, J. W., Fu, P. H., Guo, X. W., Peng, L. M., and Ding, W. J. (2007). “The effects of heat treatment and zirconium on the corrosion behaviour of Mg-3Nd-0.2Zn-0.4Zr (wt.%) alloy.” *Corros. Sci.*, 49(6), 2612–2627.

Chen, Y., Xu, Z., Smith, C., and Sankar, J. (2014). “Recent advances on the development of magnesium alloys for biodegradable implants.” *Acta Biomater.*, 10(11), 4561–4573.

Cor, E. (2004). “Standard Practice for Laboratory Immersion Corrosion Testing of Metals 1.” *Corrosion*, 72(Reapproved), 1–8.

Coy, A. E., Viejo, F., Garcia-Garcia, F. J., Liu, Z., Skeldon, P., and Thompson, G. E. (2010a). “Effect of excimer laser surface melting on the microstructure and corrosion performance of the die cast AZ91D magnesium alloy.” *Corros. Sci.*, 52(2), 387–397.

Das, M., Bhattacharya, K., Dittrick, S. A., Mandal, C., Krishna, V., Kumar, T. S. S., and Bandyopadhyay, A. (2014). “In situ synthesized TiB – TiN reinforced Ti6Al4V alloy composite coatings : Microstructure , tribological and in-vitro biocompatibility.” *J. Mech. Behav. Biomed. Mater.*, 29, 259–271.

Datta, M. K., Chou, D. T., Hong, D., Saha, P., Chung, S. J., Lee, B., Sirinterlikci, A., Ramanathan, M., Roy, A., and Kumta, P. N. (2011). “Structure and thermal stability of biodegradable Mg-Zn-Ca based amorphous alloys synthesized by mechanical alloying.” *Mater. Sci. Eng. B Solid-State Mater. Adv. Technol.*, 176(20), 1637–1643.

Dean, D. D. (1996). “Surface roughness modulates the local production of growth factors and cytokines by Surface roughness modulates the local production of growth

factors and cytokines by osteoblast-like.” 32(March 2017), 55–63.

Demir, A. G., Furlan, V., Lecis, N., and Previtali, B. (2014). “Laser surface structuring of AZ31 Mg alloy for controlled wettability.” *Biointerphases*, 9(2), 029009.

Ding, R., Chung, C., Chiu, Y., and Lyon, P. (2010). “Effect of ECAP on microstructure and mechanical properties of ZE41 magnesium alloy.” *Mater. Sci. Eng. A*, 527(16–17), 3777–3784.

Dubé, D., Fiset, M., Couture, A., and Nakatsugawa, I. (2001). “Characterization and performance of laser melted AZ91D and AM60B.” *Mater. Sci. Eng. A*, 299(1–2), 38–45.

Dutta, J., Arun, M., Sisa, K., and Manna, P. I. (2018). “Laser Surface Melting of AISI 316L Stainless Steel for Bio-implant Application.” *Proc. Natl. Acad. Sci. India Sect. A Phys. Sci.*

Dutta Majumdar, J., Galun, R., Mordike, B. L., and Manna, I. (2003). “Effect of laser surface melting on corrosion and wear resistance of a commercial magnesium alloy.” *Mater. Sci. Eng. A*, 361(1–2), 119–129.

Easton, M. A., Gibson, M. A., Qiu, D., Zhu, S. M., and Gro, J. (2012). “The role of crystallography and thermodynamics on phase selection in binary magnesium – rare earth (Ce or Nd) alloys.” 60, 4420–4430.

Feyerabend, F., Fischer, J., Holtz, J., Witte, F., Willumeit, R., Drücker, H., Vogt, C., and Hort, N. (2010a). “Acta Biomaterialia Evaluation of short-term effects of rare earth and other elements used in magnesium alloys on primary cells and cell lines q.” *Acta Biomater.*, 6(5), 1834–1842.

Feyerabend, F., Fischer, J., Holtz, J., Witte, F., Willumeit, R., Drücker, H., Vogt, C., and Hort, N. (2010b). “Evaluation of short-term effects of rare earth and other elements used in magnesium alloys on primary cells and cell lines.” *Acta Biomater.*, 6(5), 1834–1842.

Fotovvati, B., Wayne, S. F., Lewis, G., and Asadi, E. (2018). “A Review on Melt-Pool

Characteristics in Laser Welding of Metals.” *Adv. Mater. Sci. Eng.*, 2018.

Friedrich, H. E., and Mordike, B. L. (2006). *Magnesium technology: Metallurgy, design data, applications. Magnes. Technol. Metall. Des. Data, Appl.*

Friedrich, H., and Schumann, S. (2001). “Research for a `` new age of magnesium ’ ’ in the automotive industry.” 117, 276–281.

Furlan, V., Demir, A. G., and Previtali, B. (2015). “Micro and sub-micron surface structuring of AZ31 by laser re-melting and dimpling.” *Opt. Laser Technol.*, 75, 164–172.

Gan, Y., Wang, W., Cui, Z., Yan, X., Guan, Z., and Xu, B. (2015). “Numerical and experimental study of the temperature field evolution of Mg alloy during high power diode laser surface melting.” *Optik (Stuttg).*, 126(7–8), 739–743.

Gao, L., Chen, R. S., and Han, E. H. (2009). “Effects of rare-earth elements Gd and Y on the solid solution strengthening of Mg alloys.” *J. Alloys Compd.*, 481(1–2), 379–384.

Gao, X., and Nie, J. F. (2007). “Structure and thermal stability of primary intermetallic particles in an Mg-Zn casting alloy.” *Scr. Mater.*, 57(7), 655–658.

Gao, Y., Wang, C., Yao, M., and Liu, H. (2007). “Corrosion behavior of laser melted AZ91HP magnesium alloy.” *Mater. Corros.*, 58(6), 463–466.

Gökhan, A., Taketa, T. B., Tolouei, R., Furlan, V., Paternoster, C., Beppu, M. M., Mantovani, D., and Previtali, B. (2015). “Laser surface structuring affects polymer deposition , coating homogeneity , and degradation rate of Mg alloys.” *Mater. Lett.*, 160, 359–362.

Guan, Y. C., Zhou, W., Li, Z. L., and Zheng, H. Y. (2013). “Femtosecond laser-induced iridescent effect on AZ31B magnesium alloy surface.” *J. Phys. D. Appl. Phys.*, 46(42).

Guan, Y. C., Zhou, W., and Zheng, H. Y. (2009). “Effect of laser surface melting on corrosion behaviour of AZ91D Mg alloy in simulated-modified body fluid.” *J. Appl.*

Electrochem., 39(9), 1457–1464.

Guangli, B. I., Jing, J., Fan, Z., and Daqing, F. (2016). “Microstructure evolution and corrosion properties of Mg-Dy-Zn alloy during cooling after solution treatment.” 34(9), 931–937.

Gui, Z., Kang, Z., and Li, Y. (2018). “Evolution of the microstructure and fracture characteristics of a Mg- Nd-Zn-Zr-Mn alloy through heat treatment and extrusion.” *J. Alloys Compd.*, 68(9), 4.

Guo, L. F., Yue, T. M., and Man, H. C. (2005). “Excimer laser surface treatment of magnesium alloy WE43 for.” *J. Mater. Sci.*, 40, 3531–3533.

Hamu, G. Ben, Eliezer, D., and Wagner, L. (2009). “The relation between severe plastic deformation microstructure and corrosion behavior of AZ31 magnesium alloy.” 468, 222–229.

He, S. M., Zeng, X. Q., Peng, L. M., Gao, X., Nie, J. F., and Ding, W. J. (2007). “Microstructure and strengthening mechanism of high strength Mg – 10Gd – 2Y – 0 . 5Zr alloy.” 427, 316–323.

Heublein, B., Rohde, R., Kaese, V., Niemeyer, M., Hartung, W., and Haverich, a. (2003). “Biocorrosion of magnesium alloys: a new principle in cardiovascular implant technology?” *Heart*, 89(6), 651–656.

Ho, Y.-H., Vora, H. D., and Dahotre, N. B. (2015a). “Laser surface modification of AZ31B Mg alloy for bio-wettability.” *J. Biomater. Appl.*, 29(7), 915–928.

Honma, T., Ohkubo, T., Kamado, S., and Hono, K. (2007). “Effect of Zn additions on the age-hardening of Mg – 2 . 0Gd – 1 . 2Y – 0 . 2Zr alloys.” 55, 4137–4150.

Hort, N., Huang, Y., Fechner, D., Störmer, M., Blawert, C., Witte, F., Vogt, C., Drücker, H., Willumeit, R., and Kainer, K. U. (2010a). “Magnesium alloys as implant materials – Principles of property design for Mg–RE alloys☆.” *Acta Biomater.*, 6(5), 1714–1725.

Hort, N., Huang, Y., Fechner, D., Störmer, M., Blawert, C., Witte, F., Vogt, C., Drücker, H., Willumeit, R., Kainer, K. U., and Feyerabend, F. (2010b). "Magnesium alloys as implant materials-Principles of property design for Mg-RE alloys." *Acta Biomater.*, 6(5), 1714–1725.

Hu, G., Zhang, D., Tang, T., Shen, X., and Jiang, L. (2015). "Materials Science & Engineering A Effects of Nd addition on microstructure and mechanical properties of Mg – 6Zn – 1Mn – 4Sn alloy." *Mater. Sci. Eng. A*, 634, 5–13.

Janssen, M. I., Leeuwen, M. B. M. Van, Kooten, T. G. Van, Vries, J. De, Dijkhuizen, L., and Wösten, H. A. B. (2004). "Promotion of fibroblast activity by coating with hydrophobins in the β-sheet end state." *Biomaterials*, 25(14), 2731–2739.

Jebri, S., Boughzala, H., Bechrifa, A., and Jemal, M. (2012). "Structural analysis and thermochemistry of 'A' type phosphostrontium carbonate hydroxyapatites." *J. Therm. Anal. Calorim.*, 107(3), 963–972.

Johnston, S., Shi, Z., and Atrens, A. (2015). "The influence of pH on the corrosion rate of high-purity Mg, AZ91 and ZE41 in bicarbonate buffered Hanks' solution." *Corros. Sci.*, 101, 182–192.

Kannan, M. B., and Raman, R. K. S. (2008). "In vitro degradation and mechanical integrity of calcium-containing magnesium alloys in modified-simulated body fluid." *Biomaterials*, 29(15), 2306–2314.

Kim, J. M., and Park, J. S. (2011). "Microstructure and tensile properties of Mg – Zn – Gd casting alloys." *Int. J. Cast Met. Res.*, 24(2), 127–130.

Kouadri, A., and Barrallier, L. (2011). "Study of mechanical properties of AZ91 magnesium alloy welded by laser process taking into account the anisotropy microhardness and residual stresses by X-ray diffraction." *Metall. Mater. Trans. A Phys. Metall. Mater. Sci.*, 42(7), 1815–1826.

Kurella, A. K., Hu, M. Z., and Dahotre, N. B. (2008). "Effect of microstructural evolution on wettability of laser coated calcium phosphate on titanium alloy." *Mater.*

Sci. Eng. C, 28(8), 1560–1564.

Lei, T., Tang, W., Cai, S. H., Feng, F. F., and Li, N. F. (2012). "On the corrosion behaviour of newly developed biodegradable Mg-based metal matrix composites produced by in situ reaction." *Corros. Sci.*, 54(1), 270–277.

Li, C. Q., Xu, D. K., Zeng, Z. R., Wang, B. J., Sheng, L. Y., Chen, X. B., and Han, E. H. (2017). "Effect of volume fraction of LPSO phases on corrosion and mechanical properties of Mg-Zn-Y alloys." *Mater. Des.*, 121, 430–441.

Li, N., and Zheng, Y. (2013). "Novel Magnesium Alloys Developed for Biomedical Application: A Review." *J. Mater. Sci. Technol.*, 29(6), 489–502.

Li, Y., Wen, C., Mushahary, D., Sravanthi, R., Harishankar, N., Pande, G., and Hodgson, P. (2012). "Mg-Zr-Sr alloys as biodegradable implant materials." *Acta Biomater.*, 8(8), 3177–3188.

Li, Z., Gu, X., Lou, S., and Zheng, Y. (2008a). "The development of binary Mg-Ca alloys for use as biodegradable materials within bone." *Biomaterials*, 29(10), 1329–1344.

Lincks, J., Boyan, B. D., Blanchard, C. R., Lohmann, C. H., Liu, Y., Cochran, D. L., Dean, D. D., and Schwartz, Z. (2006). "Response of MG63 osteoblast-like cells to titanium and titanium alloy is dependent on surface roughness and composition." *Biomater. Silver Jubil. Compend.*, 19, 147–160.

Liu, C., Liang, J., Zhou, J., Wang, L., and Li, Q. (2015). "Effect of laser surface melting on microstructure and corrosion characteristics of AM60B magnesium alloy." *Appl. Surf. Sci.*, 343, 133–140.

Liu, S. Y., Hu, J. D., Yang, Y., Guo, Z. X., and Wang, H. Y. (2005). "Microstructure analysis of magnesium alloy melted by laser irradiation." *Appl. Surf. Sci.*, 252(5), 1723–1731.

Liu, X. B., Chen, R. S., and Han, E. H. (2008). "Effects of ageing treatment on microstructures and properties of Mg-Gd-Y-Zr alloys with and without Zn additions."

J. Alloys Compd., 465(1–2), 232–238.

Lu, F., Ma, A., Jiang, J., Chen, J., Song, D., Yuan, Y., Chen, J., and Yang, D. (2015). "Enhanced mechanical properties and rolling formability of fine-grained Mg-Gd-Zn-Zr alloy produced by equal-channel angular pressing." *J. Alloys Compd.*, 643, 28–33.

Manne, B., Thiruvayapati, H., Bontha, S., Motagondanahalli Rangarasaiah, R., Das, M., and Balla, V. K. (2018). "Surface design of Mg-Zn alloy temporary orthopaedic implants: Tailoring wettability and biodegradability using laser surface melting." *Surf. Coatings Technol.*, 347(January), 337–349.

Mondal, A. K., Kumar, S., Blawert, C., and Dahotre, N. B. (2008). "Effect of laser surface treatment on corrosion and wear resistance of ACM720 Mg alloy." *Surf. Coatings Technol.*, 202(14), 3187–3198.

Morishita, M., Yamamoto, H., Shikada, S., Kusumoto, M., and Matsumoto, Y. (2006). "Thermodynamics of the formation of magnesium-zinc intermetallic compounds in the temperature range from absolute zero to high temperature." *Acta Mater.*, 54(11), 3151–3159.

Mushahary, D., Sravanthi, R., Li, Y., Kumar, M. J., Harishankar, N., Hodgson, P. D., Wen, C., and Pande, G. (2013). "Zirconium, calcium, and strontium contents in magnesium based biodegradable alloys modulate the efficiency of implant-induced osseointegration." *Int. J. Nanomedicine*, 8(June), 2887–2902.

Neil, W. C., Forsyth, M., Howlett, P. C., Hutchinson, C. R., and Hinton, B. R. W. (2009). "Corrosion of magnesium alloy ZE41 - The role of microstructural features." *Corros. Sci.*, 51(2), 387–394.

Ng, W. F., Chiu, K. Y., and Cheng, F. T. (2010). "Effect of pH on the in vitro corrosion rate of magnesium degradable implant material." *Mater. Sci. Eng. C*, 30(6), 898–903.

Nge, T. T., Sugiyama, J., and Bulone, V. (2010). "Bacterial Cellulose-based Biomimetic Composites Bacterial Cellulose-Based Biomimetic Composites." (September).

Ninlachart, J., and Raja, K. S. (2017). “Passivation kinetics of Mg-Nd-Gd-Zn-Zr (EV31A) and Mg-Y-Nd-Gd-Zr (WE43C) in NaOH solutions.” *J. Magnes. Alloy.*, 5(3), 254–270.

Okamoto, H. (2013). “Supplemental literature review of binary phase diagrams: Cs-In, Cs-K, Cs-Rb, Eu-In, Ho-Mn, K-Rb, Li-Mg, Mg-Nd, Mg-Zn, Mn-Sm, O-Sb, and Si-Sr.” *J. Phase Equilibria Diffus.*, 34(3), 251–263.

Olakanmi, E. O., Cochrane, R. F., and Dalgarno, K. W. (2015). “A review on selective laser sintering/melting (SLS/SLM) of aluminium alloy powders: Processing, microstructure, and properties.” *Prog. Mater. Sci.*, 74, 401–477.

Owens, D. K., and Wendt, R. C. (1969). “Estimation of the surface free energy of polymers.” *J. Appl. Polym. Sci.*, 13(8), 1741–1747.

Ozdemir, R., and Karahan, I. H. (2015). “Grain size calculation of Cu-Zn alloys using Genetic programming; an alternative for Scherer’s formula.” *J. Optoelectron. Adv. Mater.*, 17(1–2), 14–26.

Pan, H., Yang, H., Tang, X., Niu, J., Xiang, Z., Song, Y., and Lu, W. (2017). “Effect of Ca/P ratio on the structural and corrosion properties of biomimetic Ca[sbnd]P coatings on ZK60 magnesium alloy.” *Mater. Sci. Eng. C*, 72, 676–681.

Pekounov, Y., and Petrov, O. E. (2008). “Bone resembling apatite by amorphous-to-crystalline transition driven self-organisation.” *J. Mater. Sci. Mater. Med.*, 19(2), 753–759.

Peng, Q., Huang, Y., Zhou, L., Hort, N., and Kainer, K. U. (2010). “Preparation and properties of high purity Mg-Y biomaterials.” *Biomaterials*, 31(3), 398–403.

Peng, Q., Wang, L. L., and Wu, Y. (2009). “Structure stability and strengthening mechanism of die-cast Mg-Gd-Dy based alloy.” *J. Alloys Compd.*, 469(1–2), 587–592.

Prekajski, M., Mirković, M., Todorović, B., Matković, A., Marinović-Cincović, M., Luković, J., and Matović, B. (2016). “Ouzo effect-New simple nanoemulsion method for synthesis of strontium hydroxyapatite nanospheres.” *J. Eur. Ceram. Soc.*, 36(5),

1293–1298.

Qian, M., and Stjohn, D. H. (2009). “Grain nucleation and formation in Mg – Zr alloys.” 22(1), 2–5.

Qin, H., Zhao, Y., An, Z., Cheng, M., Wang, Q., Cheng, T., Wang, Q., Wang, J., Jiang, Y., Zhang, X., and Yuan, G. (2015). “Enhanced antibacterial properties, biocompatibility, and corrosion resistance of degradable Mg-Nd-Zn-Zr alloy.” *Biomaterials*, 53, 211–220.

Rakesh, K. R., Bontha, S., Ramesh, M. R., Arya, S. B., and Das, M. (2018). “Laser surface modification of Mg-Zn-Gd alloy : microstructural , wettability and in vitro degradation aspects Laser surface modi fi cation of Mg-Zn-Gd alloy : microstructural , wettability and in vitro degradation aspects.” *Mater. resesrch express*, 5, 126502.

Rosales-Leal, J. I., Rodríguez-Valverde, M. A., Mazzaglia, G., Ramón-Torregrosa, P. J., Díaz-Rodríguez, L., García-Martínez, O., Vallecillo-Capilla, M., Ruiz, C., and Cabrerizo-Vílchez, M. A. (2010). “Effect of roughness, wettability and morphology of engineered titanium surfaces on osteoblast-like cell adhesion.” *Colloids Surfaces A Physicochem. Eng. Asp.*, 365(1–3), 222–229.

Rupp, F., Scheideler, L., Rehbein, D., Axmann, D., and Geis-Gerstorfer, J. (2004). “Roughness induced dynamic changes of wettability of acid etched titanium implant modifications.” *Biomaterials*, 25(7–8), 1429–1438.

Seal, C. K., Vince, K., and Hodgson, M. A. (2009). “Biodegradable surgical implants based on magnesium alloys – A review of current research.” *IOP Conf. Ser. Mater. Sci. Eng.*, 4, 012011.

Seelig. (1924). “Magnesium Prostheses.” *Arch. Surg.*, 1907(July 28).

Semak, V., and Matsunawa, A. (1999). “The role of recoil pressure in energy balance during laser materials processing.” *J. Phys. D. Appl. Phys.*, 30(18), 2541–2552.

Shao, X. H., Yang, Z. Q., and Ma, X. L. (2010). “Strengthening and toughening mechanisms in Mg–Zn–Y alloy with a long period stacking ordered structure.” *Acta*

Mater., 58(14), 4760–4771.

Shi, Z., Liu, M., and Atrens, A. (2010). "Measurement of the corrosion rate of magnesium alloys using Tafel extrapolation." *Corros. Sci.*, 52(2), 579–588.

Sikora-Jasinska, M., Chevallier, P., Turgeon, S., Paternoster, C., Mostaed, E., Vedani, M., and Mantovani, D. (2018). "Long-term in vitro degradation behaviour of Fe and Fe/Mg2Si composites for biodegradable implant applications." *RSC Adv.*, 8(18), 9627–9639.

Song, G., and Atrens, a. (2003). "Understanding Magnesium Corrosion—A Framework for Improved Alloy Performance." *Adv. Eng. Mater.*, 5(12), 837–858.

Song, G., Atrens, A., and StJohn, D. (2013). "An Hydrogen Evolution Method for the Estimation of the Corrosion Rate of Magnesium Alloys." *Magnes. Technol. 2001*, (January), 254–262.

Song, G., and Song, S. (2007). "A Possible Biodegradable Magnesium Implant Material." *Adv. Eng. Mater.*, 9(4), 298–302.

Song, Y., Han, E., Shan, D., Dong, C., and Sun, B. (2012a). "The effect of Zn concentration on the corrosion behavior of Mg – x Zn alloys." *Corros. Sci.*, 65, 322–330.

Song, Y., Shan, D., Chen, R., Zhang, F., and Han, E. H. (2009). "Biodegradable behaviors of AZ31 magnesium alloy in simulated body fluid." *Mater. Sci. Eng. C*, 29(3), 1039–1045.

Srinivasan, A., Blawert, C., Huang, Y., Mendis, C. L., Kainer, K. U., and Hort, N. (2014a). "Corrosion behavior of Mg–Gd–Zn based alloys in aqueous NaCl solution." *J. Magnes. Alloy.*, 2(3), 245–256.

Srinivasan, A., Huang, Y., Mendis, C. L., Blawert, C., Kainer, K. U., and Hort, N. (2014b). "Investigations on microstructures, mechanical and corrosion properties of Mg-Gd-Zn alloys." *Mater. Sci. Eng. A*, 595, 224–234.

Staiger, M. P., Pietak, A. M., Huadmai, J., and Dias, G. (2006). “Magnesium and its alloys as orthopedic biomaterials: A review.” *Biomaterials*, 27(9), 1728–1734.

Taltavull, C., Torres, B., Lopez, A. J., Rodrigo, P., Otero, E., Atrens, A., and Rams, J. (2014). “Corrosion behaviour of laser surface melted magnesium alloy AZ91D.” *Mater. Des.*, 57, 40–50.

Taltavull, C., Torres, B., López, A. J., Rodrigo, P., and Rams, J. (2013). “Surface & Coatings Technology Novel laser surface treatments on AZ91 magnesium alloy.” *Surf. Coat. Technol.*, 222, 118–127.

Thi, T., Sugiyama, J., and Bulone, V. (2010). “Bacterial Cellulose-based Biomimetic Composites.” *Biopolymers*, (September), 3–11.

Thomas, S., Medhekar, N. V, Frankel, G. S., and Birbilis, N. (2015). “Corrosion mechanism and hydrogen evolution on Mg.” *Curr. Opin. Solid State Mater. Sci.*, 19(2), 85–94.

Troitskii, V. V, and Tsitrin, D. N. (1944). “The resorbing metallic alloy ‘Osteosinthezit’ as material for fastening broken bone.” *Khirurgiia (Sofiia).*, 8(1944), 41–44.

Vora, H. D., Santhanakrishnan, S., Harimkar, S. P., Boetcher, S. K. S., and Dahotre, N. B. (2012). “Evolution of surface topography in one-dimensional laser machining of.” 32, 4205–4218.

Vora, H. D., Santhanakrishnan, S., Harimkar, S. P., Boetcher, S. K. S., and Dahotre, N. B. (2013). “One-dimensional multipulse laser machining of structural alumina: Evolution of surface topography.” *Int. J. Adv. Manuf. Technol.*, 68(1–4), 69–83.

Walter, R., and Kannan, M. B. (2011). “Influence of surface roughness on the corrosion behaviour of magnesium alloy.” *Mater. Des.*, 32(4), 2350–2354.

Wan, Y., Xiong, G., Luo, H., He, F., Huang, Y., and Zhou, X. (2008). “Preparation and

characterization of a new biomedical magnesium-calcium alloy." *Mater. Des.*, 29(10), 2034–2037.

Wang, L., Shinohara, T., and Zhang, B. P. (2010). "XPS study of the surface chemistry on AZ31 and AZ91 magnesium alloys in dilute NaCl solution." *Appl. Surf. Sci.*, 256(20), 5807–5812.

Wei, J., Igarashi, T., Okumori, N., Igarashi, T., Maetani, T., Liu, B., and Yoshinari, M. (2009). "Influence of surface wettability on competitive protein adsorption and initial attachment of osteoblasts." *Biomed. Mater.*, 4(4).

Wei, K., Gao, M., Wang, Z., and Zeng, X. (2014). "Effect of energy input on formability, microstructure and mechanical properties of selective laser melted AZ91D magnesium alloy." *Mater. Sci. Eng. A*, 611, 212–222.

Witte, F. (2010). "The history of biodegradable magnesium implants: A review." *Acta Biomater.*, 6(5), 1680–1692.

Witte, F. (2015). "Reprint of: The history of biodegradable magnesium implants: A review." *Acta Biomater.*, 23(S), S28–S40.

Witte, F., Feyerabend, F., Maier, P., Fischer, J., Störmer, M., Blawert, C., Dietzel, W., and Hort, N. (2007). "Biodegradable magnesium-hydroxyapatite metal matrix composites." *Biomaterials*, 28(13), 2163–2174.

Witte, F., Hort, N., Vogt, C., Cohen, S., Kainer, K. U., Willumeit, R., and Feyerabend, F. (2008). "Degradable biomaterials based on magnesium corrosion." *Curr. Opin. Solid State Mater. Sci.*, 12(5–6), 63–72.

Woodrow, P. (2004). "Arterial blood gas analysis." *Nurs. Stand.*, 18(21), 45-52; quiz 54-55.

Wu, Y. J., Xu, C., Zheng, F. Y., Peng, L. M., Zhang, Y., and Ding, W. J. (2013). "Formation and characterization of microstructure of as-cast Mg – 6Gd – 4Y – xZn – 0 . 5Zr (x = 0 . 3 , 0 . 5 and 0 . 7 wt .%) alloys." 9, 3–9.

Xin, Y., Hu, T., and Chu, P. K. (2011). “In vitro studies of biomedical magnesium alloys in a simulated physiological environment: A review.” *Acta Biomater.*, 7(4), 1452–1459.

Xu, D., Han, E. H., and Xu, Y. (2016). “Effect of long-period stacking ordered phase on microstructure, mechanical property and corrosion resistance of Mg alloys: A review.” *Prog. Nat. Sci. Mater. Int.*, 26(2), 117–128.

Xu, D. K., Liu, L., Xu, Y. B., and Han, E. H. (2007). “Effect of microstructure and texture on the mechanical properties of the as-extruded Mg-Zn-Y-Zr alloys.” *Mater. Sci. Eng. A*, 443(1–2), 248–256.

Yamasaki, Michiaki and Anan, Tsutomu and Yoshimoto, Shintaro and Kawamura, Y. (2005). “Mechanical properties of warm-extruded Mg – Zn – Gd alloy with coherent 14H long periodic stacking ordered structure precipitate Mechanical properties of warm-extruded Mg – Zn – Gd alloy with coherent 14H long periodic stacking.” *Scr. Mater.*, 53(OCTOBER 2005), 1–6.

Yamasaki, M., Sasaki, M., Nishijima, M., Hiraga, K., and Kawamura, Y. (2007). “Formation of 14H long period stacking ordered structure and profuse stacking faults in Mg-Zn-Gd alloys during isothermal aging at high temperature.” *Acta Mater.*, 55(20), 6798–6805.

Yang, H., Xia, K., Wang, T., Niu, J., Song, Y., Xiong, Z., Zheng, K., Wei, S., and Lu, W. (2016). “Growth, in vitro biodegradation and cytocompatibility properties of nano-hydroxyapatite coatings on biodegradable magnesium alloys.” *J. Alloys Compd.*, 672, 366–373.

Yang, H., Zeng, H., Hao, L., Zhao, N., Du, C., Liao, H., and Wang, Y. (2014). “Effects of hydroxyapatite microparticle morphology on bone mesenchymal stem cell behavior.” *J. Mater. Chem. B*, 2(29), 4703–4710.

Yang, J., Wang, L., Wang, L., and Zhang, H. (2008). “Microstructures and mechanical properties of the Mg – 4 . 5Zn – x Gd (x = 0 , 2 , 3 and 5) alloys.” *J. Alloys Compd.*, 459, 274–280.

Yang, L., Huang, Y., Peng, Q., Feyerabend, F., Kainer, K. U., Willumeit, R., and Hort, N. (2011). “Mechanical and corrosion properties of binary Mg – Dy alloys for medical applications.” *Mater. Sci. Eng. B*, 176(20), 1827–1834.

Yang, L., and Zhang, E. (2009). “Biocorrosion behavior of magnesium alloy in different simulated fluids for biomedical application.” *Mater. Sci. Eng. C*, 29(5), 1691–1696.

Yang, M., Cheng, L., and Pan, F. (2009). “Comparison about effects of Ce, Sn and Gd additions on as-cast microstructure and mechanical properties of Mg-3.8Zn-2.2Ca (wt%) magnesium alloy.” *J. Mater. Sci.*, 44(17), 4577–4586.

Zainal Abidin, N. I., Rolfe, B., Owen, H., Malisano, J., Martin, D., Hofstetter, J., Uggowitzer, P. J., and Atrens, A. (2013). “The in vivo and in vitro corrosion of high-purity magnesium and magnesium alloys WZ21 and AZ91.” *Corros. Sci.*, 75, 354–366.

Zander, D., and Zumdick, N. A. (2015). “Influence of Ca and Zn on the microstructure and corrosion of biodegradable Mg-Ca-Zn alloys.” *Corros. Sci.*, 93, 222–233.

Zartner, P., Cesnjevar, R., Singer, H., and Weyand, M. (2005). “First successful implantation of a biodegradable metal stent into the left pulmonary artery of a preterm baby.” *Catheter. Cardiovasc. Interv.*, 66(4), 590–594.

Zhang, B. P., Wang, Y., and Geng, L. (2011). “Research on Mg-Zn-Ca alloy as degradable biomaterial.” *Biomater. - Phys. Chem.*, 184–204.

Zhang, E., Yin, D., Xu, L., Yang, L., and Yang, K. (2009). “Microstructure, mechanical and corrosion properties and biocompatibility of Mg–Zn–Mn alloys for biomedical application.” *Mater. Sci. Eng. C*, 29(3), 987–993.

Zhang, J., Xin, C., Cheng, W., Bian, L., Wang, H., and Xu, C. (2013a). “Research on long-period-stacking-ordered phase in Mg-Zn-Dy-Zr alloy.” *J. Alloys Compd.*, 558, 195–202.

Zhang, J., Xin, C., Nie, K., Cheng, W., Wang, H., and Xu, C. (2014a). “Microstructure and mechanical properties of Mg-Zn-Dy-Zr alloy with long-period stacking ordered

phases by heat treatments and ECAP process." *Mater. Sci. Eng. A*, 611, 108–113.

Zhang, J., Zhang, W., Bian, L., Cheng, W., Niu, X., Xu, C., and Wu, S. (2013b). "Study of Mg-Gd-Zn-Zr alloys with long period stacking ordered structures." *Mater. Sci. Eng. A*, 585, 268–276.

Zhang, L. N., Hou, Z. T., Ye, X., Xu, Z. Bin, Bai, X. L., and Shang, P. (2013c). "The effect of selected alloying element additions on properties of Mg-based alloy as bioimplants: A literature review." *Front. Mater. Sci.*, 7(3), 227–236.

Zhang, S., Zhang, X., Zhao, C., Li, J., Song, Y., and Xie, C. (2010). "Acta Biomaterialia Research on an Mg – Zn alloy as a degradable biomaterial." *Acta Biomater.*, 6(2), 626–640.

Zhang, X., Wu, Y., Xue, Y., Wang, Z., and Yang, L. (2012a). "Biocorrosion behavior and cytotoxicity of a MgGdZnZr alloy with long period stacking ordered structure." *Mater. Lett.*, 86, 42–45.

Zhang, X., Yuan, G., Mao, L., Niu, J., Fu, P., and Ding, W. (2012b). "Effects of extrusion and heat treatment on the mechanical properties and biocorrosion behaviors of a Mg-Nd-Zn-Zr alloy." *J. Mech. Behav. Biomed. Mater.*, 7, 77–86.

Zhao, M. C., Liu, M., Song, G. L., and Atrens, A. (2008). "Influence of pH and chloride ion concentration on the corrosion of Mg alloy ZE41." *Corros. Sci.*, 50(11), 3168–3178.

Zheng, L., Liu, C., Wan, Y., Yang, P., and Shu, X. (2011). "Microstructures and mechanical properties of Mg-10Gd-6Y-2Zn-0.6Zr(wt.%) alloy." *J. Alloys Compd.*, 509(35), 8832–8839.

Zheng, Y. F., Gu, X. N., and Witte, F. (2014). "Biodegradable metals." *Mater. Sci. Eng. R Reports*, 77(September 2015), 1–34.

Zhong, C., Liu, F., Wu, Y., Le, J., Liu, L., He, M., Zhu, J., and Hu, W. (2012). "Protective diffusion coatings on magnesium alloys: A review of recent developments." *J. Alloys Compd.*, 520, 11–21.

Zhu, X., Chen, J., Scheideler, L., Reichl, R., and Geis-gerstorfer, J. (2004). “Effects of topography and composition of titanium surface oxides on osteoblast responses.” 25, 4087–4103.

Zhu, Y., Wu, G., Zhang, Y. H., and Zhao, Q. (2011). “Growth and characterization of Mg(OH)2film on magnesium alloy AZ31.” *Appl. Surf. Sci.*, 257(14), 6129–6137.

Zierold, A. A. (1924). “Reaction of bone to various metals.” *Arch. Surg.*, 9, 365–412.

Zreiqat, H., Howlett, C. R., Zannettino, A., Evans, P., Schulze-Tanzil, G., Knabe, C., and Shakibaei, M. (2002). “Mechanisms of magnesium-stimulated adhesion of osteoblastic cells to commonly used orthopaedic implants.” *J. Biomed. Mater. Res.*, 62(2), 175–184.

LIST OF PUBLICATIONS

	Title of the paper	Authors (in the same order as in the paper. Underline the Research Scholar's name)	Name of the Journal/ Conference, Vol., No., Pages	Month, Year of Publication	Category*
1	Effect of zinc and rare earth element addition on mechanical, corrosion and biological properties of magnesium	**Rakesh K. Rajan,** Srikanth Bontha, Ramesh M.R, S.B Arya, Anuradha Jana, Mitun Das, V.K Balla, Srinivasan A, T. Ramprabhu	Journal of Materials Research (2018) 33, pp-3466-3478 (Cambridge Core, **SCI**)	August 2018	1
2	Laser surface modification of Mg-Zn-Gd alloy: microstructural, wettability and *in vitro* degradation aspects.	**Rakesh K.R,** Srikanth Bontha, Ramesh M.R, S.B Arya, Mitun Das, V.K Balla, Srinivasan A	Material Research Express (2018), 5,pp-126502 (IOP Science, **SCIE,**)	September 2018	1
3	Laser surface melting of Mg-Zn-Dy alloy for better wettability and corrosion resistance for biodegradable implant applications	**Rakesh K.R,** Srikanth Bontha, Ramesh M.R, Mitun Das, V.K Balla,	Applied Surface Science 480 (2019) 70-82 (Elsevier, **4.4, SCI, SCOPUS**)	February 2019	1
4	Investigation of bio corrosion properties of as cast Mg-Zn-Gd alloy in a hank's solution	**Rakesh K.R,** Srikanth Bontha, Ramesh M.R, S.B Arya, V.K Balla, Srinivasan A	The fourth international conference on advance in materials and materials processing. Indian Institute of Technology, Kharagpur, India	November 2016	4

5	Microstructure and Mechanical Properties of Laser Melted Mg-Zn-Gd Alloy.	**Rakesh K.R,** Srikanth Bontha, Ramesh M.R, S.B Arya, V.K Balla, Srinivasan A	Indian Institute of metals NMD-ATM, BITS, Goa, India.	November 2017	4
6	Surface Modification of Mg-Zn-Dy-Zr Alloy by Laser surface melting Approach: for Tailoring the *In-vitro* Degradation and Mechanical Properties	**Rakesh K R,** Srikanth Bontha, Ramesh M.R, Mitun Das, Vamsi Krishna Balla	Indian Institute of metals NMD-ATM, Kolkatta, India.	November 2018	4

Category*: 1: Journal paper, full paper reviewed 2: Journal paper, Abstract reviews

3: Conference/Symposium paper, full paper reviewed 4: Conference/Symposium paper, abstract reviewed

5: others (including papers in Workshops, NITK Research Bulletins, Short notes etc.)

BIO-DATA

1. **Name** : Rakesh K Rajan
2. **Father's Name** : Rajan K.R
3. **Date of Birth** : 18th March 1988
4. **Nationality** : Indian
5. **Marital Status** : Married
6. **Address** : Department of Mechanical Engineering
   National Institute of Technology Karnataka
   Surathkal, PO Srinivasnagar 575 025
   Karnataka, India.
7. **Mobile Number** : +91-8904410288
8. **E-mail id.** : *rakprofile@gmail.com*
9. **Educational Qualification** :

Qualification	University/Board	Year of Passing
Ph.D. (Mechanical Engineering)	National Institute of Technology Karnataka	Thesis submitted: 17/12/2018
M.Tech. (Mechanical Engineering)	VIT University, Chennai	2014
B.Tech. (Mechanical Engineering)	Mahatma Gandhi University, Kottayam	2010